DNA 4612F

CHARACTERISTICS OF STRIATION STRUCTURE AND EFFECTS ON SCINTILLATION

Science Applications, Inc.

1200 Prospect Street

La Jolla, California 92037

May 1978

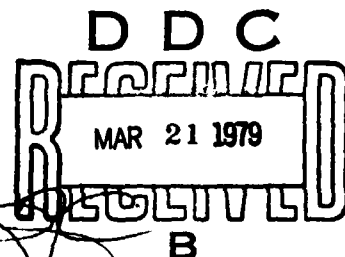Final Report for Period 1 October 1974—28 April 1978

CONTRACT No. DNA 001-75-C-0033

DDC FILE COPY

DDC
RECEIVED
MAR 21 1979
RECEIVED
B

Prepared for

Director

DEFENSE NUCLEAR AGENCY

Washington, D. C. 20305

REPORT DOCUMENTATION PAGE		READ INSTRUCTIONS BEFORE COMPLETING FORM
1. REPORT NUMBER DNA 4612F	2. GOVT ACCESSION NO.	3. RECIPIENT'S CATALOG NUMBER
4. TITLE (and Subtitle) CHARACTERISTICS OF STRIATION STRUCTURE AND EFFECTS ON SCINTILLATION.		5. TYPE OF REPORT & PERIOD COVERED Final Report for Period 1 October 1974—28 April 1978.
		6. PERFORMING ORG. REPORT NUMBER SAI-78-677-LJ
7. AUTHOR(s) David L. Sachs Lewis M. Linson David C. Baxter		8. CONTRACT OR GRANT NUMBER(s) DNA 001-75-C-0033
9. PERFORMING ORGANIZATION NAME AND ADDRESS Science Applications, Inc. 1200 Prospect Street La Jolla, California 92037		10. PROGRAM ELEMENT, PROJECT, TASK AREA & WORK UNIT NUMBERS NWED Subtask S99QAXHB054-04
11. CONTROLLING OFFICE NAME AND ADDRESS Director Defense Nuclear Agency Washington, D.C. 20305		12. REPORT DATE May 1978
		13. NUMBER OF PAGES 104
14. MONITORING AGENCY NAME & ADDRESS(if different from Controlling Office)		15. SECURITY CLASS (of this report) UNCLASSIFIED
		15a. DECLASSIFICATION DOWNGRADING SCHEDULE

16. DISTRIBUTION STATEMENT (of this Report)

Approved for public release; distribution unlimited.

17. DISTRIBUTION STATEMENT (of the abstract entered in Block 20, if different from Report)

18. SUPPLEMENTARY NOTES

This work sponsored by the Defense Nuclear Agency under RDT&E RMSS Code B322077464 S99QAXHB05404 H2590D.

19. KEY WORDS (Continue on reverse side if necessary and identify by block number)

Scintillation	Striations
Propagation	Bifurcation
Power Spectra	Structured Ionization
Nuclear Striations	

20. ABSTRACT (Continue on reverse side if necessary and identify by block number)

The characteristics of striations that are expected to be generated following a high-altitude nuclear explosion and the scintillation effects they produce are described. The shapes and density profiles of the striations are parameterized. The connection between the statistics of signal scintillation and the parameterized structural characteristics of the striations is described through the generation of formulas by an approximate analytic treatment of the power-spectral-density (PSD) of single-size striations. The formulas are

DD FORM 1473 1 JAN 73 EDITION OF 1 NOV 65 IS OBSOLETE

20. ABSTRACT (Continued)

tested by numerical propagation calculations and found to be adequate within the uncertainties of the striation parameters. The uncertainties in our present understanding of the application of the gradient-drift mechanism towards a precise description of the striation characteristics and their development in time are explored. A methodology for calculating the time-dependent phase PSD resulting from the evolving striations is introduced and a sample calculation appropriate for late-time after burst is carried out explicitly.

TABLE OF CONTENTS

LIST OF ILLUSTRATIONS

LIST OF TABLES

1. INTRODUCTION

High Altitude Nuclear Explosions (HANE) deposit large amounts of ionization in the earth's ionosphere and above. At late times the ionization density is low enough so that radio signals from satellites to ground or air receivers are not absorbed. At these times much of the ionization is structured. The ionization tends to form clumps (striations) which are nearly uniform along the earth's magnetic field for large distances but break up in the direction perpendicular to the field into smaller striations. The structuring of the ionization causes random refraction and diffraction of the radio signal producing scintillation in the signal phase and amplitude at the receiver as the satellite-receiver line-of-sight moves across the structure.

The understanding of the extent and character of the scintillation is important for the planning of future satellite communication systems. The Defense Nuclear Agency (DNA) has been studying this problem for many years. There have been many studies of the effects of various models of the structure on the statistics of the signal scintillation.[1-4]

This report represents an extension of these studies. A primary goal is to attack the problem of describing the scintillation effects to be expected from HANE. Most previous studies of the development of striations have not concentrated on specifying the shapes and profiles of striations that might be expected following a nuclear burst. In this report models of the structure are parameterized and an attempt is made to relate these models with the structure to be expected in HANE. The resulting effects on scintillations are calculated. Furthermore, the relation between the model values and the physical processes that cause structuring is discussed. A new methodology for determining the power-spectral-density (PSD) of the phase variations as a function of time is also discussed and an explicit example is presented.

In principle, the procedure to follow is straightforward. The output of the hydrocodes determines the electron density, neutral density, and neutral winds on a global scale (hundreds to thousands of kilometers). From these parameters a complete understanding of the physical processes which cause structuring would provide the capability of describing the development of striations in the microscale as a function of time and space. Given the parameters that characterize the irregularities of electron density, the power-spectral-density of the variations in phase as a function of space and time would be determined. That information is sufficient to calculate various important parameters which are a measure of the effect on propagation, such as scintillation index or the bit-error-rate on communications links.

We do not presently have sufficient knowledge to carry out the above task with certainty. The weak link is in providing an accurate description of the structure. In order to provide this description three basic things are needed: 1) a specification of the background conditions; 2) an understanding of the basic mechanisms that lead to the generation of structure; and 3) detailed knowledge regarding the method in which those basic mechanisms operating under the specified background conditions lead to the generation of specific structures.

The various two-fluid hydrocodes and their electrostatic counterparts can be considered state-of-the-art in regard to specifying the background large-scale conditions. These various codes provide the specification of the distribution of the neutral particles, ionization, and the velocity of neutral particles, $\vec{V}_n$, on the large scale. Various techniques are available for calculating the ion motion. The ion velocity, $\vec{V}_i$, must be consistent with the electric field pattern that results from the application of the continuity of current flow in the magnetized plasma. From these, the component of the slip velocity, $\vec{V}_s = \vec{V}_n - \vec{V}_i$, perpendicular to the magnetic field can be estimated. The specification of these time-varying parameters by the output of the hydrocodes is necessary but not sufficient in order to specify the structure.

In this report we will concentrate on the gradient-drift mechanism as being the mechanism that leads to the generation of striations during the first tens of minutes following a burst. Since this mechanism was first identified

nine years ago[5], it has been the subject of intense analytical, experimental, and numerical work. However, our understanding of the complex electrodynamics that governs development of irregularities is not yet sufficient to be able to specify the structure precisely. The hydrocodes have been able to specify the regions of space as a function of time in which significant growth of structure can be expected. The microscale codes, operated principally by NRL, have provided some of the characteristics of the development of structure for particular cases. Observations of some of the characteristics of striations produced by the gradient-drift mechanism have been obtained from barium release experiments conducted in the ionosphere. Basically the results of current research have been to support the validity of the general concepts regarding the development of striations. However, many specific questions for which answers are required in order to accurately specify the structure.have at the moment only speculative theoretical answers.

In order to estimate the effects of striations on propagation, we have accomplished three things. First, we have modeled characteristics of striations that have an impact on propagation. These characteristics are the shape of the striation, the profile of the electron density within the striation, and, in some cases, a distribution of scale sizes of striations. Second, we have identified specific gaps in our current understanding of the physical processes that specify these striation characteristics. We indicate that there are procedures that could be followed that could verify or deny some of the theoretical speculations regarding the specifications of these characteristics. Thirdly, we have developed a methodology for determining the time-dependent power-spectral-density of striations and have carried out a specific model calculation exemplifying the results of applying that methodology. This methodology can be viewed as an alternative to the methodology being developed by J. Workman of BRA for the SCENARIO code.

Section 2 contains a description of the model structures used in order to calculate the effects of striations on propagation. The parameterization of the shapes and profiles are described along with the resultant power-spectral-densities. The significance of the power-spectral-density (PSD) for estimating

7

the signal scintillation statistics is emphasized. Section 3 contains the results of applying the various models in order to obtain the dependence of the signal scintillation statistics on the assumed structures.

Section 4 discusses the physical processes that lead to a specification of the structures. This discussion includes an application of our present understanding derived from both linear and nonlinear analyses to a description of the time-development of striations in HANE. The gaps in our knowledge for making precise statements are emphasized. A methodology based on the bifurcation of striations for determining the time-dependent power-spectral-density is described in Section 5. A specific example appropriate for HANE conditions is calculated in detail. It is emphasized that the inputs to this methodology are the physical processes that lead to the development of striations. As our understanding regarding the development of striations is improved, those aspects that have a direct impact on scintillation effects can be incorporated into the same methodology.

2. STRIATION STRUCTURE

2.1   INTRODUCTION

A radio signal passing through a medium will have spatial variation in its amplitude (scintillation) over an area perpendicular to the line-of-sight if the medium is structured, i.e., not homogeneous. A late-time high-altitude nuclear burst's ionization is structured in the following ways on a descending order of scale size:

1. The ionization is localized within a region hundreds of kilometers in radius transverse to the magnetic field and thousands of kilometers in extent along the magnetic field;

2. The ionization is in the form of distinct cylindrical shapes (striations) imbedded in a region of much smaller (background) ionization;

3. The boundaries of these striations (electron density contours) are not smooth;

4. Sound-wave-like disturbances can exist within the striations.

The effects caused by the large-scale structure of the first type alone are negligible for the late-time electron densities and radio frequencies of interest in this study.

The dependence of the system degradation on the signal scintillation caused by structure of the second type is the subject of concern. As in our previous studies[1] we model this structure as a given set of ionization profiles randomly distributed within a given area. The amount of structure of types 3 and 4 are unknown at this time. The statistics of the scintillating signal at some distance beyond the striations are obtained using the thin-screen approximation. The results are presented as a function of λ, the signal wavelength,

9

d, distance away from the striations, n_0, peak electron density, and number, size, and shape of the ionization profile.

For any given set of striation sizes and shapes, the signal and its statistics are functions of only two dimensionless parameters:

$$\epsilon = \frac{\lambda d}{4\pi a^2}$$

where a is the characteristic scale size of the striations; and

$$\varphi_0 \equiv \sqrt{\overline{(\varphi(x) - \bar{\varphi})^2}}$$

the root-mean-square of the phase variations in the signal at the exit plane of the striations. In the thin-screen approximation, this phase is obtained by a straight-line integration of the electron density along the line-of-sight of the radio signal. For the electron density defined in an area L by L in the x-y plane;

$$\varphi(x) = r_e \lambda \int_0^L dy \, n_e(x, y) \ .$$

where y is the direction of propagation of a plane wave of wavelength λ and

$$r_e = 2.818 \times 10^{-13} \text{ cm}$$

is the classical electron radius. We define the average of any function f(x) as

$$\bar{f} = \frac{1}{L} \int_0^L dx \, f(x) \ .$$

We take the x-direction as the direction of motion of the line-of-sight (y-direction) of the signal past the ionization due to the motion of the transmitter, receiver or striations. The area $A = L^2$, will be expanding in time as the ionization spreads across magnetic field lines.

Consider the following typical example of the time-dependent ionization structure in the plane of area A. Before the onset of striations, assume that the ionization has a radial dependence only about some central position. Fig. 1(A) illustrates the contours of constant electron density, n_e, for this case. In the general case, the magnetic field will not be perpendicular to the plane and the contours will be ellipses elongated in the direction of the magnetic field's projection on the plane. This complication does not qualitatively change the result.

10

(A)

1×10^6 CM^{-3}

3

10

30

100

-400   -200   0   200   400

KM

(B)

-400   -200   0   200   400

KM
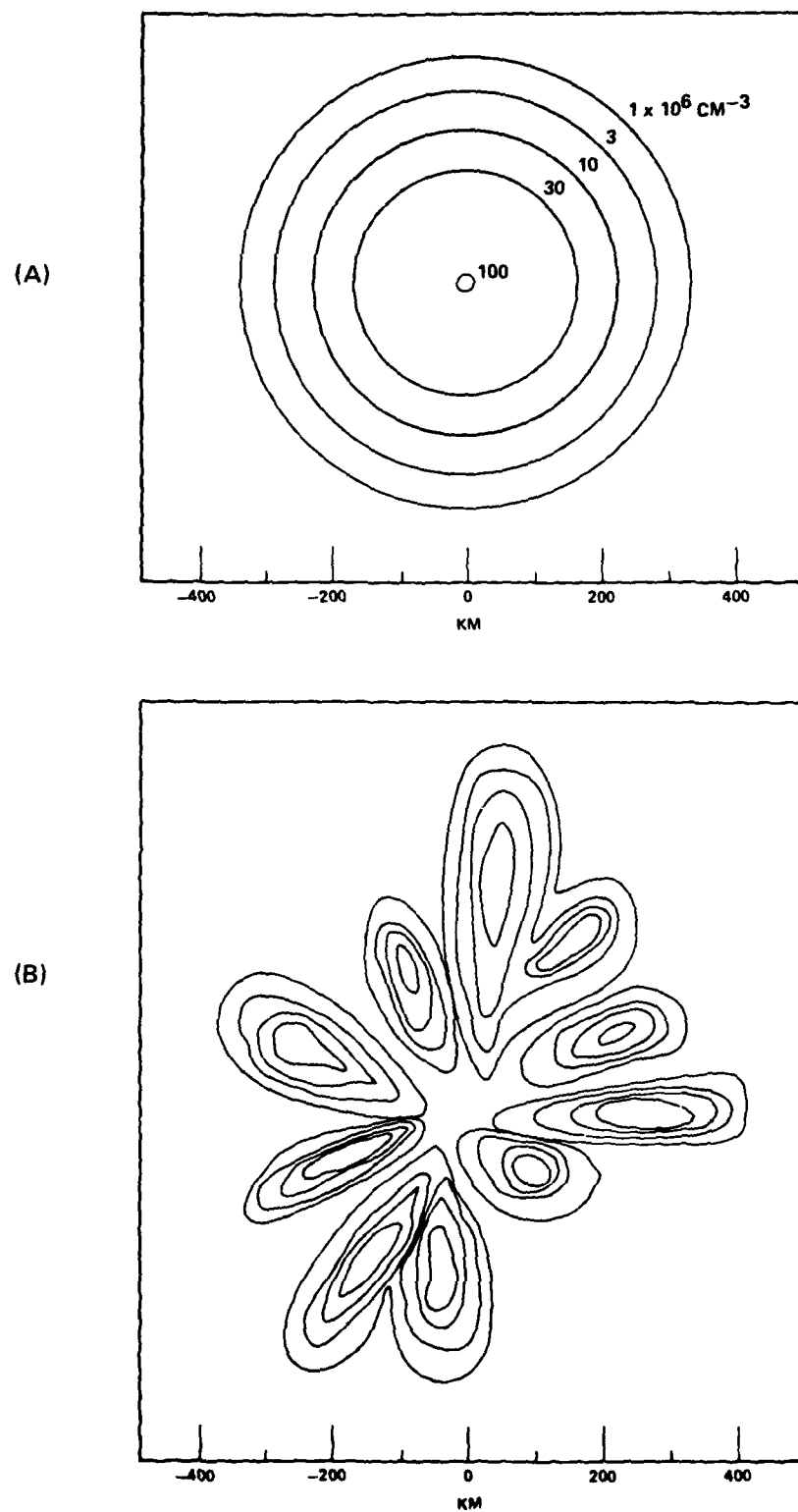
Figure 1. Schematic of electron density contours (A) before significant
structuring has taken place and (B) at around 500 s after burst
after large-scale structuring has occurred.

11

The contours illustrated are a representation of the output of an MHD computer code minutes after a high altitude burst. These contours can be approximately fit by a function of the form

$$n_e(x, y) = n_o e^{-r^2/a_o^2} + n_b$$

where r is the distance from the center and $a_o \approx 150$ km for a typical case.

This large value of a characteristic size a_o, does not lead to any amplitude scintillation in a signal traversing the ionization for the range of parameters of concern to this study:

$$\lambda \leq 10^{-3} \text{ km}$$
$$n_o \leq 10^8 \text{ cm}^{-3}$$
$$n_b \leq 10^6 \text{ cm}^{-3}$$

We therefore ignore this structure of the first type.

When the ionization breaks up from instabilities generated by a radial neutral wind into fingers that are convected radially, the total electron content will be maintained except for the ongoing processes of chemistry and diffusion along the magnetic field. The fact that the ionization is structured into smaller parcels will bring about amplitude variations. This is the structure of the second type to be investigated in this report.

Barring unforeseen surprises we expect the late-time nuclear structure to resemble a radial version of the output of the electrostatic codes of NRL[6]. By radial we mean that the 2-D cartesian fingers of NRL which extend in the constant neutral wind direction would appear in the nuclear case to extend radially outward from a cylinder axis along the magnetic field through the center of the ionization [Fig. 1(B)]. In the course of time there will be bifurcations which increase the number of fingers and decrease their size. The orientation of the major axes of the fingers will be primarily along radials and at some point further bifurcation will cease and there will be a limiting size distribution with the smallest being depleted by diffusion. A model of this time-dependent process will be described in more detail in Section 5.

2.2   STRIATION PROFILES

The essential properties of the structured ionization of a single striation important for producing amplitude scintillation appear to be:

1.   Shapes which vary from circular to highly elongated ellipses;
2.   Profiles with large density gradients in the narrow dimension;
3.   Smaller gradients in the elongated direction down to some value of n_e, then abrupt gradients.

We choose to model these features with a two-parameter set of analytic profiles:

$$n_e = n_o \left(1 - \frac{\alpha^2 r^2}{a^2}\right) \quad r \leq a$$
$$= 0 \quad\quad\quad\quad r > a \quad\quad\quad\quad (2.2.1)$$

where $r^2 = \beta x^2 + y^2/\beta$. Contours of electron density are ellipses with major to minor axes ratio β.

This is a new concept of profile which occurred to the authors after seeing the NRL contours of n_e from their numerical codes[6]. In contrast to earlier work[7], this numerical study treated a case where the initial Pedersen conductivity was much higher than the background. The profiles of ionization varied smoothly down from the peak value to some smaller value where the fall-off became abrupt. Physical motivations for this type of behavior will be discussed in Section 4.

We use the parameter α to characterize the value of density at which the profile becomes steep. The parameter β describes the ellipticity of the density contours. The parameter a is the characteristic size of the profile. If the striations are distributed over a large range of sizes a, the form of the distribution of sizes will be another parameter of the problem. We have been unable to determine from the phenomenology of the bifurcation of striations any particular form for the distribution. We have shown in previous work[1] that the scintillations are highly dependent on the profile shape. A possible expected distribution of sizes will be discussed in Section 5. The comparison of the

distribution of sizes and the single size will be made by means of the power-spectral-density of the electron density.

2.3 POWER-SPECTRAL-DENSITY

We have chosen the basic representation of the structured electron density as a set of striations of given number, size and profile. An alternate representation of the electron density is through its power-spectral-density (PSD).

From the Fourier transforms of the electron density in the area $A = L^2$,

$$f(\vec{k}) = \int_0^L \frac{dx}{L} \int_0^L \frac{dy}{L} \; e^{-i\vec{k}\cdot\vec{x}} \, n_e(x,y) \; ,$$

we have

$$n_e(x,y) = \sum_{l,m} f(\vec{k}) \, e^{i\vec{k}\cdot\vec{x}}$$

where

$$\vec{k} = \left(\frac{2\pi l}{L}, \; \frac{2\pi m}{L}\right) \quad -\infty < l, m < \infty \; .$$

The average electron density is

$$\bar{n}_e = \frac{1}{A} \int d\vec{x} \, n_e(x,y) = f(0) \; .$$

If we set $f(0) \equiv 0$, then $f(\vec{k})$ is the Fourier transform of $\Delta n_e \equiv n_e - \bar{n}_e$. Define the PSD of the electron density by

$$\Phi(\vec{k}) = \frac{1}{A} \int d\vec{x} \, e^{-i\vec{k}\cdot\vec{x}} \, \overline{\Delta n_e(\vec{x}') \, \Delta n_e(\vec{x}' + \vec{x})} \qquad (2.3.1)$$

$$= \frac{1}{A^2} \int d\vec{x} \int d\vec{x}' \; e^{-i\vec{k}\cdot\vec{x}} \, \Delta n_e(\vec{x}') \, \Delta n_e(\vec{x}' + \vec{x})$$

$$= f(\vec{k}) f(-\vec{k}) = |f(\vec{k})|^2$$

where $f(-\vec{k}) = f^*(\vec{k})$ follows from the fact that Δn_e is real.

Thus the PSD of n_e, $\Phi(\vec{k})$, defined by Eq. (2.3.1), is given by

$$\Phi(\vec{k}) = |f(\vec{k})|^2 \ .$$

The propagation analysis requires

$$\varphi(x) = r_e \lambda \int_0^L \Delta n(x, y)\, dy$$

which has the Fourier transform

$$F(k) = \frac{1}{L} \int_0^L \varphi(x) e^{-ikx}\, dx = r_e \lambda L\, f(k, 0) \ .$$

We will use the notation of Salpeter[8] for the PSD of phase

$$\varphi^2(q) \equiv \frac{1}{2\pi} \int_{-\infty}^{\infty} dr\, e^{-iqr}\, \overline{\varphi(x)\varphi(x+r)}$$

defined for an infinite interval and evaluate it for our defined phase on the interval $0 \le x \le L$ to obtain

$$\varphi^2(q) = \frac{L}{2\pi} |F(q)|^2 = \frac{L}{2\pi} (r_e \lambda L)^2 |f(q, 0)|^2 \qquad (2.3.2)$$

In Salpeter's [8] description of the original analysis of Mercier [9], the statistics of the intensity scintillations are described completely in terms of $\varphi^2(q)$. This is because Mercier required the condition

$$\overline{e^{i \sum_j a_j \varphi(x_j)}} = e^{-\frac{1}{2} \overline{[\sum_j a_j \varphi(x_j)]}^2}$$

for a_j any set of constants. This condition is satisfied if $\varphi(x_j)$ is a Gaussian distributed variable. Much of the recent literature has been devoted to the question of the requirements for $\varphi^2(q)$ to be sufficient for the description of signal scintillations. A sufficient requirement is that the phase be the sum of many random contributions. Since this is the case in our analysis we will consider that a specification of $\varphi^2(q)$ is sufficient.

15

2.4 POWER-SPECTRAL-DENSITY OF STRIATIONS

The connection between $\varphi^2(q)$ and a random set of striations is as follows.

The profile in expression (2.2.1) has the Fourier transform

$$f(k_{x'}, k_{y'}; \vec{x}_i) = e^{-i\vec{k} \cdot \vec{x}_i} f_i(k_{x'}, k_{y'})$$

where

$$f_i(k_{x'}, k_{y'}) = \frac{2n_o \pi a^2}{L^2} \left[\frac{J_1(s)}{s} (1 - \alpha^2) + 2\alpha^2 \frac{J_2(s)}{s^2} \right]$$

where

$$s = a \sqrt{\frac{k_{x'}^2}{\beta} + k_{y'}^2 \beta}$$

and $J_{1,2}$ are Bessel functions.

The y'-direction is along the major axis of the ellipse and $\vec{x}_i$ is the position of the striation in the xy plane. The phase integral is along the y-axis which is taken to be at an angle θ_i to the y'-axis so that

$$x = x' \cos \theta_i + y' \sin \theta_i .$$

The Fourier transform of the phase produced by the striation is

$$F_i(k) = r_e \lambda L e^{-ikx_i} \iint \frac{dx}{L} \frac{dy}{L} e^{-ikx} n_e(x - x_i, y - y_i)$$

$$= r_e \lambda L e^{-ikx_i} \iint \frac{dx'}{L} \frac{dy'}{L} e^{-i(k \cos \theta_i x' + k \sin \theta_i y')} n_e(x' - x_i, y' - y_i)$$

$$= r_e \lambda L e^{-ikx_i} f_i(k \cos \theta_i, k \sin \theta_i) .$$

The total phase produced by a set of striations has the Fourier transform

$$F(k) = \sum_i F_i(k)$$

and the PSD

$$\varphi^2(q) = \frac{L^3}{2\pi}(r_e\lambda)^2\left[\sum_i f_i^2\,(q\cos\theta_i,\ q\sin\theta_i)\right.$$

$$\left. + \sum_{i\neq j} e^{-iq(x_i-x_j)}\,f_i(q\cos\theta_i,\ q\sin\theta_i)\,f_j(q\cos\theta_j,\ q\sin\theta_j)\right]$$

(2.4.1)

from Eq. (2.3.2).

    Some comments are in order here. In a previous analysis[1] we showed the contribution of the second term in brackets to be an A. C. jitter about the contribution of the first term due to the positions of a given set of striations. If we average $\varphi^2(q)$ over an ensemble of random placements of the striations with the fractional number of times striation i is at x_i being $P_i(x_i)dx_i$ and consider the positioning of striations to be uncorrelated, the average of the second term in brackets is

$$\sum_{i\neq j} f_i(q\cos\theta_i,\ q\sin\theta_i)f_j(q\cos\theta_j,\ q\sin\theta_j)\,|S|^2$$

where

$$S = \int_0^L P_i(x_i)\,dx_i\,e^{-iqx_i}\ .$$

If the distribution over the length L is uniform, $P = \frac{1}{L}$ and $S = \frac{\sin(qL/2)}{(qL/2)}$ which is zero at $q = 2\pi\,\frac{\ell}{L}, \ell = 1,\ 2,\ \ldots,$ the only values of q used.

    This means the PSD is given by the first term alone for determining effects due to the striations' profiles.

    There have been experimental determinations of the PSD which have included large contributions from structure of the first type, the positioning of the ionization in space. These contributions can be illustrated by distributing the striations over the line L by a Gaussian probability $P(x_i)$ where

$$P(x_i) = \frac{e^{-(x_i-L/2)^2/a^2}}{\sqrt{\pi}\,a} \qquad a \ll L/2\ .$$

17

Then $|S| = e^{-q^2 a^2/4}$. If there are M striations with the same form of profile, the bracket in Eq. (2.4.1) becomes

$$Mf^2 \left[1 + (M-1) e^{-q^2 a^2/2} \right]$$

and the second term dominates at low values of q until $Me^{-q^2 a^2/2}$ becomes less than unity. This is a real effect which must be included if one wants to include the effects of structure of the first type on scintillation or if one wants to extract properties of striations from experimentally obtained PSDs.

Another point to be made is that the portion of the PSD due to structure of the first type does not satisfy the criterion for the PSD to be sufficient to describe scintillation effects. That is, the phase variations resulting from this type of structure are not the resultant of many random inputs.

For our purposes, the connection between striation profiles and the PSD will be through the first term alone. Then

$$\varphi^2(q) = \frac{L^3}{2\pi} (r_e \lambda)^2 \sum_i f_i^2 (q \cos \theta_i, \ q \sin \theta_i) \ .$$

3. SCINTILLATION DEPENDENCE ON THE PARAMETERS OF SHAPE

3.1 CIRCULAR CONTOUR ($\beta = 1$)

We first discuss the case of $\beta = 1$ (circular n_e contours). The profile is

$$n_e = n_0 \left(1 - \frac{\alpha^2 r^2}{a^2}\right) \quad r \le a$$

$$= 0 \quad r > a$$

where $\alpha = 0$ produces the rod profile studied previously[1] and $\alpha = 1$ produces a parabolic profile. The PSD for this profile is

$$\varphi^2(q) = \frac{2\pi}{L} \ (r_e \lambda n_0 a^2)^2 \left[\frac{J_1(qa)}{qa} (1 - \alpha^2) + 2\alpha^2 \frac{J_2(qa)}{(qa)^2}\right]^2 \tag{3.1.1}$$

Fig. 2 shows the PSD of three profiles corresponding to $\alpha = 0$, 0.9 and 1. After the first zero of the Bessel function, the locus of peaks is plotted.

The large q behavior of $\alpha = 0$ and 0.9 is q^{-3} where the large q behavior of $\alpha = 1$ is q^{-5}. The PSD's are normalized so that the profiles have the same n_0 and the same total electron content which requires

$$\pi a^2 (1 - \alpha^2/2)$$

to have the same value for any α or

$$a = a\,(0)\,(1 - \alpha^2/2)^{-\frac{1}{2}}.$$

They therefore have the same value as $q \to 0$. The $\alpha = 0.9$ curve looks the same as the $\alpha = 1.0$ curve until a region around the value of $q\,a\,(0) = 2\alpha^2 \frac{\sqrt{1 - \alpha^2/2}}{(1 - \alpha^2)}$ after which the q^{-3} behavior takes over. The curves are all plotted vs. $\nu = \frac{q}{2\pi}$ for the case $a(0) = 0.282$. so the break point is at $\nu = \frac{6.6}{2\pi(0.282)} = 3.7$. From the curve we see the transition to begin at the second peak of the Bessel function where the line has a ν^{-4} dependence. The transition ends around $\nu = 7.4$ where the ν^{-3} dependence takes over.
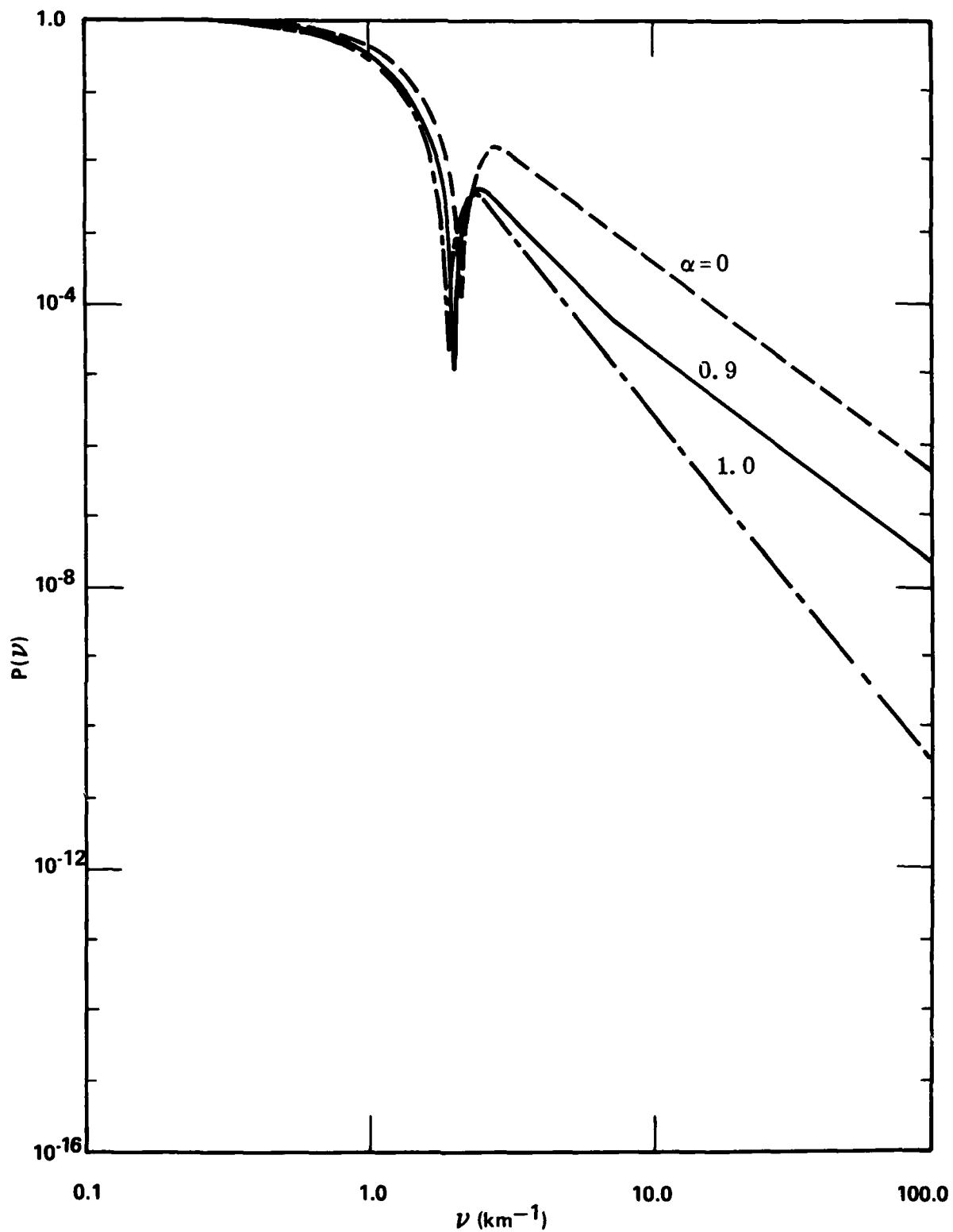
Figure 2. Power-Spectral-Density (PSD) of integrated phase shift for circular n_e contour striations ($\beta = 1$).

20

Our analysis of the scintillation effects is through the thin screen approximation and a Fast Fourier Transform propagation routine as described in our last analysis[1]. In that analysis we obtained the required $\varphi(x)$ by summing contributions from randomly placed striations. In the present analysis we have compared the results of that procedure with the alternate method of using the PSD directly. The alternate method stipulates the Fourier transform of $\varphi(x)$ to be

$$\varphi(q) \, e^{i\theta(q)},$$

where the amplitude is the square root of the PSD and the phase, $\theta(q)$, is chosen randomly between 0 and 2π for each value of q. The two methods agree if there are enough randomly placed striations so that the generated $\varphi(x)$ is due to about ten or more striations contributing for each value of x. If there are fewer striations of larger electron density so that φ_{rms} is unchanged, the comparison shows weaker scintillation effects using the random striations than using the PSD. This follows from the fact that the PSD method assumes the phase to be distributed as randomly as possible with the same φ_{rms} and correlation lengths. The PSD method is consistent with our expectation that signals will pass through many random striations.

Since the PSD is an even function of q, its Fourier transform, the phase autocorrelation, is

$$\overline{\varphi(x)\varphi(x+r)} = 2 \int_0^\infty dq \, \varphi^2(q) \cos(qr) \equiv \varphi_0^2 \, \rho(r)$$

where the variance

$$\varphi_0^2 = 2 \int_0^\infty dq \, \varphi^2(q) = \frac{16(r_e \lambda n_0 a^2)^2}{3aL} \left[(1-\alpha^2)^2 + \frac{16\alpha^2(1-\alpha^2)}{15} + \frac{32\alpha^4}{105} \right] .$$

The dependence of the phase variance on the parameter α is slight. We maintain the electron content constant as we vary α so

$$\varphi^2(q=0) = \frac{\pi}{2L} (r_e \lambda n_0 a^2)^2 (1-\alpha^2/2)^2$$

is constant and

$$\varphi_o^2 = \frac{32}{3\pi a} \frac{\left[(1-\alpha^2)^2 + \frac{16\alpha^2(1-\alpha^2)}{15} + \frac{32\alpha^4}{105}\right]}{(1-\alpha^2/2)^2} \varphi^2 \ (q=0)$$

Using $a(\alpha) = a(0)(1-\alpha^2/2)^{-\frac{1}{2}}$, the dependence of φ_o^2 on α alone varies from a factor of unity for $\alpha = 0$ to a factor $\frac{32}{105(\frac{1}{2})^{\frac{3}{2}}} = 0.862$ for $\alpha = 1$. This dependence of $\varphi_{rms} = \sqrt{\varphi_o^2}$ on α will be ignored and we will present our results of the propagation study in the usual manner[1] as a function of the two parameters, $\varphi_o = \varphi_{rms}$ and $\epsilon = \frac{\lambda d}{4\pi a^2(0)}$.

One measure of the severity of signal intensity scintillation is the scintillation index S_4 defined by

$$S_4^2 \equiv \overline{I^2} - 1$$

where I is the signal intensity on a plane a distance d from the striation normalized to intensity in the absence of striations. The average intensity $\overline{I} = 1$ by conservation of energy. This means no energy is backscattered by the striations using our propagation methods which are strictly valid for small-angle forward scatter. We have found in a previous study[1] that for $S_4 \leq 0.3$, the scintillation is too mild to disturb communication systems and for $S_4 \gtrsim 0.9$ severe scintillation occurs which can be approximated by Rayleigh statistics. These values of S_4 are therefore useful for the discussion of system effects. Another useful parameter is the intensity correlation length, ℓ, defined where

$$\overline{I(x)I(x+\ell)} - 1 = e^{-1} S_4^2 \ . \tag{3.1.2}$$

We plot the contours of $S_4 = 0.3$ and 0.9 on Figs. 3, 4 and 5 for the cases $\alpha = 0$, 0.9 and 1 respectively as a function of ϵ and φ_o. We also plot contours of $\ell/a(\alpha)$ as a function of ϵ and φ_o in the figures as dashed lines. We are strictly interested in ℓ only in the regime of strong scintillation $S_4 \gtrsim 0.9$. From the figures it is obvious that in this case $\ell/a(\alpha)$ is well approximated as a function of φ_o alone. In fact $\ell = \frac{2}{3}a(\alpha)/\varphi_o$ fits very well.
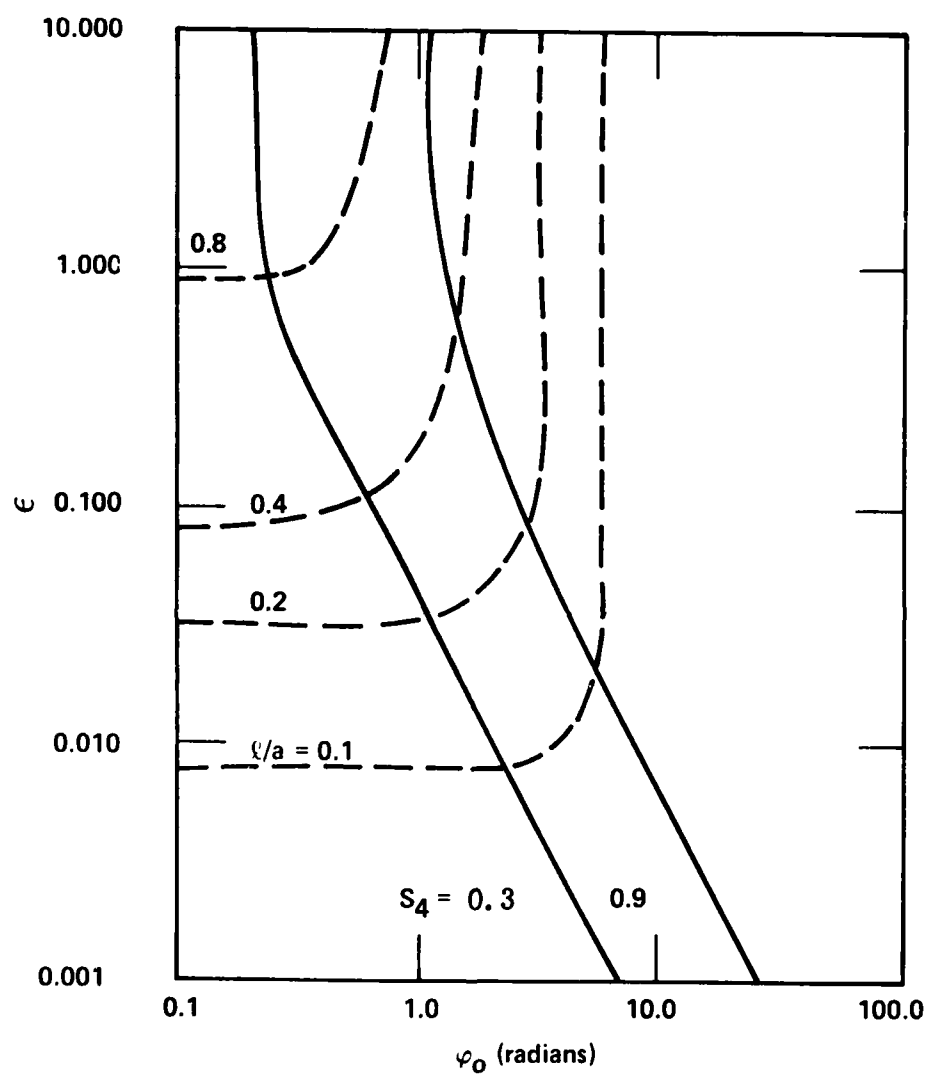
Figure 3. Contours of S_4 and ℓ/a for circular n_e contours ($\beta = 1$) and $\alpha = 0$.

23
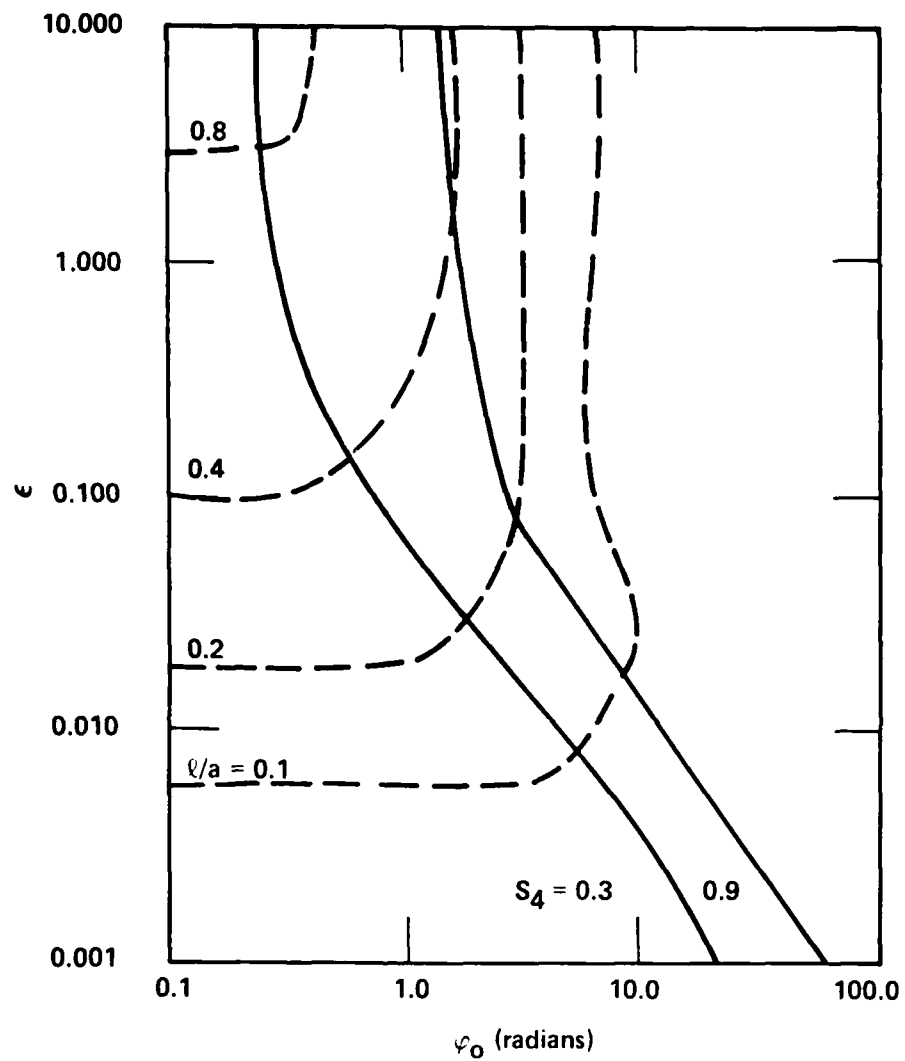
Figure 4. Contours of S_4 and ℓ/a for circular n_e contours ($\beta = 1$) and $\alpha = 0.9$.

24
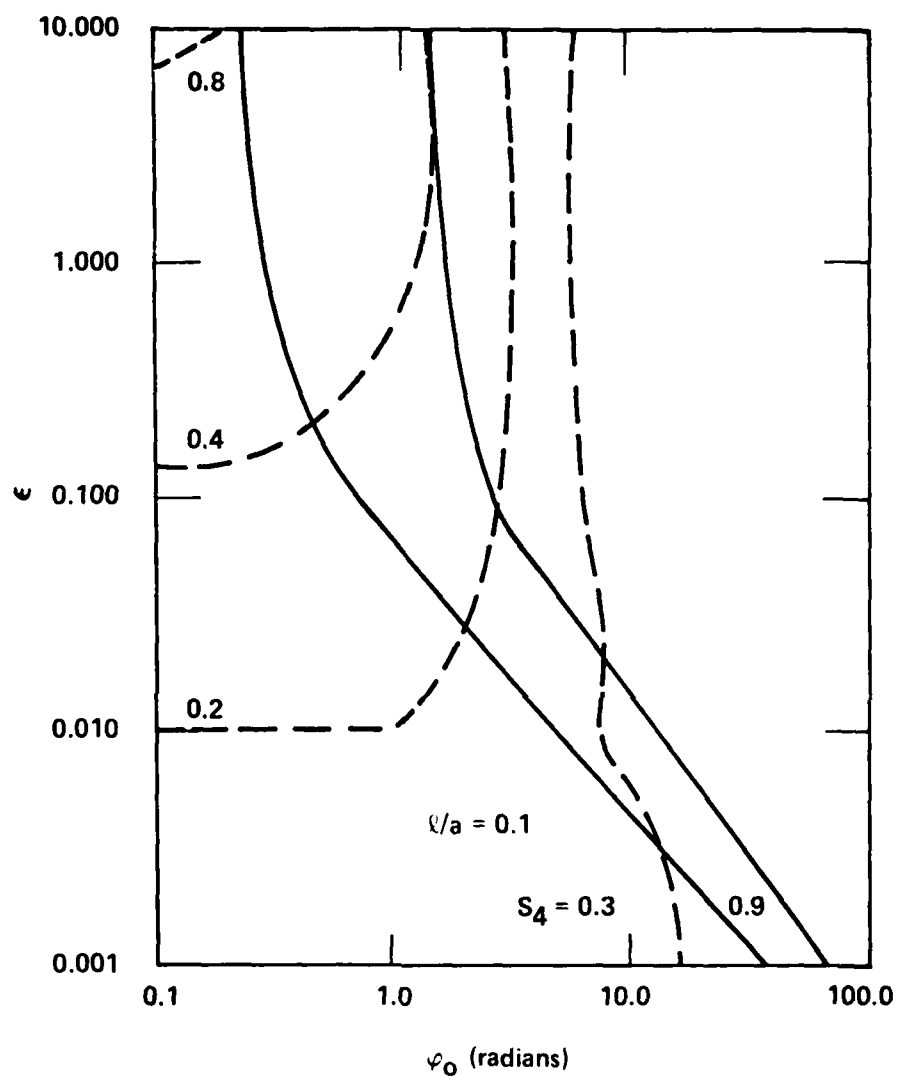
Figure 5. Contours of S_4 and ℓ/a for circular n_e contours ($\rho = 1$) and $\alpha = 1.0$.

Mercier's[9] analysis of scintillation effects in the limit as $\epsilon \to \infty$ obtained an expression for $\overline{I(x)I(x+\ell)}$ which depended on the PSD of phase alone. Again, this is because he assumed the phase to be Gaussian distributed as we do. His expression is

$$\overline{I(x)I(x+r)} - 1 = e^{-2\varphi_0^2}\left[e^{2\varphi_0^2\rho(r)} - 1\right]$$

which results in

$$S_4^2 = 1 - e^{-2\varphi_0^2}$$

or $S_4 = 0.3$ for $\varphi_0 = 0.217$ and $S_4 = 0.9$ for $\varphi_0 = 0.91$. These values are in agreement with the top of the contours in Fig. 3 for $\alpha = 0$. For the other figures, the $S_4 = 0.3$ contour is in agreement but the $S_4 = 0.9$ contour is at a larger value of φ_0 but appears to be approaching Mercier's limiting value.

The curvature of the contour of S_4 as they approach Mercier's $\epsilon = \infty$ limit contrasts strongly with the contours of ℓ/a which are straight lines down to the $S_4 = 0.9$ contour even when $\epsilon \ll 1$. We therefore believe Mercier's analysis to be valid for $S_4 \gtrsim 0.9$ for any ϵ. Since this regime always has $\varphi_0 > 1$, we take the limit of Mercier's expression where $e^{-2\varphi_0^2} \ll 1$ and obtain $\overline{I(x)I(x+\ell)} - 1 = e^{-2[\varphi_0^2 - \varphi_0^2\rho(\ell)]}$. From our formula (3.1.2) for ℓ we have

$$\varphi_0^2 - \varphi_0^2\rho(\ell) = \frac{1}{2}.$$

Since we restrict ourselves to the case of $\varphi_0^2 \gg 1$ we need to evaluate $\rho(\ell)$ for small values of ℓ/a where $\rho \approx 1 - A\ell^2/a^2$ where A is some factor depending on the functional form of the auto correlation $\rho(\ell)$. Thus

$$\ell \approx \frac{a}{\sqrt{2\varphi_0^2 A}} = \frac{1}{\sqrt{2A}} \ \frac{a}{\varphi_0}$$

and the dependence of ℓ/a on φ_0 is as seen in the figures.

We shall now discuss the $S_4 = 0.3$ contour. All figures show the contour to asymptote to a straight line $\varphi_0 = $ constant for $\epsilon \gg 1$ and to asymptote to

a straight line $\epsilon = B\varphi_0^{-c}$ for $\epsilon \ll 1$ which always is in the regime $\varphi_0 \gg 1$. The case $\alpha = 0.9$ shows a break at very small ϵ from the straight line.

This behavior is in agreement with the analysis of Mercier[9] who showed that for $\varphi_0 \ll 1$,

$$S_4^2 = 8 \int_0^\infty dq\, \varphi^2(q) \sin^2 (\epsilon q^2 a^2).$$

In the $\displaystyle\lim_{\epsilon \to \infty} S_4^2 = 4 \int_0^\infty dq\, \varphi^2(q) = 2\varphi_0^2$ or $S_4 \to \sqrt{2\varphi_0}$.

It has since been shown by Jokipii[10] and others that Mercier's formula is also valid when $\varphi_0 > 1$ so long as the resultant value of $S_4^2 \ll 1$. The small ϵ limit produces

$$S_4^2 = 8\,\epsilon^2 a^4 \int_0^\infty dq\, \varphi^2(q)\, q^4$$

which diverges for the power spectra we are considering. If the power spectra fell off faster than q^{-5} for some large value of q as they must from diffusion, there would be some small ϵ below which the curve would asymptote to the straight line $\epsilon = B/\varphi_0$. We assume this value of ϵ to correspond to a diffusion cut off size $a_D \sim 30$ m. We shall assume our curves of the power spectrum are accurate out to $q = (30\,\text{m})^{-1}$. It is interesting that the expansion of $\sin^2 (\epsilon q^2 a^2)$ as a means of obtaining the small ϵ limit which leads to a rapid ϵ^2 fall off for S_4^2 (as was found for an exponential power spectrum in a previous study[1]) may be incorrect for power law spectra even if a reasonable diffusion cut-off exists.

We shall obtain the small ϵ behavior of S_4^2 by assuming that the $\sin^2 (\epsilon q^2 a^2)$ term wipes out the contribution to the integral of the low qa portion of $\varphi^2(q)$. (valid when $\epsilon q^2 a^2 \ll 1$) and that we can go directly to the asymptotic limit of the Bessel functions, where for $\alpha = 0$ we have

$$S_4^2 = 8 \int_0^\infty dq \sin^2 (\epsilon q^2 a^2) \frac{4}{L} (r_e \lambda n_o a^2)^2 \frac{\sin^2 (qa - \pi/4)}{(qa)^3}$$

$$= 6 a \varphi_o^2 \int_0^\infty \frac{dq}{(qa)^3} \sin^2 (\epsilon q^2 a^2) \sin^2 (qa - \pi/4) \ .$$

Let $t = \epsilon q^2 a^2$. Then

$$S_4^2 = 3 \ \epsilon \varphi_o^2 \int_0^\infty dt \left(\frac{\sin t}{t} \right)^2 \sin^2 \left(\sqrt{t/\epsilon} - \pi/4 \right)$$

where for small ϵ,

$$\sin^2 \left(\sqrt{t/\epsilon} - \pi/4 \right) \sim \frac{1}{2}$$

through the important part of the integrand so

$$S_4^2 = \frac{3}{2} \ \epsilon \varphi_o^2 \int_0^\infty dt \left(\frac{\sin t}{t} \right)^2 = \frac{3\pi}{4} \ \epsilon \ \varphi_o^2 \ .$$

Therefore S_4^2 falls off as ϵ rather than ϵ^2. If there were an abrupt diffusion cut-off of $\varphi^2(q)$ at $q = q_D$ then the result is unchanged if $\epsilon q_D^2 a^2 > 1$ as mentioned above. For $\epsilon q_D^2 a^2 < 1$ we recover the ϵ^2 behavior.

The $S_4 = 0.3$ contour in Fig. 3 agrees very well with a combination of the two limits like

$$S_4^2 = \frac{2 \varphi_o^2}{(1 + \frac{8}{3\pi \epsilon})} \tag{3.1.3}$$

for example. The $S_4 = 0.9$ contour in Fig. 3 has a high ϵ limit which corresponds to Mercier's $S_4 = 1 - e^{-2\varphi_o^2}$ formula. If we arbitrarily extend the formula of Mercier to all ϵ we obtain

$$S_4^2 = 1 - e^{-2\varphi_o^2 / (1 + \frac{8}{3\pi \epsilon})}$$

28

The $S_4 = 0.9$ contour from this formula corresponds to $S_4^2 = 1.66$ in Eq.

(3.1.3). So if we would plot $\varphi = 0.9 \sqrt{1 + \frac{8}{3\pi\epsilon}}$ for the $S_4 = 0.9$ contour and

$\varphi_0 = 0.2 \sqrt{1 + \frac{8}{3\pi\epsilon}}$ for the $S_4 = 0.3$ contour they would lie along the plotted contours in Fig. 3 well within the accuracy of the plots. Therefore we may say for the case of $\alpha = 0$, $\beta = 1$, that:

1. scintillation is negligible for $\varphi_0 < 0.2 \sqrt{1 + \frac{8}{3\pi\epsilon}}$

2. scintillation is Rayleigh for $\varphi_0 > 0.9 \sqrt{1 + \frac{8}{3\pi\epsilon}}$

   with a correlation length

$$\ell = 0.6 \, a/\varphi_0$$

3. If desired, the amplitude distribution for intermediate values of φ_0 could be approximated by a Ricean using

$$\varphi_{eff} = \varphi_0 / \sqrt{1 + \frac{8}{3\pi\epsilon}}$$

   if no attempt is made to correlate amplitude and phase.

Our propagation output includes a calculation of the average bit error probability, $\overline{P}_e$, for noncoherent frequency shift key (FSK) modulation according to the formula

$$\overline{P}_e = \int_0^\infty P(s) P_e(s) \, ds$$

where $P(s)$ is the probability density that the signal-to-noise ratio is s and $P_e(s) = \frac{1}{2} e^{-s/2}$ is the bit-error probability for the value s. This is evaluated by averaging $P_e(Is_0)$ for our output considering the signal-to-noise ratio to be s_0 in the absence of scintillations. For $s_0 = \sqrt{10^3}$ (15 dB), a Rayleigh distribution produces $\overline{P}_e = .03$ whereas no scintillation means $\overline{P}_e = 7.10^{-8}$ (or no error). Our results show $\overline{P}_e$ to vary with S_4. e.g., a contour of $\overline{P}_e = 10^{-2}$ follows the $S_4 = 0.8$ contour very closely.

We now skip to the case $\alpha = 1$. Fig. 5 indicates that the small ϵ behavior of the $S_4 = 0.3$ contour approaches

$$S_4^2 = C \, \varphi_0^2 \, \epsilon^2$$

whereas the $S_4 = 0.9$ contour shows a weaker ϵ-dependence and indicates a tendency to close on the $S_4 = 0.3$ contour as ϵ decreases. This behavior is similar to the case of the exponential power spectrum studied earlier[1] wherein there was focusing leading to values of S_4 greater than unity.

For our purposes the important aspect of the $\alpha = 1$ case is the fact that the $S_4 = 0.3$ contour requires a larger φ_0 than the $\alpha = 0$ case, that is φ_{eff} is larger when $\epsilon < 1$. For $\alpha = 1$ our approximate formulas for the small ϵ case diverge. We need to evaluate

$$S_4^2 = \frac{64\pi}{L} \, (r_e \lambda n_0 a^2)^2 \int_0^\infty dq \, \frac{J_2^2(qa)}{(qa)^4} \, \sin^2(\epsilon q^2 a^2)$$

$$= \frac{315\pi}{16} \, \varphi_0^2 \, \epsilon^{\frac{3}{2}} \int_0^\infty \frac{dt}{t^{5/2}} \, \sin^2(t) \, J_2^2\left(\sqrt{t/\epsilon}\right) \, .$$

The integral can be split into two parts for small ϵ

$$\int_0^\epsilon dt \, t^{\frac{3}{2}} \, \frac{J_2^2\left(\sqrt{t/\epsilon}\right)}{t^2} \approx \frac{\sqrt{\epsilon}}{160}$$

and

$$\int_\epsilon^\infty \frac{2\sqrt{\epsilon}}{\pi} \, \frac{dt}{t^3} \, \sin^2(t) \, \cos^2\left(\sqrt{t/\epsilon} - \pi/4\right)$$

$$\approx \frac{\sqrt{\epsilon}}{2\pi} \int_\epsilon^\infty \frac{(1 - \cos(2t))}{t^3} \approx \frac{\sqrt{\epsilon}}{2\pi} \, (3 - 2 \ln \epsilon)$$

producing

$$S_4^2 = \omega_o^2 \epsilon^2 \frac{(315)}{16} \left(\ln \left(\frac{1}{\epsilon} \right) + \frac{3}{2} \right).$$

To agree with the curves of Fig. 5 we must convert the ϵ dependence where $\epsilon = \frac{\lambda d}{a^2(\alpha=1)}$ to that of the figure where the curves are plotted for

$$\epsilon_o = \frac{\lambda d}{a^2(\alpha=0)} = \frac{2\lambda d}{a^2(\alpha)} = 2\epsilon \quad \text{so}$$

$$S_4^2 = \frac{\omega_o^2 \epsilon^2}{64} (315) \left[\ln \left(\frac{2}{\epsilon_o} \right) + \frac{3}{2} \right].$$

In contrast to the $\alpha = 0$ case we will need

$$\omega_o = 0.2 \sqrt{1 + \frac{128}{315 \, \epsilon_o^2 \left[\ln \left(\frac{2}{\epsilon_o} \right) + \frac{3}{2} \right]}}$$

to have $S_4 = 0.3$ which becomes larger than the ω_o required for $\alpha = 0$ by as much

as a factor $\sqrt{\dfrac{16\pi}{105 \, \epsilon_o \left[\ln \left(\frac{2}{\epsilon_o} \right) + \frac{3}{2} \right]}}$ for small ϵ_o which is 7.25 for $\epsilon_o = 10^{-3}$.

Since the 0.9 contour appears to have an $\epsilon^{\frac{3}{2}}$ behavior from the figure, the Mercier type extension used in the $\alpha = 0$ case will not work here. However, the correspondence of systems-related parameters such as $\overline{P}_e$ with S_4 breaks down also. This is because the focusing effects caused by shapes whose power spectra decrease more rapidly than q^{-3} lead to large values of S_4 from focusing rather than from deep nulls.

A check of the $\overline{P}_e = 10^{-2}$ contour shows it to follow the curve

$$\omega_o = 0.9 \sqrt{1 + \frac{128}{315 \, \epsilon_o^2 \left[\ln \left(\frac{2}{\epsilon_o} \right) + \frac{3}{2} \right]}} \tag{3.1.4}$$

31

(a factor of 4.5 higher than for the $S_4 = 0.3$ curve) closely enough for our purposes.

This fit becomes very inaccurate for $\epsilon \leq 3 \cdot 10^{-3}$ as the $\overline{P}_e = 10^{-2}$ contour begins to approach the $S_4 = 0.9$ contour but this region ($\epsilon \leq 3 \cdot 10^{-3}$) is also the region where the greatest differences occur between the $\alpha = 1$ and $\alpha \neq 1$ cases so modeling it accurately for $\alpha = 1$ is not necessary.

Figure 4 for $\alpha = 0.9$ illustrates this point. The S_4 contours are similar for $\epsilon \geq 10^{-2}$ and begin to differ for $\epsilon \lesssim 3 \cdot 10^{-3}$. Note the $S_4 = 0.3$ contour begins to fall off slower with ϵ approaching the ϵ-dependence found for the $\alpha = 0$ case. This is because the high wavenumber portion of the PSD for $\alpha = 0.9$ has the q^{-3} behavior of the $\alpha = 0$ case. For $\alpha < 0.9$, the q^{-3} behavior appears earlier (lower q) and one never has the q^{-5} behavior of $\alpha = 1$ since this would occur at a value of q too low for the Bessel functions to be replaceable by their asymptotic expansion limits.

For $0.9 < \alpha < 1.0$, the q^{-3} behavior appears at larger values of q causing the $S_4 = 0.3$ contour to differ from the $\alpha = 1$ behavior at values of ϵ below the limit on the figure. Since both the $\alpha = 0.9$ and $\alpha = 1$ contours of $\overline{P}_e = 10^{-2}$ break from the expression (3.1.4) for $\epsilon \leq 3 \cdot 10^{-3}$, we expect the same type of break to occur for $0.9 < \alpha < 1.0$. This low ϵ break will not be modeled at this time for the $0.9 < \alpha < 1$ case since we do not expect to be in this low ϵ regime when $\beta = 1$. That is, values of ϵ this low occur at early times after burst when $\beta \neq 1$. We shall therefore approximate the results of this section with the following functional fit. Let

$$g(\epsilon_0) = (1-\alpha^2)^2 \, \frac{3\pi \epsilon_0}{8} + \alpha^4 \, \frac{315}{64} \, (1-\alpha^2/2) \, \epsilon_0^2 \left[\ln\left(\frac{2}{\epsilon_0}\right) + \frac{3}{2} \right]$$

and define

$$\omega_{eff} = \omega_0 / \sqrt{1 + \frac{1}{g(\epsilon_0)}} \quad .$$

The limit of scintillation effects ($S_4 = 0.3$) occurs for $\omega_{eff} = 0.2$. The amplitude distribution effectively becomes Rayleigh at $\omega_{eff} = 1$ with a correlation length

$$\ell = 0.6 \, a/\omega_0 \quad .$$

3.2 ELLIPTICAL CONTOUR

For a set of elliptical striations where the major axis of striation i is at an angle θ_i to the ray direction,

$$\wp^2(q) = \frac{2\pi}{L} \left(r_e \lambda n_o a^2 \right)^2 \sum_i \left[\frac{J_1(qa_i)}{qa_i} (1-\alpha^2) + 2\alpha^2 \frac{J_2(qa_i)}{(qa_i)^2} \right]^2$$

where

$$a_i = a \sqrt{\frac{\cos^2\theta_i}{\beta} + \beta \sin^2\theta_i} = \frac{a}{\sqrt{\beta}} \sqrt{1 + (\beta^2 - 1)\sin^2\theta_i} \ .$$

The electron content of each striation is independent of β and θ_i so as before $a(\alpha) = a(0)(1-\alpha^2/2)^{-\frac{1}{2}}$ for the content to be independent of α. Each striation then produces a phase variance

$$\varphi_{oi}^2 = \frac{4\pi}{L} \frac{(r_e \lambda n_o a^2)^2}{a_i} \int_0^\infty a_i dq \left[\frac{J_1(qa_i)}{qa_i}(1-\alpha^2) + 2\alpha^2 \frac{J_2(qa_i)}{(qa_i)} \right]^2$$

$$= \varphi_{oi}^2 (\beta=1) \sqrt{\frac{\beta}{1 + (\beta^2-1)\sin^2\theta_i}} \equiv \Gamma \varphi_{oi}^2 (\beta=1) \ .$$

The factor Γ is the scale factor for the q-dependence of $\varphi_i^2(q) = \varphi_i^2(q/\Gamma)(\beta=1)$. That is, $\varphi_i^2(o)$ is independent of β and θ_i but $\wp_i^2(q)$ is stretched a factor Γ with respect to the $\beta=1$ case. For small values of θ_i, $\Gamma > 1$ and the scintillation effects will be worse than in the $\beta=1$ case.

We illustrate this by choosing a random set of striations for a situation where the signal line-of-sight traverses the middle of a striated region. The set of values of θ_i is generated by choosing values of x_i to be random on a line $0 \le x \le 64$ km while values of y_i are random on a line $0 \le y \le 500$ km. The value of θ_i is chosen to be on the radial from the center of the striations to the position of the ith striation;

$$\tan \theta_i = \frac{x_i}{y_i} \ .$$

33

The resultant PSD for $\beta = 3$ is shown in Fig. 6 for the two cases $\alpha = 0, 1$. In this figure we do not need to plot the loci of peaks of the Bessel functions since the range of values of θ_i smear out the far nulls much as a distribution over sizes would. The first few nulls are not smeared out much because the range of θ_i is small. The dashed lines are fits to the curves used for the propagation. The behavior at large ν ($\nu = q/2\pi$) will be proportional to $(\nu/\nu_0)^{-3}$ for $\alpha = 0$ and $(\nu/\nu_1)^{-5}$ for $\alpha = 1$. Since the PSD, $P(\nu)$, is normalized to unity in the figure at $\nu = 0$, we have for $\alpha = 0$

$$P(\nu) = \frac{1}{M} \sum_{i=1}^{M} \left[\frac{2J_1(2\pi\nu a/\Gamma_i)}{(2\pi\nu a/\Gamma_i)} \right]^2$$

$$\approx \frac{1}{2\pi^4 \nu^3 a^3} \quad \frac{1}{M} \sum_{i=1}^{M} \Gamma_i^3$$

or

$$\nu_0 = \frac{\overline{\Gamma_i^3}^{\frac{1}{3}}}{(2\pi)^{\frac{4}{3}} \pi a} \quad .$$

For $\alpha = 1$

$$P(\nu) = \frac{1}{M} \sum_{i=1}^{M} \left[\frac{8J_2(2\pi\nu a/\Gamma_i)}{(2\pi\nu a/\Gamma_i)^2} \right]^2$$

$$\approx \frac{2}{\pi^6 \nu^5 a^5} \quad \frac{1}{M} \sum_{i=1}^{M} \Gamma_i^5$$

or

$$\nu_1 = \frac{\overline{\Gamma_i^5}^{\frac{1}{5}}}{(\pi/2)^{\frac{1}{5}} \pi a}$$

The curves are drawn for $a(\alpha = 0) = 0.282$ km and a $(\alpha = 1) = 0.282\sqrt{2} = 0.399$ km and show $\nu_0 = 0.976$ km^{-1} and $\nu_1 = 1.142$ km^{-1} so

34

Figure 6. Power-Spectral-Density (PSD) of integrated phase shift for elliptical n_e contour striations ($\beta = 3$). $\alpha = 0, 1$.

$$\overline{\Gamma_i^3}^{\frac{1}{3}} = (2\pi)^{\frac{1}{3}}(.976)\,\pi\,(.282) = 1.595$$

and

$$\overline{\Gamma_i^5}^{\frac{1}{5}} = (\pi/2)^{\frac{1}{5}}(1.142)\,\pi\,(.399) = 1.567\ .$$

The closeness of these numbers show $\overline{\theta_i^2} \ll 1$ since

$$\Gamma_i^n = \beta^{n/2}(1 + (\beta^2-1)\sin^2\theta_i)^{-n/2}$$

$$\approx \beta^{n/2}\left(1 - \frac{n}{2}(\beta^2-1)\theta_i^2\right),$$

$$\overline{\Gamma_i^n}^{1/n} \approx \beta^{\frac{1}{2}}\left(1 - \frac{(\beta^2-1)}{2}\overline{\theta_i^2}\right) = 1.732\,(1-4\overline{\theta_i^2})$$

which produces the values $\overline{\theta_i^2} = .0198$ at $\alpha = 0$ and $\overline{\theta_i^2} = .0238$ at $\alpha = 1$ where the difference in these two terms are a result of higher-order terms in $(\beta^2-1)\theta_i^2$ which we dropped. Our procedure for aligning striations along a radial direction has led to the small value of $\theta_{rms} \approx 8.5°$ for the alignment of major axes with the ray direction. We expect $\overline{\Gamma} = 1.6$ is sufficiently accurate for our purposes.

We thus expect $\varphi_o^2\,(\beta=3) \approx 1.6\,\varphi_o^2\,(\beta=1)$. The contours of $S_4 = 0.3$ and 0.9 and various values of ℓ/a are shown in Fig. 7 for the $\alpha = 0$, $\beta = 3$ case. It is apparent that the behavior of the S_4 contours is similar to Fig. 3 for $\beta = 1$ and agreement is obtained by scaling the ϵ parameter by $\overline{\Gamma}^2 = 2.56$. So that

$$S_4(\varphi_o,\,\epsilon)\Big|_{\beta=3} = S_4\,(\varphi_o,\,\overline{\Gamma}^2\,\epsilon)\Big|_{\beta=1}\ .$$

The contours of ℓ/a are displaced from those in Fig. 3 and have the form $\ell/a = 0.6/(\overline{\Gamma}\,\varphi_o)$ since ℓ must scale as $\overline{\Gamma}^{-1}$. Comparison of the

36
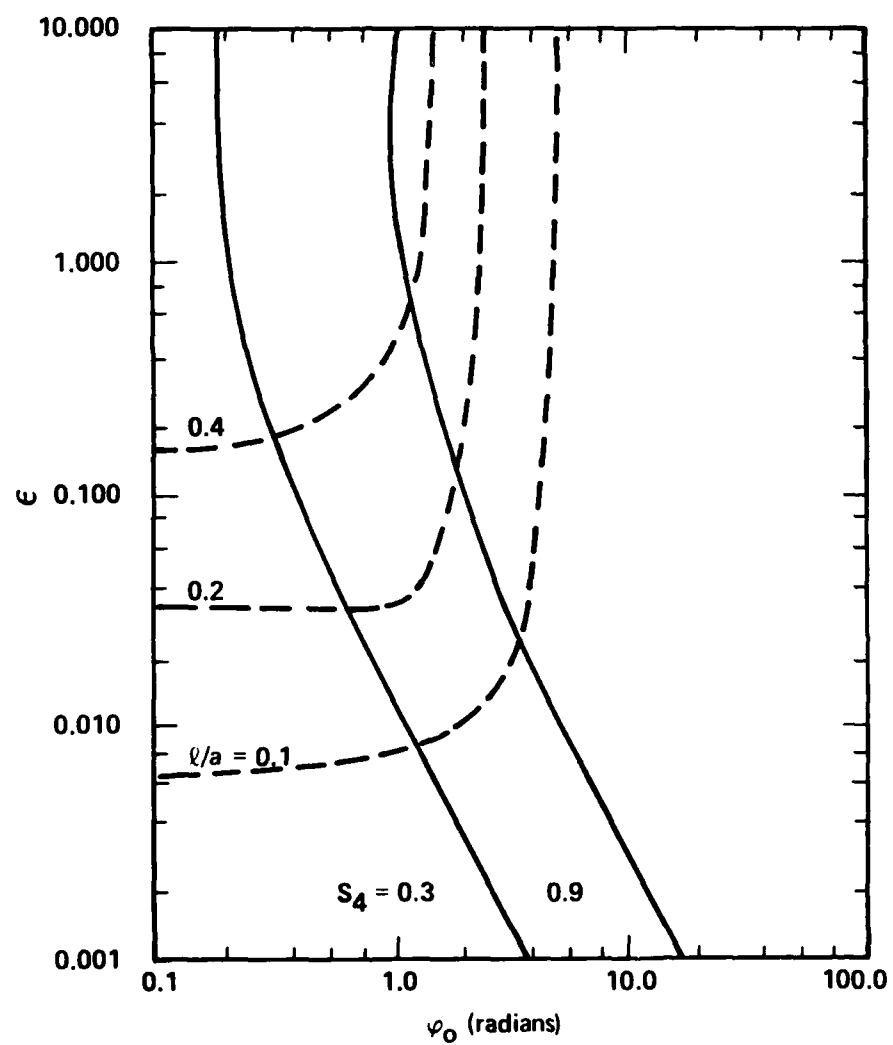
Figure 7. Contours of S_4 and ℓ/a for elliptical n_e contours ($\beta = 3$) and $\alpha = 0$.

contours in Fig. 8 for the $\alpha = 1$, $\beta = 3$ case with those shown in Fig. 5 indicates that the simple scaling agrees sufficiently even though not as well as for the $\alpha = 0$ case.

The PSD for $\beta = 10$ is shown in Fig. 9 for $\alpha = 0$ and 1. From the curves we have

$$\nu_0 = 1.377 \text{ and } \nu_1 = 1.773 \text{ which means}$$

$$\overline{\Gamma_i^3}^{\frac{1}{3}} = 2.251 \text{ and } \overline{\Gamma_i^5}^{\frac{1}{5}} = 2.4325 .$$

So the particular choice of striations causes the PSD to scale as $\Gamma = 2.25$ for $\alpha = 0$ and $\Gamma = 2.43$ for $\alpha = 1$. We have $\varphi_0 \Big|_{\beta=10} = \Gamma \varphi_0 \Big|_{\beta=1}$ and we expect the contours of S_4 and ℓ/a in Figs. 10 and 11 to scale as

$$S_4(\varphi_0, \epsilon) \Big|_{\beta=10} = S_4(\varphi_0, \Gamma^2 \epsilon) \Big|_{\beta=1}$$

and

$$\ell/a = \frac{0.6}{\Gamma \varphi_0}$$

which they do.

Because the scale factors depend on which region of the fireball is being scanned by the line-of-sight, we have chosen a stressing region where $\Gamma \lesssim \sqrt{\beta}$. There will be off-center regions where $\Gamma \approx 1$ but regions with $\Gamma < 1$ where for large β one has $\Gamma \sim \frac{1}{\sqrt{\beta}} \frac{1}{\csc^n \theta_i}^{\frac{1}{n}}$ will produce weaker scintillation effects. Regions further out will also produce weaker effects since less structure is propagated through due to the curvature of the region containing the striations. Even without the curvature effect, $\Gamma < 1$ and scintillation effects are weaker than for circular cross-sections for most of the path of the line-of-sight through the striations.

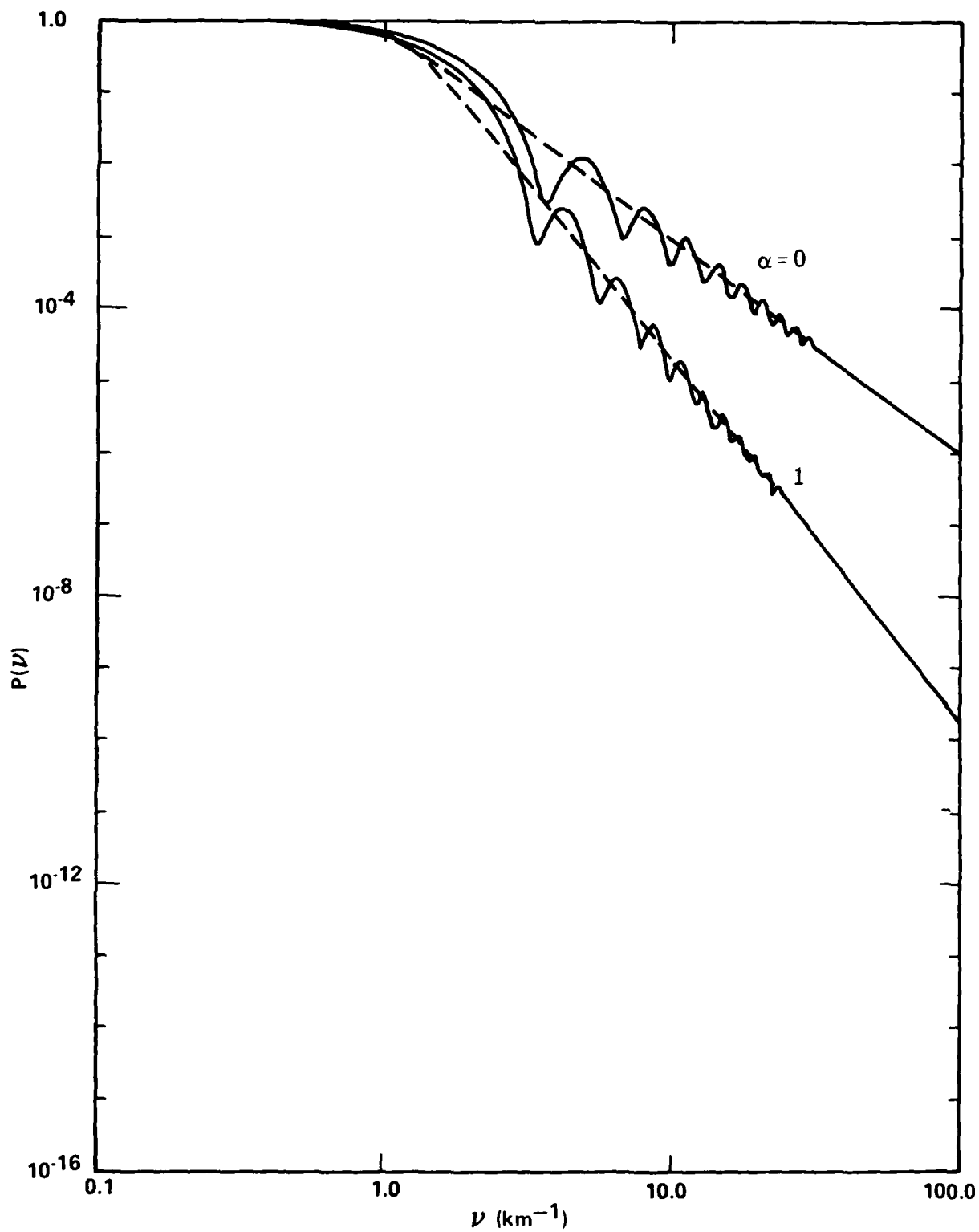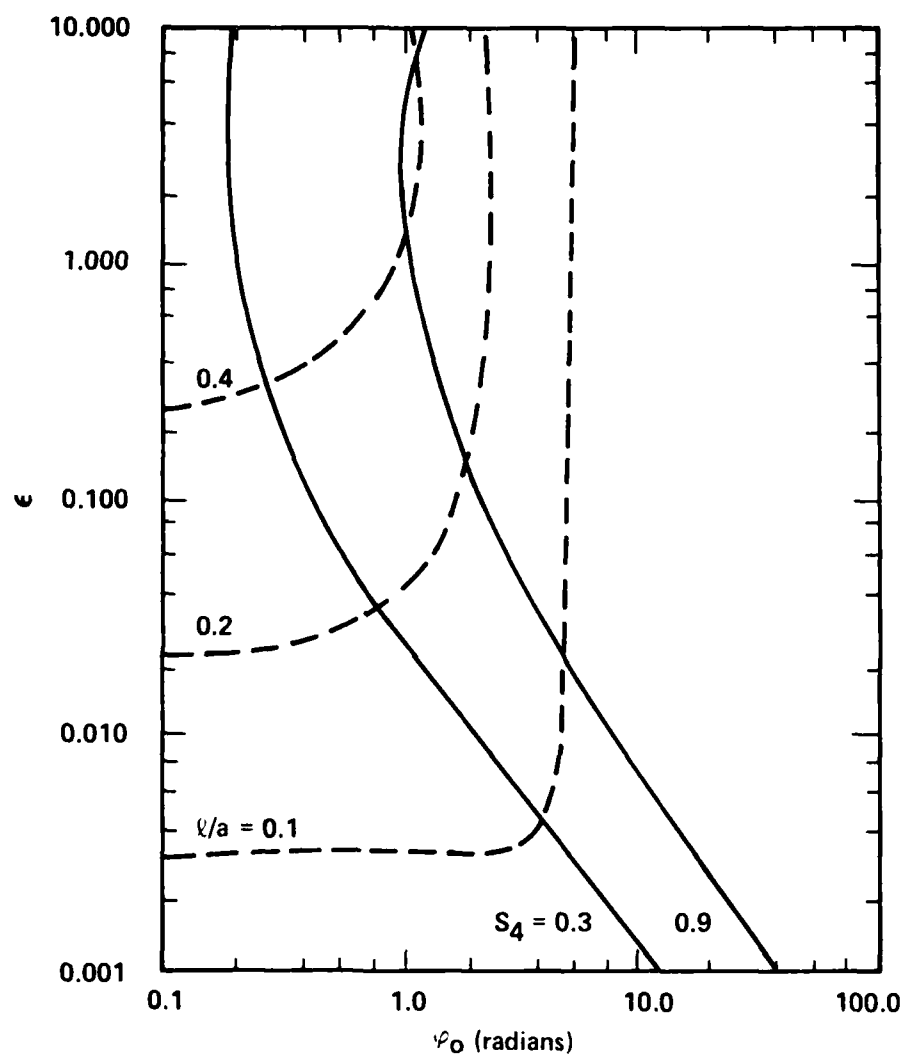Figure 8. Contours of S_4 and ℓ/a for elliptical n_e contours ($\beta \ 3$) and $\alpha = 1$.

39
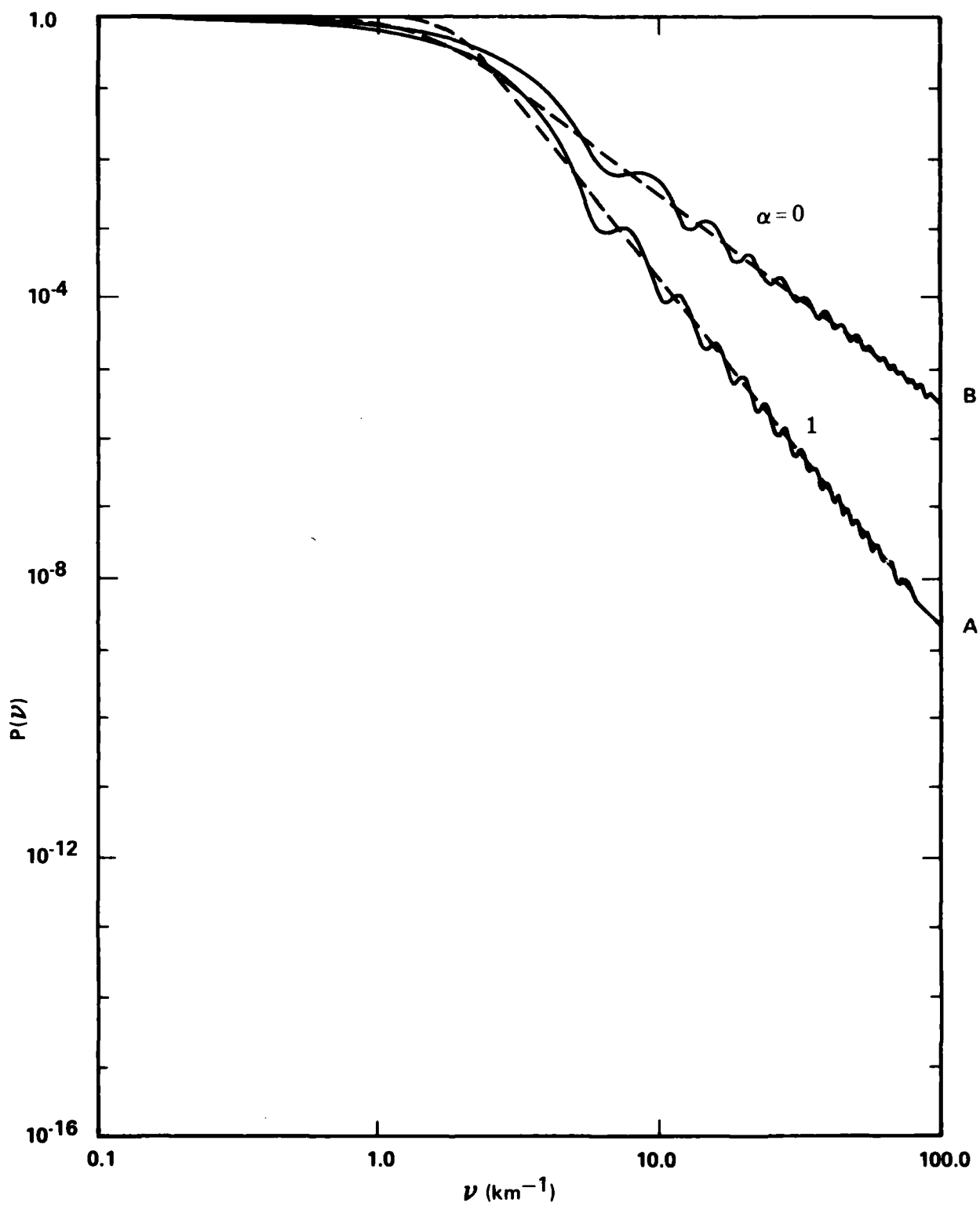
Figure 9. Power-Spectral-Density (PSD) of integrated phase shift for
elliptical n_e contour striations ($\beta = 10$) and $\alpha = 0, 1$.

40
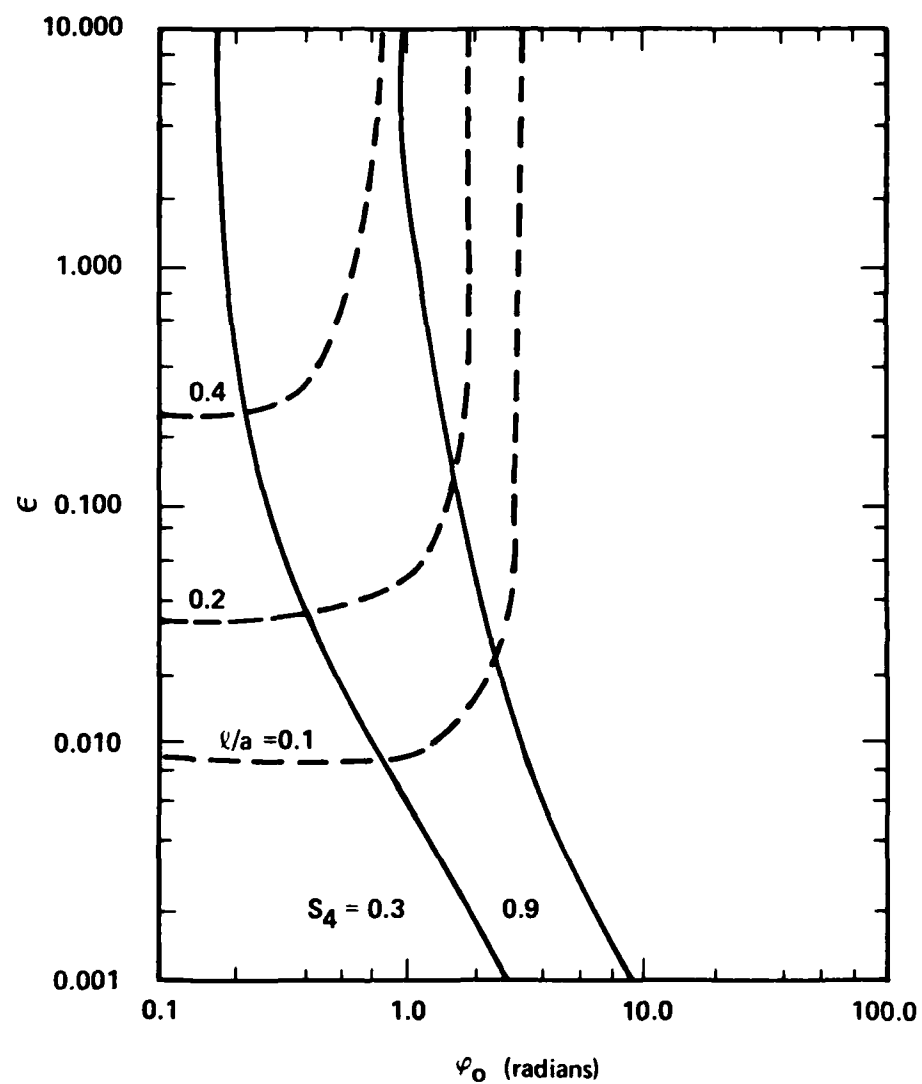
Figure 10. Contours of S_4 and ℓ/a for elliptical n_e contours ($\beta = 10$) and $\alpha = 0$.
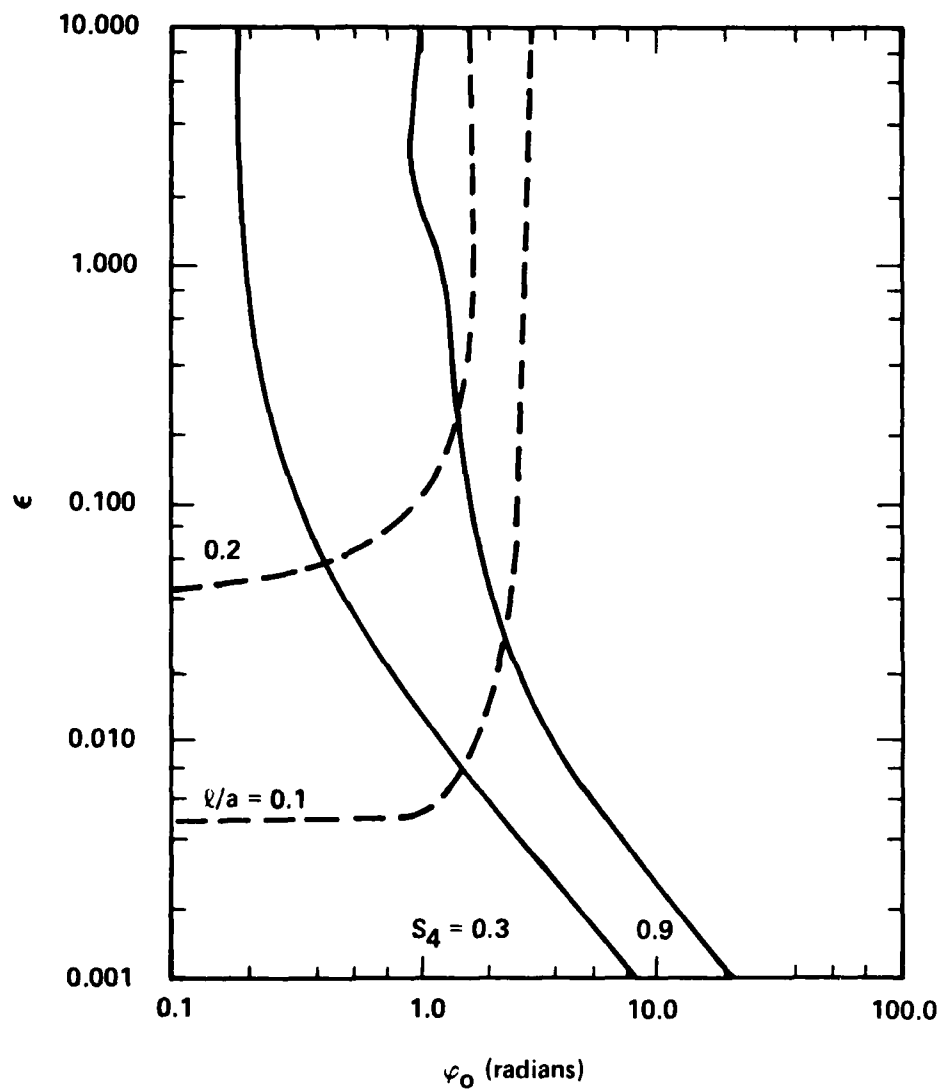
Figure 11.   Contours of S_4 and ℓ/a for elliptical n_e contours ($\beta = 10$) and $\alpha = 1$.

3.3 EFFECTS FOR A SINGLE SIZE

The general conclusions for scintillation effects are presented in terms of

$$\varphi_{eff} = \frac{\varphi_0}{\sqrt{1 + 1/g}} \qquad (3.3.1)$$

where

$$\varphi_0^2 = \frac{16 a^3 \Gamma}{3L} (r_e \lambda n_0)^2 M$$

(ignoring the slight dependence of φ_0 on α) where M is the total number of striations, $\beta^{-\frac{1}{2}} < \Gamma < \beta^{\frac{1}{2}}$, and

$$g = (1-\alpha^2)^2 \frac{3\pi \Gamma^2 \epsilon}{8} + \alpha^4 (1-\alpha^2/2) \frac{315}{64} \Gamma^4 \epsilon^2 \left[\ln\left(\frac{2}{\Gamma^2 \epsilon}\right) + \frac{3}{2} \right] .$$

For $\varphi_{eff} \gtrsim 1$, the signal distribution will be taken as effectively Rayleigh although the scintillation index, S_4, need not be unity. In this case the signal autocorrelation length

$$\ell \approx \frac{0.6 a}{\Gamma \varphi_0 \sqrt{1-\alpha^2/2}} . \qquad (3.3.2)$$

For $\varphi_{eff} \leq 0.2$, $S_4 \leq 0.3$ and amplitude scintillation is negligible. The quantity

$$\epsilon = \frac{\lambda d}{4\pi a^2} \quad .$$

The quantity a is defined by the electron content of a striation, $C \equiv n_0 \pi a^2$.

As the original content $C_0 = n_0 \pi a_0^2$ striates and bifurcates the number of striations $M = a_0^2/a^2$ so

$$\varphi_0 = 4 r_e \lambda n_0 a_0 \sqrt{\frac{\Gamma a}{3L}} \qquad (3.3.3)$$

43

decreases as a decreases. But

$$g = \frac{3(1-\alpha^2)^2}{32a^2} \Gamma^2 \lambda d + \frac{\alpha^4(1-\alpha^2/2)315}{1024\pi^2 a^4} \Gamma^4 \lambda^2 d^2 \left[\ln\left(\frac{8\pi a^2}{\Gamma^2 \lambda d}\right) + \frac{3}{2}\right] \quad (3.3.4)$$

increases as a decreases.

What are the relationships between n_o, a, α, and Γ as the original striations bifurcate? A discussion of a in Section 5 suggests the formula

$$a(t) = 0.1 + \frac{1}{2}\left[19.9 - \bar{t} + \sqrt{(19.9 - \bar{t})^2 + 0.64}\right] \quad \text{km}$$

where $\bar{t} = \frac{t - 500}{58}$ for $t \geq 500$ s. At $t = 500$ s, $a = 20$ km so for $a_o = 150$ km, $M \approx 56$. The striations should be elliptical, $\beta \sim 10$ so $0.4 < \Gamma < 2.5$ depending on the region. The profiles will be parabolic until n_e falls to a value where the integrated conductivity is a few times the background. For a 3 mho background and a 30 mho central conductivity at $n_o = 10^8$, the profile wouldn't be steep until $n_1 \sim 2 \cdot 10^7$ which corresponds to

$$\alpha = \sqrt{1 - \frac{n_1}{n_o}} = .9 .$$

For $L = 10^3$ km

$$\varphi_o(500 \text{ s}) \approx 10^3 \sqrt{\frac{a}{L}} \lambda \text{ (cm)} = 140 \Gamma^{\frac{1}{2}} \lambda \text{ (cm)} .$$

For $\alpha = 0.9$ and $d = 10^3$ km

$$g = 8.5 \cdot 10^{-8} \Gamma^2 \lambda \text{ (cm)} + 7.6 \cdot 10^{-12} \Gamma^4 \lambda^2 \left[\ln\left(\frac{10^6}{\Gamma^2 \lambda \text{(cm)}}\right) + \frac{3}{2}\right]$$

so

$$g(\Gamma^2 \lambda) \sim 8 \cdot 10^{-8} \Gamma^2 \lambda \qquad \Gamma^2 \lambda < 10^3$$

$$\sim 10^{-10} \Gamma^4 \lambda^2 \left(1 - \frac{\ln(\Gamma^2 \lambda)}{15}\right) \qquad \Gamma^2 \lambda > 10^3$$

44

For $\lambda = 10$ cm,

$$\varphi_{eff} = 1400 \; \Gamma^{\frac{1}{2}} \sqrt{g} = 1.26 \; \Gamma^{\frac{3}{2}} \quad \Gamma < 10^2$$

and the scintillation depends critically on Γ (being slight near the edge of the region and Rayleigh in the rest of the region). If n_o were 10^7, φ_o would drop to 140 producing negligible scintillation for any Γ. However the drop to 10^7 means the profile should have steepened to $\alpha = 0$ where

$$\sqrt{g} = \frac{\Gamma}{10a(km)}$$

and

$$\varphi_{eff} = .7 \; \Gamma^{\frac{3}{2}}$$

with little benefit.

The fireball region is thus a region of high scintillation even for large striations of 20 km size for $\lambda = 10$ cm. The equation set (3.3.1-3.3.4) describes the amplitude scintillation as a function of the parameters n_o, λ, L, d, a, a_o, α, and $\Gamma(\beta)$. We expect α and β to depend on n_o, background and time. We have thus far treated a case where all striations have the same size. We will investigate the effects of a size distribution on scintillation in a later report. The effects of a size distribution on the PSD are discussed in Section 5. We have shown in this section that amplitude scintillation effects can be approximated using analytic fits to the PSD.

45

4. TIME-DEPENDENT STRIATION DEVELOPMENT

4.1 DISCUSSION OF STRIATION DEVELOPMENT IN HANE

The gradient-drift instability mechanism has been combined with the output of hydrocodes of HANE in order to determine those regions of space and time after burst during which significant amplification of irregularities in the electron density can be expected. Generally speaking, these various studies have shown that the region of space 200 to 400 kilometers away from the center of the electron density distribution tends to have striation amplifications in the $10^2 - 10^3$ range by times of the order 300 to 600 s after burst. Consistent with the often made assumption that the initial amplitude of fluctuations in electron density are of order $10^{-3} - 10^{-2}$ times the unperturbed electron density, the nominal time at which the irregularities in electron density become nonlinear, i.e., $\Delta n_e / n_e$ of order 1, can be taken to be 500 seconds after burst certainly to within a factor of 2.

Unfortunately, our present understanding of the initial phase of striation development is not sufficient for us to specify precisely the form and scale sizes that are likely to be generated by the gradient-drift instability mechanism. We know that these scale sizes are considerably smaller than the typical 50 - 100 km sizes used in the hydrocode computations. The scintillation effects to be expected from HANE depend critically on the characteristics of the striations. The previous section has indicated the dependence of propagation effects on some of these currently unknown parameters. In the discussion below we will describe those aspects of striation development for which we have an understanding as well as identify gaps in our knowledge. The result of the discussion provides the motivation for the parameterized models that were discussed in Section 2 and formed the basis for the computations in Section 3.

Figure 1(B) provides a schematic illustration of the electron density contours at times around 500 seconds after burst after the initially fairly smooth electron density contours become highly distorted. The striations are formed

47

in part by motion of regions of high electron density to a greater radius than the hydrocodes would have transported them, and in part, by motion of regions of lower electron density in towards the center of the electron density distribution. We do not know precisely the configurations to be expected at this time in the cylindrical geometry with a radial neutral wind that is a function of radial distance. However, we summarize below our current understanding regarding scale sizes, shapes, and the time evolution of striations and place bounds on the range of values to be expected.

4.1.1 Initial Development

The analytical[11] and numerical[12, 7] studies of one-dimensional clouds have some relevance for the cylindrically symmetrical problem. The unperturbed equilibrium in both cases has the Pedersen current flow at right angles to the density gradients which are colinear with the neutral wind velocity. There are, of course, geometric factors which lead to significant differences on the global scale for the two cases.

The gradient-drift instability[5] results from disruptions in the equilibrium current-flow-pattern due to irregularities in the field-line integrated Pedersen (FLIP) conductivity, $\Sigma(\vec{r})$. Thus, in order to determine the electric field pattern that maintains divergence-free current flow, we need to know the distribution of the FLIP conductivity. Consistent with the smooth electron density contours shown in Figure 1(A) before striation formation, we may model the radial distribution of the Pedersen conductivity as

$$\Sigma(r) = \Sigma_o [1 + \varkappa \exp(-r^2/a_o^2)] \qquad (4.1)$$

where Σ_o represents the FLIP conductivity of the uniform background. Σ_o for the ambient ionosphere has typical values of 1 - 10 mho depending on time of day. Values of $\varkappa$ appropriate for HANE will be discussed below.

During the initial stages when the fluctuation amplitudes are small, the development of the irregularities can be treated by linearized equations. The

48

problem with attempting to apply these results to HANE is that the unperturbed electron density (and conductivity) is inhomogeneous and time-varying. Thus, the changes in the electron density contours are due in part to the description provided by the linearized-growth-analysis and in part to changes occurring in the evolving electron density distribution. The latter influences the validity of the linearized-growth-analysis.

The linearized analysis of a one-dimensional cloud has most validity when applied locally. Perkins et al.[11] analyzed the stability in the limit $kh \gg 1$ where k is the Fourier wave-number of the perturbed density in the direction of the current flow and $h = | \nabla \ln \Sigma |^{-1}$ is the gradient length associated with the spatial dependence of $\Sigma(r)$. The principal results obtained by Perkins et al. of interest here relate to the location, shape, and growth time of the perturbed density. They find that the eigenfunction maximizes at the position $r = r_m$ for which h is a minimum, h_m, (maximum in the logarithmic gradient). The striation is elongated in the direction of the neutral wind, $\vec{V}_n$, with a length that is $\beta = (2kh_m)^{\frac{1}{2}}$ times the transverse width, $1/k$. The time scale for exponential growth is

$$\tau_g \sim (h_m/V_s) [1 + (1/kh_m)] \tag{4.2}$$

where V_s is the magnitude of the slip velocity of the neutrals, $\vec{V}_s = \vec{V}_n - \vec{V}_i$, transverse to the magnetic field. Because diffusion coefficients are generally small, diffusion is not likely to be a dominant process until late times when large density gradients have formed.

Table 4.1 shows some of the characteristic numbers that result when the conclusions from the linearized analysis are applied to the cases of both planar clouds, shown above the dashed line, and cylindrical clouds associated with HANE, shown below the dashed line. The cases above the dashed line are chosen to represent the parameters associated with the numerical simulations of NRL[6,7] when applied to clouds having a conductivity profile given by Eq. (4.1). The third column gives the position of the maximum in the eigenfunction predicted by linear theory. We see that for higher conductivity ratios this

Table 4.1 Cloud characteristics associated with initial striation development

1	2	3	4	5	6	7	8	9	10	11
χ	a_o (km)	r_m (km)	χe^{-z_m} $z_m = r_m^2/a_o^2$	ℓ_m (km)	π/k (km)	kh_m	kr_m	h_m/V_s (s)	t (s)	$A = e^{t/\tau_g}$
1	8	7	0.5	14.4	1.2	38	-	144	480	2.8×10^1
10	8	10	2.1	4.7	2.0	12	-	47	240	1.6×10^2
-	-	-	-	-	-	-	-	-	-	-
3	150	150	1.1	140	40	11	12	140	500	3.5×10^1
10	150	190	2.1	90	40	7	15	90	500	2.6×10^2
100	150	260	5.0	50	40	4	20	50	500	2.2×10^4
1000	150	330	8.6	40	40	3	26	40	500	2.7×10^5

maximum relative deformation occurs further out from the region of peak density toward the tail of the Gaussian. Column 4 gives the value of the cloud conductivity in units of Σ_0 at the position of the maximum. Even for clouds with very high peak conductivity ratios, the density contours that deform most rapidly correspond to a value of cloud conductivity of order the background conductivity.

Column 5 lists the minimum value of the logarithmic density gradient length that occurs for each of the cases. Column 6 indicates the characteristic full-width of the striations. In the planar cloud cases above the dashed line, the values given are obtained from the observation that in the 12 kilometer dimension shown, there were 5 and 3 striations growing initially, in the two cases respectively. This dimension is also consistent with the full-width after the striations have become nonlinear. In the HANE cylindrical cloud case shown below the dashed line we have just given characteristic numbers associated with a striation of a characteristic radius a = 20 kilometers. The seventh column shows that these numbers imply that $kh_m \gg 1$. The eighth column provides an estimate of the number of such 20 kilometer size striations that might exist around the cylindrical radius of $r = r_m$. The characteristics growth time, $\tau_g \sim h_m/V_s$ is shown in column 9 where for the planar cloud case a velocity of 0.1 km/s was used while in the HANE case a typical velocity of 1 km/s was used.

We now compare the numbers relevant for the linearized analysis shown in Table 4.1 with numerical simulations of the planar cloud case. Figures 12 (from Ref. 7) and 13 (from Ref. 6) illustrate the $\varkappa = 1$ (at t = 480 s) and $\varkappa = 10$ (at t = 240 s) cases, respectively. In each of these figures the maximum distortions of the equal density contours are comparable to the size of the striations which is a criterion that the distortions are ending the linear phase and entering the nonlinear phase. Note that the positions of the maximum distortions are located at a distance further from the maximum density in the case of the higher conductivity ratio. At the times indicated in column 10 of Table 4.1, the initial fluctuation amplitudes of 5% and 3%, respectively, will have been amplified by the factor A shown in column 11. This amplification is sufficient that the linearized theory is no longer applicable and the striation development has entered the nonlinear regime consistent with the distortions shown in the respective figures.

51

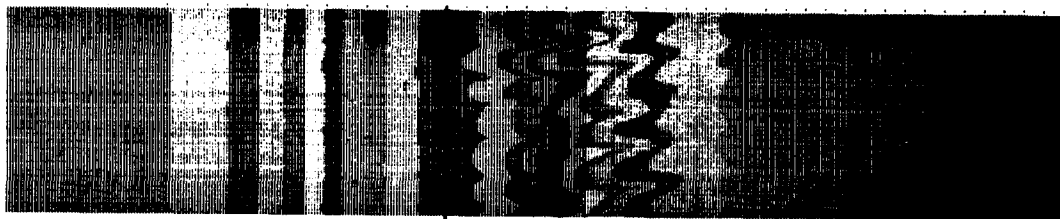Figure 12.   Iso-Pedersen conductivity contours of a one-dimensional
plasma cloud with $\varkappa = 1$ at $t = 480$ s after initial perturbation
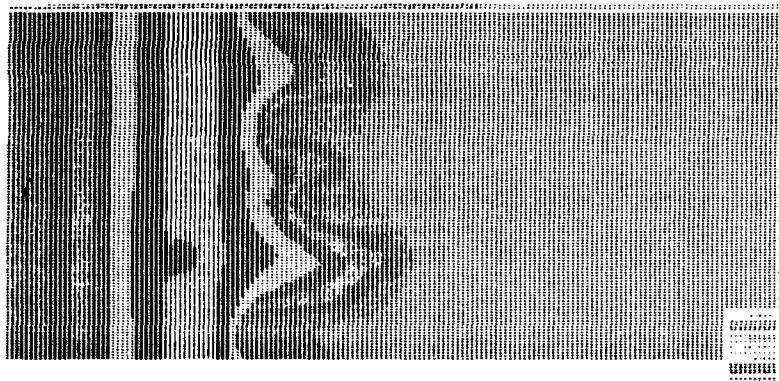amplitudes of $\sim 5\%$ (taken from Ref. 7).

Figure 13.   Iso-Pedersen conductivity contours of a one-dimensional
plasma cloud with $\varkappa = 10$ at $t = 240$ s after initial perturbation
amplitudes of $\sim 3\%$ (taken from Ref. 6; $R_e = \infty$ case).

At late time in the nonlinear regime, the above description is not appropriate. In that regime the striations do not increase in amplitude exponentially with time but maintain a nearly constant electron density. The striations move with a velocity that is dependent on the local slip velocity and the ratio of the FLIP conductivity of the striation to the FLIP conductivity in the background region in the vicinity of the striation. Furthermore, these isolated striations undergo additional deformations that are sometimes simply described as bifurcations. We will discuss the time-scale for these bifurcations in Section 4.1.2 below.

We do not have an adequate understanding of the transition between the linear regime and the nonlinear regime except in highly idealized cases. Crucial questions regarding the scale size of the striations and the time scale for their development require further study.

If an initially planar cloud is seeded with perturbations having a periodicity equal to $2\pi/k$, then both linear[11] and nonlinear[12] analyses show that the resulting striations maintain this periodicity. In the linearized regime, the perturbation density grows exponentially in time with a time constant, τ_g, close to that given by Eq. (4.2). However, linear theory so far has been unable to specify the eventual scale size of striations in the nonlinear regime. A naive interpretation of the linear theory would indicate that, according to Eq. (4.2), the smallest striation scale size would grow the most rapidly. It would also indicate that for the case of large conductivity clouds the striation growth would affect primarily the low density regions of the cloud, near $r = r_m$ where r_m is the location of the maximum in the eigenfunction.

However, as the striations approach the nonlinear regime neither of the above conclusions is correct. The small scale perturbations which, according to linear theory, grow the fastest also "saturate" the fastest. Larger scale striations which continue growing then dominate the smaller scale structures. The influence that the value of the cloud conductivity ratio, x, the density profile of the cloud, connections to other layers of ionization on the same magnetic field line, and possibly diffusion, have on the important problem of specifying the scale size of nonlinear striations has not yet been determined.

53

In regard to the striation scale sizes that we might expect from HANE from the available examples, it would appear that it is reasonable that the initial values would be in the range $3 \leqslant kh_m \leqslant 30$. This result would give initial characteristic striation half-widths, $a = \pi/2k$, in the range from several kilometers to several tens of kilometers. Furthermore, an examination of column 11 of Table 4.1 indicates that by times of around 500 s following burst, the amplification factors are generally in the range consistent with code calculations. Both the simplified model and the more extensive code calculations indicate that the initially linear striations have become nonlinear by approximately 500 s.

4.1.2   Nonlinear Development

We now turn to a discussion of some of the expected characteristics of striations when they are in the nonlinear phase. For the case of HANE we assume that the striations have reached the nonlinear phase at times greater than 500 s after burst. We will discuss some concepts related to the initial sizes of the striations, the shapes of the striations, the density profiles within the striations, and the time scale for their development. A discussion of the time development of striations is given in the next section.

Once the ionization in HANE has reached the stage shown schematically in Figure 1(B), we can apply our understanding of the processes that affect the evolution of these striations which we will characterize as having a typical scale size a. In discussing these concepts we will not include the mutual interactions between neighboring striations. This neglect will modify some of the details but will not affect the general concepts. We have already indicated that the probable size of these striations is determined by processes not fully understood during their initial stages of development. Indications are that for the case of HANE they are probably in the range of several kilometers to several tens of kilometers in scale size.

The conductivity associated with a HANE cloud is an important parameter for describing its development. During the first tens of seconds following a high altitude explosion the concept of conductivity is inappropriate because the magnetic field lines are distorted and the electrostatic approximation is not valid.

If the concept were applied unthinkingly, however, the evaluation of the FLIP conductivity would probably produce values in the range of many of hundreds to thousands of mho. However, this value would rapidly decrease with time because the neutral density decreases as a result of being heaved to higher altitudes.

The contribution to the FLIP conductivity obtained by integrating over a small height range Δ, is given by

$$\delta \Sigma = \frac{en\nu}{B\Omega} \frac{\Delta}{\sin \theta} \tag{4.3}$$

where e, n, B, ν, Ω, and θ are, respectively, the electronic charge, ion number density (equal to the electron concentration), magnetic field strength, ion-neutral collision frequency, ion gyrofrequency, and magnetic field dip angle. By using $B = 0.5$ gauss, $\Omega = 300$ s^{-1} appropriate for ions of mass 16, and $\nu = 2 \times 10^{13} \rho$ where ρ is the neutral mass density expressed in g/cm^3, (consistent with an approximate effective collision cross section of $\sim 5 \times 10^{-15}$ cm^2), and $\theta \sim 70^\circ$, we obtain

$$\delta \Sigma \sim 2.3 \times 10^5 \, n\rho\Delta \text{ mho} \tag{4.4}$$

where n and Δ are expressed in units of cm^{-3} and km, respectively. As an example, the FLIP conductivity of a plasma cloud produced by a 48 kg barium release at ~ 10 minutes after release when $n \sim 10^7$ cm^{-3}, $\Delta \sim 25$ km, and $\rho \sim 4.5 \times 10^{-13}$ g/cm^3, is ~ 26 mho when Eq. (4.4) is used. This value is in excellent agreement with more detailed estimates given in Ref. 13.

Accurate values of the FLIP conductivity of a HANE cloud as a function of time can be obtained from late-time electrostatic codes such as MELT, but these values are not currently part of the output. It is difficult to make accurate estimates by using Eq. (4.4) because both n and ρ vary by many orders of magnitude along a magnetic field line and this variation changes with time. However, we have attempted to use the expression given in Eq. (4.4) to get crude estimates of the range of expected FLIP conductivities. We have examined typical outputs of the MELT code at times of 500, 1000, 1500, and 2000 seconds after a burst. Because many neutrals have been heaved to high altitude, it

appears that at 500 s, the FLIP conductivity $\sim$ 100 mho. By 1000 s, it appears that this value may have decreased by an order of magnitude or more. For the time-scale 500 - 2000 s after burst the FLIP conductivity of the large cloud of ionization created by a high altitude nuclear burst is of order 10 - 100 mho.

Forty-eight kilogram barium releases at altitudes of 180 to 190 km produce clouds of ionization that have a FLIP conductivity of order 30 mho[13], and a typical scale size a $\sim$ 3 km. Thus, it is reasonable to expect that some of the observed behavior of barium releases conducted in the ionosphere at dusk may provide appropriate descriptions of the subsequent development of the large scale striations shown in Figure 1(B), particularly at later times. The scale size of a 20 km striation in HANE is approximately a factor of 7 larger than a 3 km barium cloud. However, at late times in the 1000 s time range following a burst, the neutral wind velocity at several hundred kilometers radius from the burst field line is of order 500 m/s which is a factor of 7 larger than a typical ionospheric neutral wind velocity of 70 m/s. Thus, the time scale for the subsequent development of the large-scale nonlinear striations that can be assumed to be present at 500 seconds after burst is in the same range as the time scale for the development of smaller-scale ionospheric barium clouds. Each of the clumps shown in Figure 1(B) is likely to develop in a manner very similar to typical barium clouds such as Spruce or those released during the STRESS test series.

Barium releases conducted in Florida during winter behaved as though the ratio of cloud to background FLIP conductivity were in the range of 3 to 6, so we estimate the effective ionospheric conductivity to be 5 to 10 mho. These values are significantly greater than is expected from a nighttime ionosphere which should be in the range of 1 mho. The larger value is explained by the hypothesis that the polarization electric fields induced by the presence of the barium cloud is projected along the magnetic field lines into the daytime (in the case of Spruce) or late afternoon (in the case of the STRESS test series) ionosphere in the southern conjugate region[14]. Thus, the appropriate background ionospheric conductivity, Σ_0, to use in Eq. (4.1) may range from a low of the

order of 1 mho up to a high in the 10-20 mho range corresponding to the presence of nighttime or daytime ionospheres. The appropriate value of x in Eq. (4.1) for HANE may range from $\leqslant 1$ at late-time for a daytime burst to possibly as large as > 100 at 500 s for a nighttime burst. The strong suggestion is made that rather than providing just a simulation of gradient-drift physics, observations of barium clouds may provide a direct visualization of the equivalent development of structure for some cases in HANE.

We now discuss various characteristics of the striations in the nonlinear regime. The first characteristic is the peak electron concentration in the striations. Striations are formed by the tendency for the regions of large conductivity to become more coupled to the neutral wind. Thus, the peak electron concentrations in striations are essentially comparable to the peak electron concentrations that are provided by the output of the large-scale codes. Many of the striations will have electron concentrations of order 10^8 cm^{-3} for thousands of seconds.

The shape and profile of the striations depend on the conductivity ratio x. We have already discussed the uncertainty in our knowledge of the initial scale size of the striations, but as we discussed in the previous subsection, we expect values of kh_m in the range of 1 - 100. During the first 500 s when we expect the conductivity of the burst-produced ionization to be very large, an examination of the tabulations given in Table 4.1 suggests initial scale sizes of striations from kilometers to several tens of kilometers. Associated with this range of striation scale sizes, we expect an initial ratio of length to width, defined earlier as the parameter β, in the range from 1 to 10. Two sets of arguments lead to this conclusion. First, the linear theory provides an estimate $\beta \sim (2\,kh_m)^{\frac{1}{2}}$ when $kh_m \gg 1$ which is consistent with $1 \leqslant \beta \leqslant 10$. So, from linear theory one expects elongated initial striations. The second argument follows from an analysis of the polarization electric field pattern associated with nonlinear striations. For large conductivity ratios, the rate of steepening of the original high density contours in the direction of the neutral wind is much lower than for moderate conductivity ratios. Thus, after the nonlinear striations have been formed, the typical length in the direction of the neutral wind may be a reflection of the original scale size in that direction, i.e., a dimension of order 150 km. If, indeed,

57

the dimension of the striations in the radial direction were this large, then it is easy to imagine values of $\beta \sim 10$.

Now we discuss the profile of the electron density within a striation. A principal feature of plasma cloud dynamics is the steepening of the backside of a plasma cloud. However, this steepening phenomenon is most prominent for those parts of the cloud or striation that have values of conductivity less than several times the background conductivity Σ_o. Conclusions drawn from both linear and nonlinear theory support this claim. From linear theory we pointed out when we discussed column 4 in Table 4.1 that the values of the conductivity at which the linearized perturbation amplitude is largest occurs for those values of conductivity that are only a few times the background value even when the peak conductivity is extremely large, i.e., relatively low-valued density contours undergo initial maximum deformation.

Arguments from nonlinear analyses rely on the realization that steepening occurs as a result of shear flow. In the electrostatic approximation that is applicable for the description of striation development, the shear in the flow exists because of gradients in the electric field. Gradients in the electric field result from the presence of polarization charges whose magnitude and location are determined by Poisson's equation. In the simplified one-layer model, the requirement that

$$\nabla \cdot \vec{J} = 0 \quad \text{where} \quad \vec{J} = \Sigma \, (\vec{E} + \vec{V}_n \, x \, \vec{B}) \tag{4.5}$$

is the field-line-integrated current density across $\vec{B}$ can be written as

$$\nabla \cdot \vec{E} = - \, (\vec{E} + \vec{V}_n \, x \, \vec{B}) \cdot \nabla \ln \Sigma \, (\vec{r}) \, . \tag{4.6}$$

This equation indicates that the extremes in the gradients of $\vec{E}$ are at the positions where $h = |\nabla \ln \Sigma|^{-1}$ is a minimum. An examination of column 4 of Table 4.1 shows that even for large κ, this position occurs at relatively low values of conductivity. Hence, we expect those portions of the striations that have FLIP conductivities only a few times the background to develop large density gradients. However, if the conductivity ratio associated with the peak electron concentration is of order 10 or more, we expect the steepening rate of the high

58

density portions of the striation to be considerably less than that of the low density portions[15].

Numerical solutions of the nonlinear equations[6,7], corresponding to the cases $\varkappa = 1$ and 10, support these comments. For the low conductivity case considered in Ref. 7, the density gradients developed at late times are significantly larger than the original density gradients present initially. However, the late-time density contours in Ref. 6 for $R_e = \infty$ indicate that large density gradients are developed only on the outermost density contours. The density gradients in the direction of the neutral wind in the vicinity of the peak conductivity are similar to those present initially, and have not steepened appreciably. Hence, in the case of striations whose conductivity ratios exceed 5, it is appropriate to describe the density profile as having a small gradient until the conductivity falls to several times the background conductivity at which point the density gradients become exceedingly large. These remarks refer primarily to gradients in the direction of the neutral wind. In both high and low conductivity cases, however, very large density gradients are developed in the direction transverse to the direction of elongation because this is the region where the shear flow is the greatest.

One might suspect that diffusion would prohibit the development of very large density gradients. However, a simple plasma model calculation shows that this conclusion is not correct. In fact we shall show that very large gradients in the low density region of a striation can still exist.

The continuity equation for incompressible flow with diffusion added can be written

$$\frac{\partial n_e}{\partial t} + \vec{v} \cdot \nabla n_e = \nabla \cdot D \nabla n_e \tag{4.7}$$

where

$$D = \frac{K(T_e + T_i)}{eB} \frac{\nu_e}{\omega_{ce}} \tag{4.8}$$

is the classical ambipolar diffusion coefficient for diffusion perpendicular to the magnetic field. $\omega_{ce} = 9 \times 10^6$ s^{-1} is the electron cyclotron frequency and $\nu_e = \nu_{en} + \nu_{ei}$ is the sum of the electron collision frequencies for collisions with neutrals and ions, respectively. With

$$\nu_{en} \sim 2 \times 10^{-8} \, n_o \, , \quad \nu_{ei} \sim 1 \times 10^{-3} \, n_e \qquad (4.9)$$

appropriate for $T_e \sim T_i \sim 0.1$ ev, we find that $\nu_{ei} > \nu_{en}$ for $n_e > 2 \times 10^{-5} \, n_o$. For neutral particle densities less than 4×10^9 cm^{-3} corresponding to $\rho \sim 10^{-13}$ g/cm^3, electron-ion collisions dominate electron-neutral collisions whenever $n_e > 10^5$ cm^{-3}. In this case the diffusion coefficient is proportional to n_e and it can be written approximately

$$D = \overline{D}n_e \sim 4 \times 10^{-7} \, n_e \, \text{m}^2/\text{s} \qquad (4.10)$$

with n_e in units of cm^{-3}.

We wish to examine the density profile at the tip of the striation and consider density gradients in the x-direction alone. In the frame moving with the tip of the striation, the flow in the low-density ionization exterior to a rod-like striation has a stagnation point at which we take the origin of our coordinate system. In this frame, the incompressible exterior flow field can be approximated near the stagnation point by

$$\vec{v} = - \omega x \, \hat{e}_x + \omega y \, \hat{e}_y \qquad (4.11)$$

in this planar model. The velocity shear ω has a value of order $\omega \sim V_s/a$. By combining Eqs. (4.10) and (4.11) with Eq. (4.7), we look for a profile of the electron density that satisfies the steady-state continuity equation (4.7),

$$\overline{D} \, \frac{\partial}{\partial x} \, n_e \, \frac{\partial n_e}{\partial x} + \omega x \, \frac{\partial n_e}{\partial x} = 0 \, . \qquad (4.12)$$

We have not found an analytic solution of this nonlinear inhomogeneous equation, but we have found that there is a solution for which $n_e \to 0$ as $x \to x_o$ that can

be developed as a power series expansion;

$$n_e \sim \frac{x_0^2 \omega}{\bar{D}} \left[A\left(1 - \frac{x}{x_0}\right)^{\frac{1}{2}} \left(1 - \frac{\left(1 - \frac{x}{x_0}\right)^{\frac{1}{2}}}{3A}\right)^2 + O\left(1 - \frac{x}{x_0}\right)^2 \right] \qquad (4.13)$$

where A is an arbitrary constant. This solution shows that $\vec{\nabla} n_e \to \infty$ as $x \to x_0$ and $n_e \to 0$. The constant A and the value of x_0 are determined by boundary conditions whose application requires a knowledge of the full-solution and depends on the value of n_e at $x = 0$ and the striation scale size a. The scale size for the variation in n_e at low values of density is

$$x_0 \sim \left(\frac{\bar{D} n_e(o) a}{A V_s}\right)^{\frac{1}{2}} \sim 3 \text{ m} \qquad (4.14)$$

for electron concentrations $\sim 10^7 \text{ cm}^{-3}$ and striations with $a \sim 1$ km and $V_s \sim 500$ m/s. This small value for scale length compared to a justifies the use of an abrupt fall-off in density as characterized by the parameter α in Section 2.

In summary, the discussions in this section have provided the physical basis for the models of striation shapes and density profiles that were parameterized in Section 2. It would appear that values of α and β in the ranges $0 \le \alpha \le 1$ and $1 \le \beta \le 10$ span the values that are appropriate for various bursts at certain times during the evolution of the striations. The largest uncertainty, in addition to those represented by these ranges of values, has to do with the scale size of striations to be expected. In the next section, we will discuss a model for the time dependence of the changes in the sizes and numbers of striations after the first 500 s following a nuclear burst.

4.2 DISCUSSION OF TIME-DEPENDENT STRIATION DEVELOPMENT

It is well known that, when a plasma cloud is placed into the ionosphere, it eventually develops structure that at late times has the appearance of isolated rods, called striations, aligned with the earth's magnetic field. A one-dimensional cloud that is elongated in the direction of the current flow, so that $\vec{J} \cdot \nabla \Sigma = 0$, is in equilibrium. If there were no fluctuations in the electron density it would not

break up into smaller-scale striations. However, this equilibrium configuration is unstable. If the cloud were seeded with small amplitude perturbations in electron density, these perturbations would initially grow in amplitude on the back side (the side out of which the neutral particles are flowing). If the initial seed enhancements were periodic, the developing structure would have the appearance of a periodic distribution of sheets (see Fig. 14 taken from Ref. 12). If, on the other hand, the perturbations in electron density were randomly placed, or contained a large range of scale sizes, then sheet-like protuberances of different size and amplitude would begin to grow (see Fig. 12 from Ref. 7). The striations form as a result of the tendency for the regions of maximum conductivity to move with a velocity closer to that of the neutral wind.

As the striation continues to develop it continues to have a sheet-like appearance. However, the maximum in the conductivity tends to approach the tip region of the striation and the ionization that is left behind has considerably lower values of conductivity. Since the ionization flow in the plane transverse to the magnetic field is incompressible, the width of the lower conductivity region of the sheet becomes quite thin. This fact explains the rod-like appearance of the region of higher electron density concentrated near the tip when viewed across magnetic field lines.

There is no equilibrium configuration for a two-dimensional cloud with finite conductivity gradients. The first manifestation of the distortion of the electron density contours is a steepening of the backside as the maximum in conductivity moves with a velocity closer to that of the neutral particles compared to the velocity of the lower conductivity regions. An example of these distortions is shown in Fig. 15 from Ref. 12. If two perturbations in electron density are placed on an otherwise cylindrically symmetrical two-dimensional cloud, each maximum will tend to form its own sheet and the cloud initially breaks into two pieces. This process is called bifurcation and the classical shapes that result are shown in Fig. 16 taken from Ref. 12. This bifurcation, or budding, process appears to be a common stage in the evolution of the tips of striations. These classical shapes are often seen to develop in the photographs of barium clouds taken up the field lines and in numerical simulations of late-time striations.

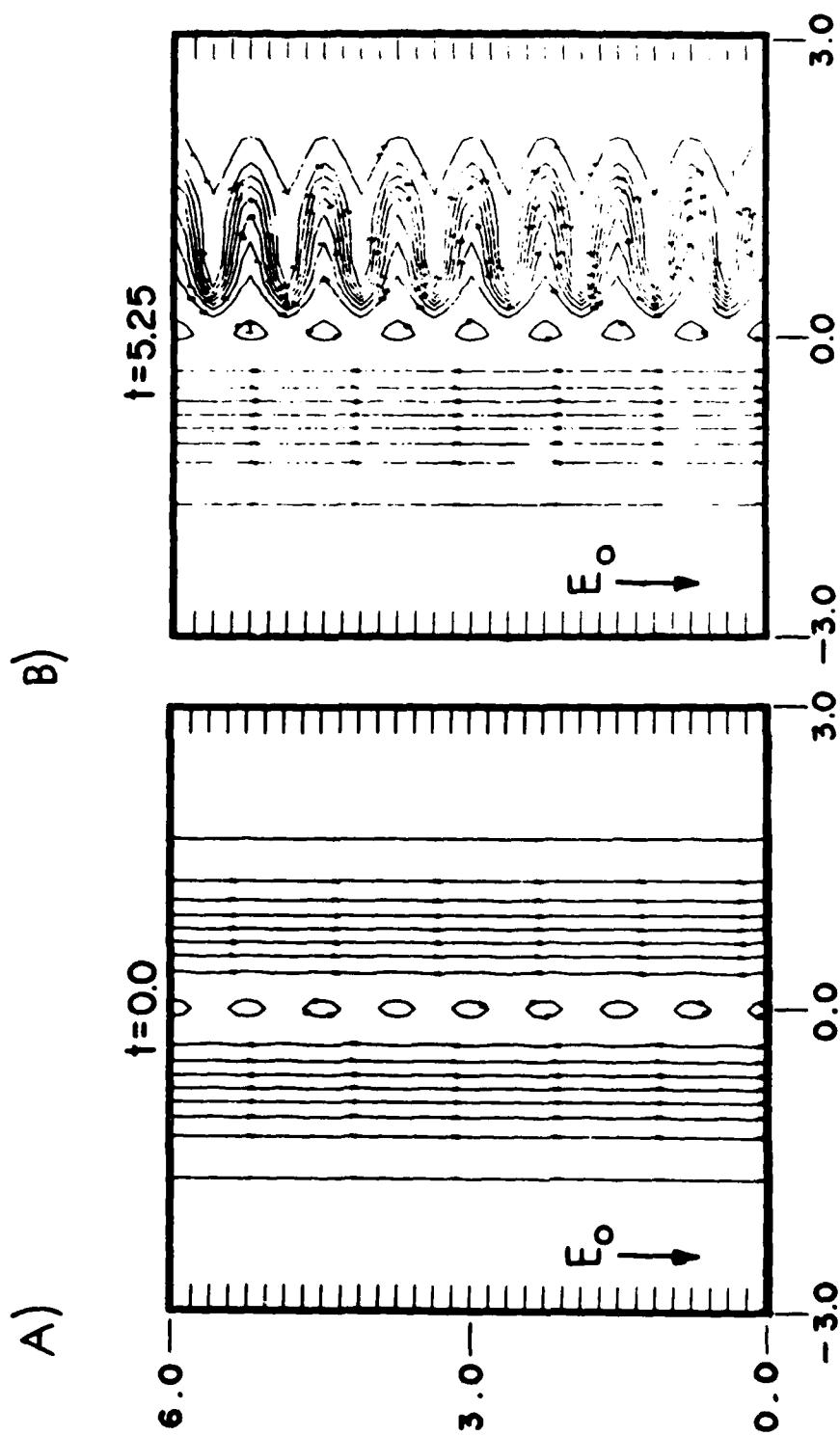Figure 14. Isodensity contours and striations for a one-dimensional cloud with a periodic initial perturbation (taken from Ref. 12).
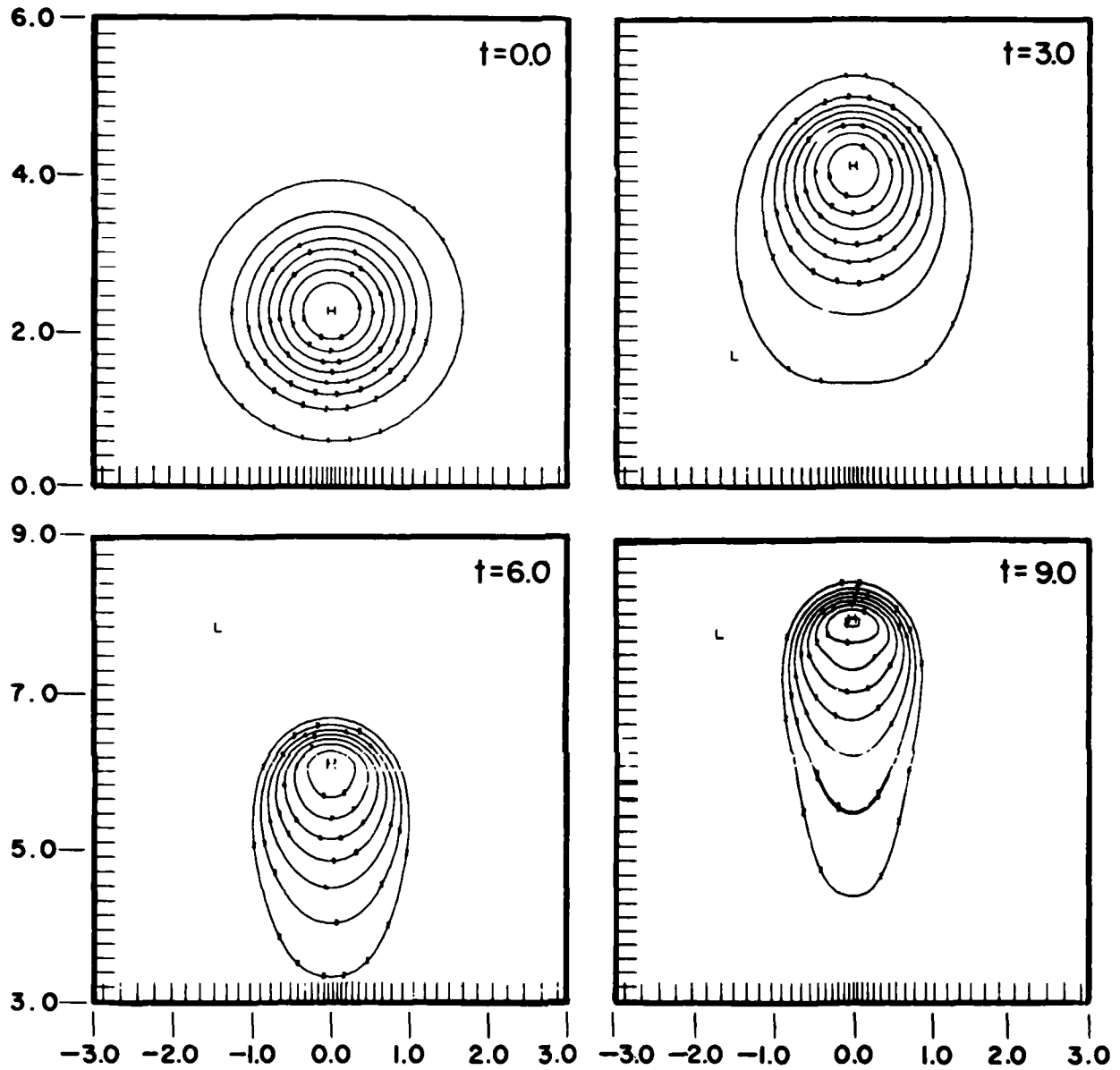
Figure 15. Isodensity contours for an initially circular plasma cloud with no initial perturbation showing backside steepening (taken from Ref. 12).
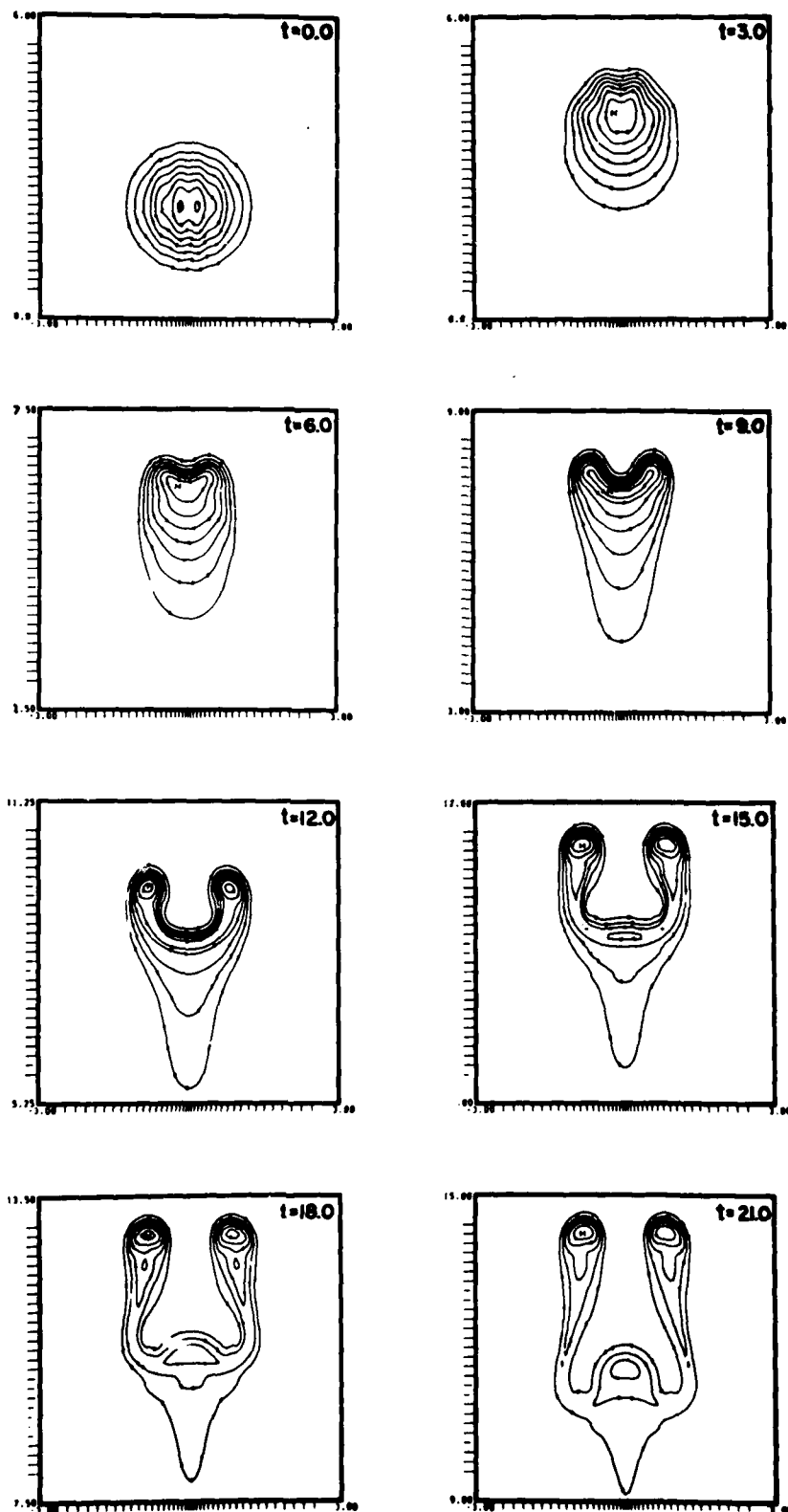
Figure 16. Isodensity contours for an initially circular plasma cloud with a 5% initial perturbation (taken from Ref. 12).

The process by which an initially cylindrically-symmetric plasma cloud breaks up into smaller-scale striations is not certain. One viewpoint suggests that after backside steepening has destroyed cylindrical symmetry, the cloud bifurcates, producing smaller-scale-size structures which then continue to evolve by a series of bifurcation processes. Another view tends to suggest that the backside steepening process produces a more one-dimensional-like cloud on the backside which becomes more unstable than an initially cylindrical cloud. This viewpoint would lead to the conclusion that this more one-dimensional-like cloud would break up into a series of sheets whose scale lengths are determined by processes that have not yet been clearly identified. There is no doubt that these sheets continue to evolve by a bifurcation (or budding or cleavage) process.

No numerical simulation of an initially cylindrically-symmetric cloud in a one-layer ionospheric model has spontaneously generated smaller scale structures by either developing a series of sheets or a bifurcation process. It is not known if the one-layer model would cause a cylindrical cloud to eventually bifurcate or striate. A recent study by Ossakow et al.[16] leads to the suggestion that the backside steepening of a cloud is perhaps the first stage in the beginning of a bifurcation. However, in the process of evolving, the steep backside becomes quasi-one-dimensional. It would appear that a number of sheets could form in this region, and their development could result in additional sheets being formed of smaller size. At late times, each of these sheets will have elongated in the direction of the neutral wind and will have the appearance of sheets with rod-like tips. This sheet-like appearance is similar to that seen in photographs of barium clouds taken at late times up the magnetic field line. Specific examples are the Spruce and Redwood ion clouds released during test series SECEDE and the Carolyn ion cloud released during the STRESS test series.

A numerical study by Doles et al.[17] suggests that interactions with other layers in the ionosphere can lead to the spontaneous formation of sheets without the need for initial large seed amplitudes. At the moment it is difficult to say what the dominant processes are that lead to the generation of nonlinear sheets in large plasma clouds in the ionosphere. Each of the mechanisms mentioned above may have some role to play. The identification of the role that each of those factors

plays will be necessary before one can specify with certainty the mechanism that determines the scale length of the nonlinear striations.

We have already alluded to the fact that the large scale striations, likely to exist at around 500 s following HANE, may have an appearance somewhat similar to those shown in the schematic diagram in Fig. 1(B). We expect each of these large-scale striations to continue to evolve in a manner very similar to ionospheric plasma clouds for two reasons. First, the typical ratio of the FLIP conductivity of the cloud to that of the background ionosphere is expected to be in the range from < 1 to 100 which overlaps the range of values of $\varkappa$ associated with many ionospheric barium releases. Second, by 500 s the regions of maximum conductivity are probably located in the range of from 200 to 400 kilometers away from the center of the burst so that the radial neutral wind tends to be flowing through each of the clumps of ionization in one direction similar to the wind flow through an ionospheric barium plasma cloud.

The equations (without diffusion) that describe the behavior of ionospheric plasma clouds do not contain any fundamental scale lengths, but do have the neutral slip velocity, V_s, as a fundamental velocity. The only lengths that enter the problem are those associated with the initial distribution of conductivity. According to Table 4.1, two such lengths associated with Gaussian distributions are the Gaussian radius a_o and the maximum gradient length h_m. It is not known what effect the assumed initial density profile has on the future development of such a cloud. However, all clouds with the same shape, density profile, and peak conductivity should evolve on a time scale that is proportional to a characteristic size, say, a_o. Thus, after striations have become fully-developed and the maximum in the conductivity has concentrated near the tip so it is somewhat rod-like, the tip of the striation should continue to evolve in a manner precisely similar to the manner in which the original cloud evolved, except on a time scale somewhat faster because of the smaller size. This concept leads to a rapid cascade producing larger numbers of striations of smaller and smaller size. Before continuing the discussion of the effect of size on the development time of striations, we first indicate the dependence of the development time on the shape of the cloud and the conductivity ratio $\varkappa$.

Even though we cannot specify precisely the method by which a large plasma cloud breaks up into smaller-scale striations, we can indicate the scaling of the time dependence on the shape of the cloud and its conductivity. In a frame moving with an appropriate field-line averaged neutral wind velocity, the zeroth-order equation for current continuity has the simple form

$$\nabla \cdot \Sigma(\vec{r}) \, \vec{E}\,' = 0 \qquad (4.15)$$

where $\vec{E}\,'$ is an effective electric field[13]. A plasma cloud represents an enhancement of the conductivity in a region where the neutral wind is blowing through background ionization. The gradients in the conductivity generate polarization electric fields that allow the cloud to move across the magnetic field lines with part of the velocity of the neutral wind. In general, the velocity of the plasma cloud can be written in the form

$$\vec{V}_c = \frac{\vec{E}_a \times \vec{B}}{B^2} + \eta \left[\vec{V}_n - \frac{\vec{E}_a \times \vec{B}}{B^2} \right] \qquad (4.16)$$

where the coupling parameter, η, is a function of $\varkappa$ and β, the FLIP conductivity ratio and length to width ratio, respectively, of the plasma cloud. The functional dependence of η on $\varkappa$ and β is most easily obtained by solving Eq. (4.15) where the electric field has the constant value $\vec{E}_a' = \vec{E}_a + \vec{V}_n \times \vec{B}$ far from the cloud.

The functional form of $\eta(\varkappa, \beta)$ depends on the density profile in the plasma cloud. A simple solution of Eq. (4.15) exists for plasma clouds having a uniform density and a sharp edge corresponding to $\alpha = 0$ for the shape defined in Section 2. When the plasma cloud boundary has an elliptical shape with major axis $a\beta^{\frac{1}{2}}$ in the direction of the neutral wind and minor axis $a\beta^{-\frac{1}{2}}$, the electric field, $\vec{E}_c'$, inside the plasma cloud has a constant value.

$$\vec{E}_c' = \frac{\vec{E}_a'}{1 + \dfrac{\beta \varkappa}{1 + \beta}} \qquad (4.17)$$

The cloud moves with the constant velocity $\vec{V}_c = \vec{V}_n + \vec{E}_c' \times B/B^2$. By making use of

68

the expression (4.17) and subsituting into Eq. (4.16), we derive the expression for the coupling constant

$$\eta\,(\varkappa,\,\beta)\;=\;\frac{\beta\,\varkappa}{1+\beta+\beta\,\varkappa}\,.\qquad\qquad(4.18)$$

We invoke the principle that the tendency to striate depends on the difference in velocity between a plasma cloud with a finite value of β and a sheet-like cloud which corresponds to a value of $\beta = \infty$. In particular, we claim that the time for an elliptically-shaped cloud to bifurcate, striate, or develop smaller scale striations is proportional to the time it takes a sheet-like configuration of ionization to move a characteristic distance in the direction of elongation of the cloud with respect to the cloud. We will call this time a bifurcation time, τ_b, and indicate that it is proportional to

$$\tau_b\;=\;C_1\,\frac{a}{V_c(\infty)-V_c(\beta)}\;=\;C_1\,\frac{a}{V_s}\left[\sqrt{\beta}\,(1+\frac{1}{\varkappa})\,(1+\beta+\beta\,\varkappa)\right].\quad(4.19)$$

Thus, the time to develop or bifurcate is proportional to the scale size of the striation and inversely proportional to the neutral wind velocity in the frame moving with the velocity of the ambient ionization. Table 4.2 presents numerical values of the term in brackets for representative values of $\varkappa$ and β. We see that large values of $\varkappa$ and β slow down the rate of development of plasma clouds or large striations.

Table 4.2. Coefficient of bifurcation time.

$\varkappa$	$\beta = 1$	3	10	$\beta \gg 10$
1	6	24	133	$\to 4\,\beta^{\frac{3}{2}}$
3	7	30	173	$\to 5.3\,\beta^{\frac{3}{2}}$
10	13	65	386	$\to 12.1\,\beta^{\frac{3}{2}}$
$\varkappa \gg 10$	$\to \varkappa$	$\to 5.2\,\varkappa$	$\to 32\,\varkappa$	$\to \varkappa\beta^{\frac{3}{2}}$

The zeroth-order one-layer model equations indicate that the rod-like tip of a striation should behave exactly as an original plasma cloud behaves, proceeding through the same stages of development. Thus one would expect that the backside of the tip of the striation would steepen and then it should bifurcate and/or generate a number of smaller scale sheets, each of which would undergo its own similar development. The time scale for these subsequent developments, being proportional to the scale size, a, of the cloud, would rapidly diminish and in a finite time all striations would become infinitely thin. The scaling indicated by Eq. (4.19) has been supported by observations of the time it takes for large barium plasma clouds to striate. The striation onset time for cylindrical clouds tended to vary with scale size, a, neutral slip velocity V_s, and conductivity ratio, x, according to Eq. (4.19) with $\beta = 1$ and $C_1 \sim 1.5$. For instance, in the case of the Spruce ion cloud with a characteristic radius 3 km, $V_s = 50$ m/s, and an estimated conductivity ratio $x \sim 3$-4, definite structure was seen in the ion cloud at around 11 minutes after release. In further support of the reduction in development time with scale size, by 22 minutes following the release of the cloud (two striation onset times), the striations were well-developed with many tens of striations having scale sizes in the hundreds of meters range. It is obvious that this subsequent development of the cloud after the initial formation of the smaller sizes proceeded much more rapidly than the development of the original cloud.

However, this simple description ceased to apply at later times for the smaller-scale striations. Many striations with a scale size of order $a \sim 200$ m were seen to maintain their identities for several hundreds of seconds. Furthermore, the STRESS test series has shown that many fine-scale striations with characteristic dimensions of order hundreds of meters can exist for as long as two hours following a release and thus were able to maintain their identities for many thousands of seconds without undergoing further development. It is apparent that at the small scale sizes, the zeroth-order equations are inadequate to describe the behavior of the rod-like striations. They apparently become stable against the formation of striations.

There are a number of factors that have not been included so far in the zeroth-order model that could be important for affecting the development of small-

70

scale striations. Prominent among these missing factors are connections to other regions of the ionosphere along the same magnetic field line, the proper treatment of diffusion coefficients, and possibly changes in the effective background ionospheric conductivity. The proper treatment of the mechanisms that control the behavior of late-time striations may also lead to a proper treatment of the factors that determines the initial scale size in larger plasma clouds.

5. BIFURCATION MODEL AND TIME-DEPENDENT
POWER-SPECTRAL-DENSITIES

5.1 BIFURCATION MODEL APPLIED TO HANE

In Section 5.2 below, we present the results of calculations that give the phase power-spectral-density as a function of time based on parameters associated with HANE and the concepts described in Section 4. In this section we introduce a methodology for describing the time-dependence of the number and scale size of striations that might be expected following a HANE. We emphasize that it is the methodology that is of importance rather than the explicit results produced. However, there are some features of the results shown in this and the next section that are likely to occur following HANE.

In Section 4.1 we presented a discussion that motivated us to postulate that around 500 s following burst there exist some number, M_o, of well-developed striations with scale sizes in the range of several kilometers to several tens of kilometers. In this section, we describe a model for determining the time-dependence of the number and scale size of these initial striations beyond the first 500 s following burst. The concept is simple. For any striation of scale-size a, there is a characteristic bifurcation time $\tau_b(a)$. After a time lapse of $\tau_b(a)$, we envision that a large striation will have bifurcated and that there will then be two striations having the same shape and peak electron density as their original parent striation. In order to conserve the number of electrons, the size of these daughter striations will be $a/\sqrt{2}$.

We now define a time-dependent distribution function of striation scale sizes, $M(a, t)$, such that the number of striations of scale size a within the range a to $a + da$ is $M(a, t)da$. If we label the initial size of the striation a' and the present size a, then the above description of the bifurcation process is consistent with

$$M(a, t)da = 2M(a', t - \tau_b(a')) da'.$$

73

Substituting $a' = \sqrt{2}\, a$, we find that the distribution function, $M(a, t)$ would obey the equation

$$M(a, t) = 2^{\frac{3}{2}} M(\sqrt{2}a, t - \tau_b(\sqrt{2}a)). \tag{5.1}$$

A specification of the function $\tau_b(a)$ is necessary in order to find a solution.

Equation (5.1) is consistent with the following description. A newly created striation of size a' exists for a time $\tau_b(a')$ and then instantaneously breaks into two striations each of size $a'/\sqrt{2}$. This description of the bifurcation process is obviously not physical. It is also difficult to treat analytically. Instead, we will develop another equation that is consistent in concept with the above bifurcation model but represents striations as changing continuously in size. We assume that a striation of size a after a time lapse t was earlier part of a larger striation of size a'. Then its present size is a function of the earlier size and the time lapse t, i.e., $a = a(a', t)$. A time constant $\tau(a)$ for the rate of change of size of striation of size a, can be defined by

$$\frac{1}{\tau(a)} = -\frac{1}{a} \left. \frac{\partial a(a', t)}{\partial t} \right|_{a'} \tag{5.2}$$

where we take $\tau(a)$ as being proportional to $\tau_b(a)$. This description says that each striation slowly shrinks continuously creating a fraction of a striation of the same shrinking size. This description is not physical either but it roughly satisfies Eq. (5.1), it is analytically tractable, and, for a continuous distribution of a large number of striations, should provide a good indication of the subsequent distribution of scale sizes after a number of bifurcations.

If all striations have the same density profile, then the density within a striation can be written $n(r) = n_0 f(r/a)$. In order that the bifurcation process conserves the number of electrons, we must have

$$n_0 M(a, t) \left[\int_0^\infty 2\pi r f(r/a)\, dr \right] da = n_0 M(a', 0) \left[\int_0^\infty 2\pi r f(r/a')\, dr \right] da'.$$

This equation determines $M(a, t)$ in terms of the initial distribution of scale sizes $M_0(a') = M(a', 0)$ as

$$M(a, t) = \frac{a'^2(a, t)}{a^2} \left. \frac{\partial a'(a, t)}{\partial a} \right|_t M_0(a'(a, t))$$

$$= \left(\frac{a'(a, t)}{a} \right)^3 \frac{\tau(a)}{\tau(a'(a, t))} M_0(a'(a, t)) . \tag{5.3}$$

The function $a'(a, t)$ is the inverse of the function $a(a', t)$ and represents the initial scale size of the striation that has a size a after a time lapse t.

Equation (5.3) is a general result for the time-dependent striation scale-size distribution function once the function $a'(a, t)$ (or equivalently, $a(a;t)$) is determined. In order to provide an explicit example we need to specify an appropriate bifurcation time constant. We choose to illustrate a simple example by considering only cylindrically-shaped rod-like striations which are characterized by $\alpha = 0$ and $\beta = 1$. Motivated by the discussion following Eq. (4.19), we choose

$$\tau_b(a) = \frac{10 a}{V_s} \left[1 + \frac{C a_s^2}{(a - a_s)^2} \right] . \tag{5.4}$$

The second term in square brackets represents an ad hoc stabilizing term for small scale sizes such that $\tau_b(a) \to \infty$ as $a \to a_s$. We shall arbitrarily choose the minimum scale size $a_s = 0.1$ km in the following calculations. For moderate values of the constant C, we find that for $a \sim 3$ km and $V_s \sim 50$ m/s, the bifurcation time given by Eq. (5.4) is ~ 10 min which is about the time that it took the Spruce ion cloud to develop its initial structure. At late time after many striations had formed in the Spruce ion cloud, we found that no striation with scale size <300 m was seen to bifurcate in times ~ 200 s. We choose $C = 16$ in order to be consistent with that fact.

75

A number of other functions for $\tau_b(a)$, ad hoc or physically motivated, can be examined. For instance, the stabilizing term could have the form

$$\tau_{b1}(a) = \frac{10a}{V_s}\left[1 + \frac{C_2 a_s}{(a-a_s)}\right].\qquad(5.5)$$

For comparison purposes, the two functions $\tau_b(a)$ and $\tau_{b1}(a)$ with $C = 16$ and $C_2 = 5$ are shown plotted in Fig. 17 with $V_s = 500$ m/s. Henceforth, we will adopt the time constant $\tau(a)$ associated with $\tau_b(a)$ solely because the striations do not accumulate at the smallest scale size a_s as rapidly as for $\tau_{b1}(a)$.

We take the time constant defined in Eq. (5.2) to have the same form as $\tau_b(a)$, i.e.,

$$\tau(a) = \tau_0 a\left[1 + \frac{C a_s^2}{(a-a_s)^2}\right].\qquad(5.6)$$

If we integrate Eq. (5.2) for a bifurcation time $\tau_b(a)$ and neglect the time-dependence of a on the left-hand side, we obtain by using Eqs. (5.4) and (5.6),

$$\frac{\tau_b(a)}{\tau(a)} = \frac{10}{\tau_0 V_s} = -\ln\frac{a/\sqrt{2}}{a} = \frac{1}{2}\ln 2 \qquad(5.7)$$

from which

$$\tau_0 = \frac{20}{V_s \ln 2}\; s \qquad(5.8)$$

with V_s expressed in km/s. As a characteristic value of the neutral slip velocity in the HANE late-time-frame, we take $V_s = 0.5$ km/s. Equation (5.8) then gives $\tau_0 = 58$ s as the value on which our numerical calculations below are based.

With $\tau(a)$ of the form given by Eq. (5.6), the time it takes for a striation of size a to be formed from a striation of size a' can be found by integrating Eq. (5.2);
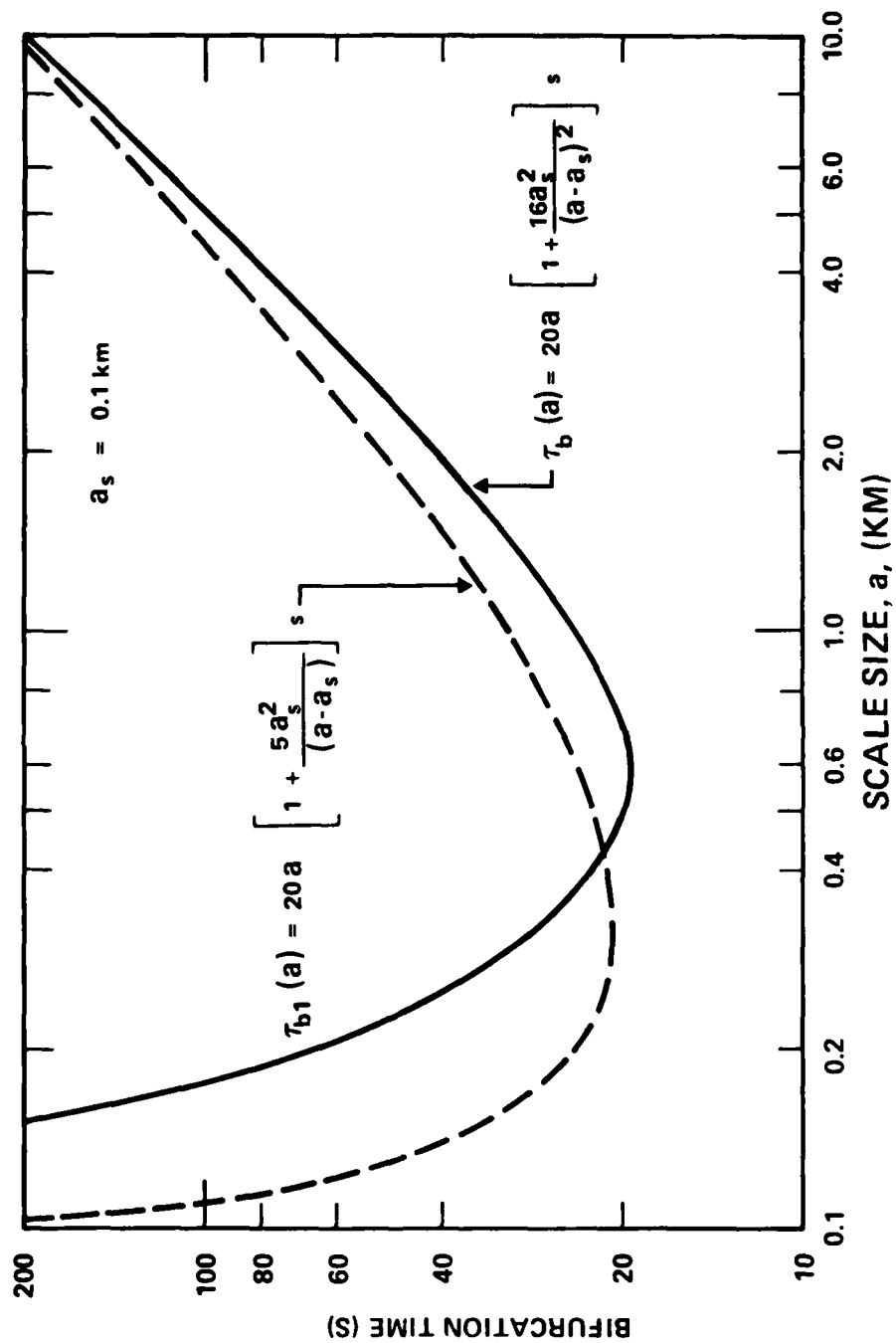
76

Figure 17. Bifurcation time as a function of striation scale size, a, for two models discussed in the text.

77

$$t(a, a') = -\int_{a'}^{a} \frac{\tau(a)}{a} \, da = \tau_0 \left[a' - a + Ca_s^2 \left(\frac{1}{a-a_s} - \frac{1}{a'-a_s} \right) \right] \qquad (5.9)$$

For initial scale sizes $a' > 10$ km, $C = 16$, and $a_s = 0.1$, the last term in Eq. (5.9) is less than one second in magnitude and we will neglect it. Henceforth we will measure time t in seconds after burst and will assume that at $t = t_0 = 500$ s there exist striations with some initial distribution in scale sizes. In terms of the normalized time lapse $\bar{t}$ given by

$$\bar{t} = t(a, a')/\tau_0 = \frac{t - 500}{58} . \qquad (5.10)$$

we may use Eq. (5.9) to explicitly approximate the functions $a'(a, t)$ and $a(a', t)$:

$$a' = a + \bar{t} - \frac{0.16}{a - 0.1} ; \qquad (5.11)$$

$$a = 0.05 + \frac{1}{2} \left[a' - \bar{t} + \sqrt{(a' - 0.1 - \bar{t})^2 + 0.64} \right] . \qquad (5.12)$$

In order to specify the striation scale-size distribution as a function of time, we need to specify the distribution of sizes at the initial time, t_0, and the time dependence of the number of new striations that are being generated at each scale size other than by the bifurcation process. The latter represents a time-dependent source of striations each of which would then evolve in scale size. We will illustrate the methodology by considering only the initial-value problem and neglecting an additional source of newly-created striations. However, the second initial distribution that we discuss below is motivated by the distribution of sizes that results from the specific choice of $\tau(a)$. The first example of an initial size distribution is a delta function, i.e., initially there are striations of only one size present. Based on the discussion in Section 4.1.1, we shall assume that at 500 s after burst there are M_0 striations of scale size 20 km. Thus $M_{01}(a') = M_0\delta(a' -20)$. By applying the general formula given in Eq. (5.3), we find

78

$$M_1(a, t) = M_0 \frac{a'^2}{a^2} \left. \frac{\partial a'}{\partial a} \right|_t \delta(a' - 20)$$

$$= \frac{400 M_0}{a_\ell^2(t)} \delta(a - a_\ell(t)) \tag{5.13}$$

where $a_\ell(t)$ is the solution of Eq. (5.12) with $a' = 20$. The second form for $M_1(a, t)$ indicates that at any time only one scale size is present and the number of striations varies as $1/a^2$. We note that the total number of electrons is conserved (time-independent) and, according to the equation leading to the derivation of Eq. (5.3), is proportional to $800 \, \pi \, M_0 n_0 \int_0^\infty x \, f(x) \, dx$.

The above model is consistent with the presumed instantaneous creation of a number of striations of a given size at 500 s. If, instead, striations were created continuously throughout the initial 500 s time interval, the striations into which they evolve would have a $1/a^2$ distribution. An initial $1/a^2$ distribution of large scale sizes tends to maintain itself. The $1/a^2$ behavior is a property of the choice of the form of $\tau(a)$. For intermediate values of a such that $a_s \ll a \ll a'$, we find from Eq. (5.11) that $a'(a, t) \sim \bar{t}$. By applying the general formula Eq. (5.3), we obtain

$$M(a, t) = \left(\frac{a'}{a}\right)^3 \frac{\tau(a)}{\tau(a')} M_0(a') \sim \frac{\bar{t}^2 M_0(t)}{a^2} \tag{5.14}$$

i.e., $M(a, t) \propto 1/a^2$ independent of the form of the initial distribution $M_0(a')$. A different choice of the function $\tau(a)$ gives a different distribution. For example, if $\tau(a) = \bar{\tau}$, a constant independent of a, then $M(a, t) \propto 1/a^3$.

For the second example we shall take an initial $1/a^2$ distribution. At 500 s after release we assume that there are a total of M_0 striations distributed in size between 10 and 40 kilometers with a $1/a^2$ distribution. Thus

$$M_{02}(a') = \frac{40 M_0}{3 a'^2} H(a' - 10) H(40 - a') \tag{5.15}$$

79

where H(x) is the Heaviside step-function. The numerical coefficient and end limits are chosen so that initially there are the same number of striations present as for $M_{01}(a')$, although they are now distributed in size, and they contain the same number of electrons. We note that although half of the striations present have scale sizes between 10 and 16 km, they contain only 20% of the electrons while half of the electrons are contained in 20% of the striations with sizes between 25 and 40 km.

Thus applying the general formula (Eq. (5.3)) we obtain the second time-dependent distribution of striation scale sizes,

$$M_2(a, t) = \frac{40M_o}{3a^2} \left[1 + \frac{0.16}{(a-0.1)^2} \right] H(a - a_m(t)) \, H(a_M(t) - a) \qquad (5.16)$$

where we have neglected $0.16/(a' - 0.1)^2$ compared to 1 for $a' > 10$ km. The functions $a_m(t)$ and $a_M(t)$ are the solutions of Eq. (5.12) with $a' = 10$ and 40, respectively. Note that $M_2(a, t)$ has a time-independent (but scale-size dependent) amplitude but has a nonzero value only in the finite time-dependent range $a_m(t) < a < a_M(t)$. Table 5.1 lists the values of $a_\ell(t)$, $a_m(t)$, $a_M(t)$, and the number of striations, $N_j(t) = \int_0^\infty M_j(a, t)\, da$, that are present according to the two model distributions at 500 s increments after burst.

Table 5.1   Bifurcation model parameters

t	a_ℓ	a_m	a_M	N_1	N_2
(s)	(km)	(km)	(km)	(M_o)	(N_o)
500	20	10	40	1	1
1000	11.39	1.49	31.38	3	9
1500	2.82	0.122	22.67	50	4,300
2000	0.127	0.110	14.15	24,000	13,000
∞	0.100	0.100	0.100	40,000	40,000

Figure 18 contains a plot of the amplitude of the two distributions in scale size defined by Eqs. (5.13) and (5.16) respectively. The solid curves give

80
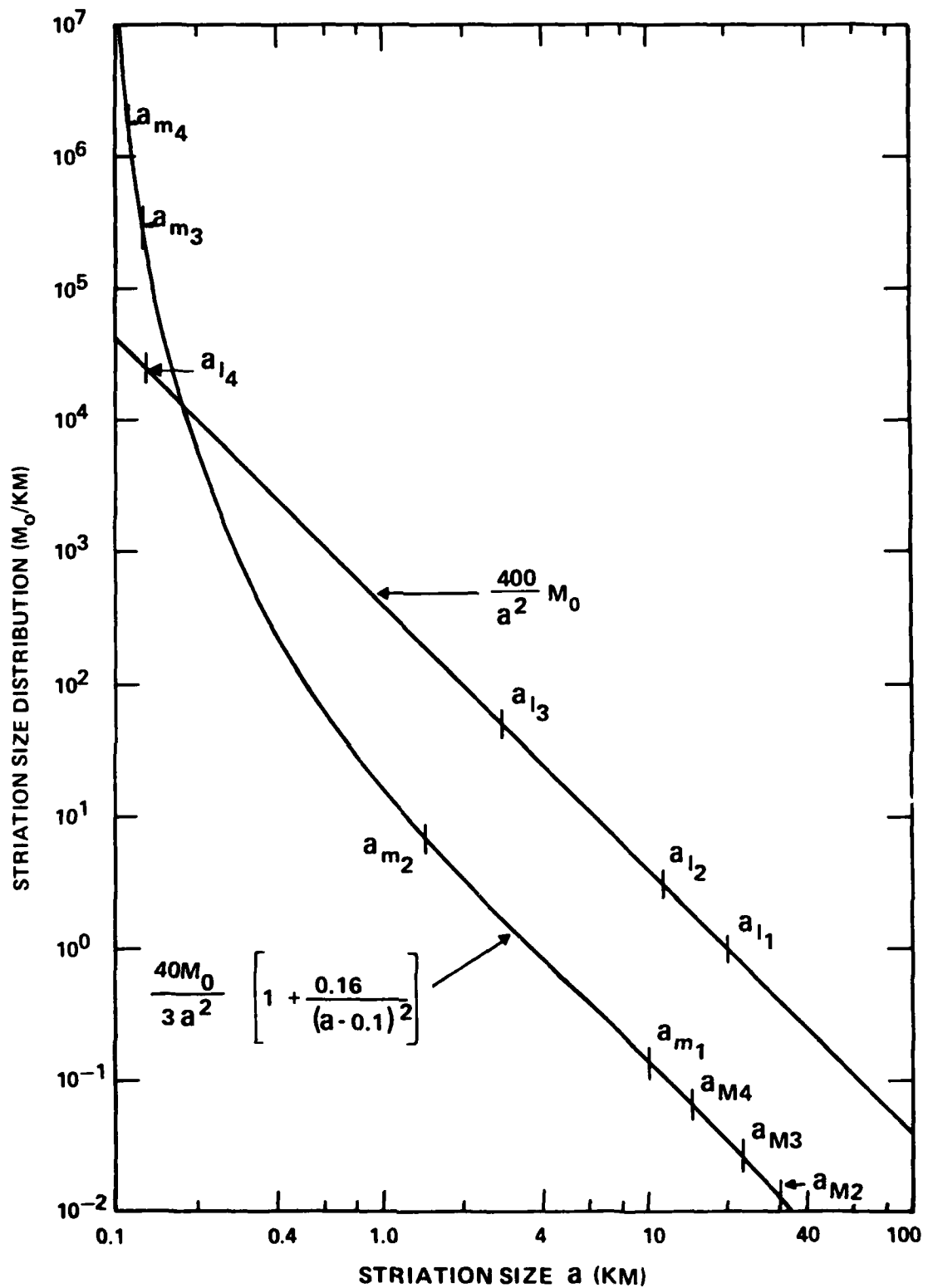
Figure 18. The two distributions in striation scale size resulting from the two assumed initial distributions corresponding to a delta function, $M_{o1}(a)$, and to a $1/a^2$ distribution, $M_{o2}(a)$, as discussed in the text. The values of a_m, a_M, and a_l as defined in the text are indicated at $t = 500$ s, 1000 s, 1500 s, and 2000 s after burst, respectively.

the number of striations of a given size. For $M_1(a, t)$, there is only one scale size at any time. The value of that scale size at times of 500, 1000, 1500 and 2000 s after burst are indicated by small vertical bars labeled $a_{\ell 1}$ through $a_{\ell 4}$, respectively. Likewise, at any given time in the evolution of the striations according to $M_2(a, t)$ there are always striations present between a minimum, a_m, and a maximum, a_M, scale size. The values of a_m and a_M at 500, 1000, 1500 and 2000 s after burst are also indicated by vertical bars. Figure 19 shows the total number of striations present according to the two models as a function of time after burst.

As the distribution $M_2(a, t)$ evolves, the ratio a_M/a_m at first increases and then decreases as can be seen from Table 5.1. At 2000 s after burst there are still large-scale striations with sizes greater than one kilometer present as well as many striations close to the minimum size a_s. After a few more hundred seconds $a_M \rightarrow a_s$ and the distribution approaches a delta function with all striations being of order 100 meters in size.

5.2   TIME-DEPENDENT PHASE POWER-SPECTRAL-DENSITIES

In Section 3 of this report it was emphasized that a knowledge of the phase power-spectral-density (PSD) is sufficient for determining the average properties of scintillation effects to be expected on propagating through striated media. In Section 2, the effects of peak electron concentration, scale size of striations, and shape and density profile of striations on the phase PSD produced by a single striation was calculated. In Section 4, the striation characteristics to be expected from HANE were discussed and in Section 5.1 we introduced a simplified bifurcation model that determined the number of striations of different scale sizes as a function of time. In this section we compare the phase PSDs that result from the two initial assumed distributions of scale sizes, $M_1(a, t)$ and $M_2(a, t)$. We will also show and discuss the changes in the PSD as the size distribution of striations changes as a function of time.

The results shown here should not be taken as a specific example of what actually occurs in HANE, but rather as a model calculation of the methodology that we have been describing. However, the physical characteristics that are
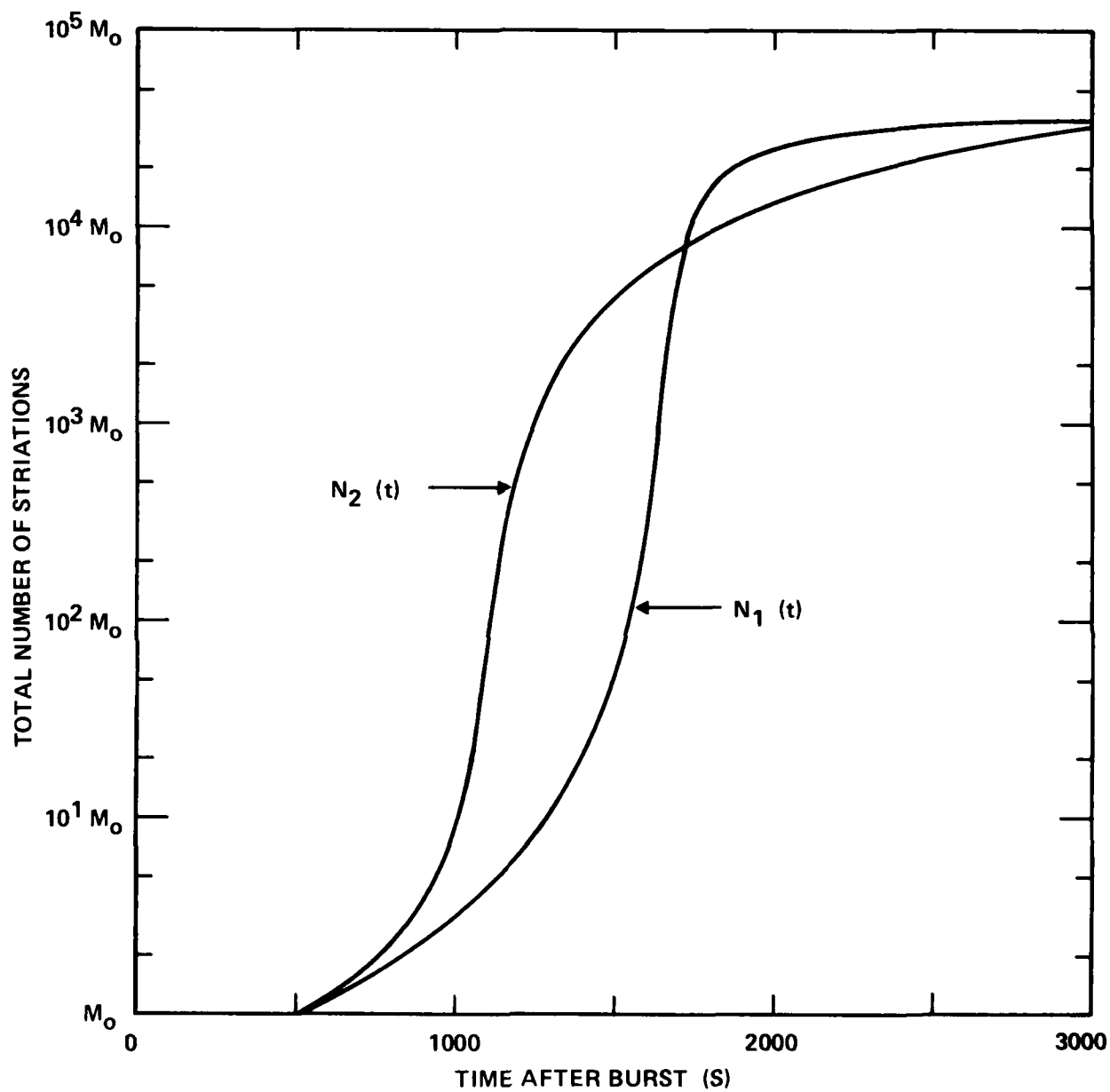
82

Figure 19. Total number of striations as a function of time resulting from the two striation scale size distributions as discussed in the text.

believed to operate on the striations during HANE will undoubtedly produce some of the effects that will be shown here. As we learn more detailed and precise information regarding the time development of striations in HANE, this same methodology can be applied to provide more accurate estimates of the time-dependent PSD.

The contribution to the phase PSD, $\varphi^2(q)$, due to a single rod ($\beta = 1$) of radius a is given by Eq. (3.1.1) with $\alpha = 0$. The PSD resulting from a set of rods, located randomly, having a distribution of scale sizes given by $M_j(a, t)$ is

$$\varphi_j^2 (q, t) = \overline{C} P_j (q, t) = \frac{2\pi}{L} \left(\frac{r_e \lambda n_0}{q} \right)^2 \int a^2 J_1^2 (qa) M_j (a, t) \, da \qquad (5.17)$$

where $P_j(q, t)$ are normalized PSD. By expanding the Bessel function for small q as $q \to 0$, we define the constant $\overline{C}$ to have the value

$$\overline{C} \approx \varphi_2^2 (0, 500) = 1.4 \times 10^5 \, \pi \, (r_e \lambda \, n_0)^2 \, M_0/L$$

$$= 3.5 \times 10^8 \, \frac{(n_0 \lambda)^2 \, M_0}{L} \, rad^2 \, km \qquad (5.18)$$

with $(n_0 \lambda)$ expressed in units of $10^{13} \, m^{-2}$ and L given in km. With this choice, we find $P_2 (0, 500) = 1$ and $P_1 (0, 500) = 4/7$. In Figures 20 and 21 we show the time-development of $P_1(q, t)$ and $P_2 (q, t)$, respectively, obtained by using the two different scale-size distribution functions $M_1(a, t)$ and $M_2(a, t)$ discussed in the previous section, i.e., those developing from an initial delta function and $1/a^2$ distribution, respectively. In Figures 22 through 25, we compare $P_1(q, t)$ with $P_2(q, t)$ at times corresponding to 500, 1000, 1500 and 2000 s after burst.

Figure 20 shows $P_1(q, t)$ at 5 different times including the asymptotic curve as $t \to \infty$. Because $P_1(q, t)$ is the PSD that results from a collection of 400 $M_0/a_\ell^2(t)$ striations of identical scale size a_ℓ, each of the curves shown is the same curve just displaced vertically and horizontally by the appropriate amount. The scales on the bottom show the appropriate wavenumber, q, and the equivalent wavelength, $2\pi/q$. The PSD as given by Eq. (3.1.1) has zeros
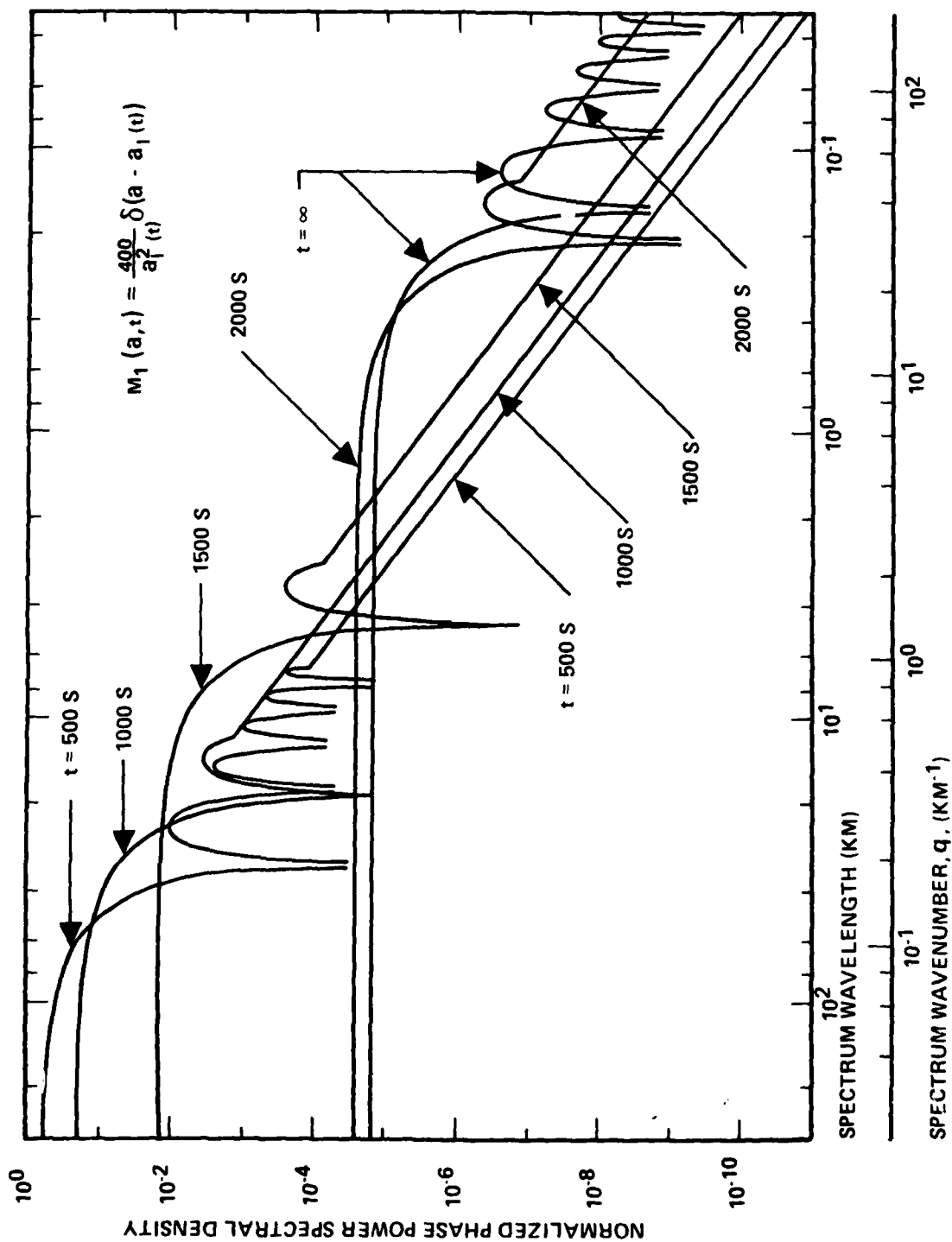
Figure 20. Time development of the Power-Spectral-Density corresponding to an initial delta function in scale size. The time is given in seconds after burst. The curve labeled 500 s results from the assumed initial single size of $a = a_\ell(500) - 20$ km.

at the zeros of the Bessel function. The first five zeros are indicated only for the initial, $t = 500$ s, and the final, $t \to \infty$, curves. For the other three intermediate times, only the first zero is indicated. The zeros are a manifestation of the existence of a single scale size. If there had been a slight range in scale sizes about the value a_ℓ, the zeros would have averaged out and the peaks would have been reduced in amplitude. The higher wavenumber portions of the PSD have been replaced by the straight line representing the q^{-3} asymptotic curve at the average values of the function. This straight line is located a factor of 2 below the peaks because the average value of $\sin^2$ is 0.5.

The values of $P_1(q, t)$ have simple expressions in the limits as $q \to 0$ and $q \to \infty$. By taking the appropriate power series expansion for small q and asymptotic expansion for large q of the Bessel function, we find that $P_1(q, t)$ can be represented fairly accurately by a function of the form

$$P_1(q, t) \sim \frac{4}{7} \frac{\left[a_\ell(t)/20 \right]^2}{\left[1 + 0.851 \, q^2 a_\ell^2(t) \right]^{\frac{3}{2}}} \, . \tag{5.19}$$

Because $P_1(0, t)$ decreases as $a_\ell^2(t)$, its value at $t \to \infty$ is a factor of 4×10^4 less than the initial value at $t = 500$ s. The phase PSD at very high wavenumber increases monotonically as $1/a_\ell(t)$ amounting to a late-time increase of a factor of 200 over the initial values of power at high wavenumber. From the expression in Eq. (5.19) one finds that the power at a given wavenumber, q, is a maximum at the time that $a_\ell(t) = 1.53/q$.

Figure 21 shows a similar plot of the phase PSD, $P_2(q, t)$, evaluated at the four times shown. This figure shows the time evolution of P_2 resulting from a group of striations which evolve in time by the bifurcation model discussed in the previous section, having an initial $1/a^2$ distribution in scale sizes ranging from a minimum of 10 km to a maximum of 40 km. The subsequent figures show a direct comparison between $P_1(q, t)$ and $P_2(q, t)$ at each of the respective times. The first observation is that the distribution in sizes has averaged out the zeros of the Bessel function and the slight ripple seen at the lower wavenumbers is a
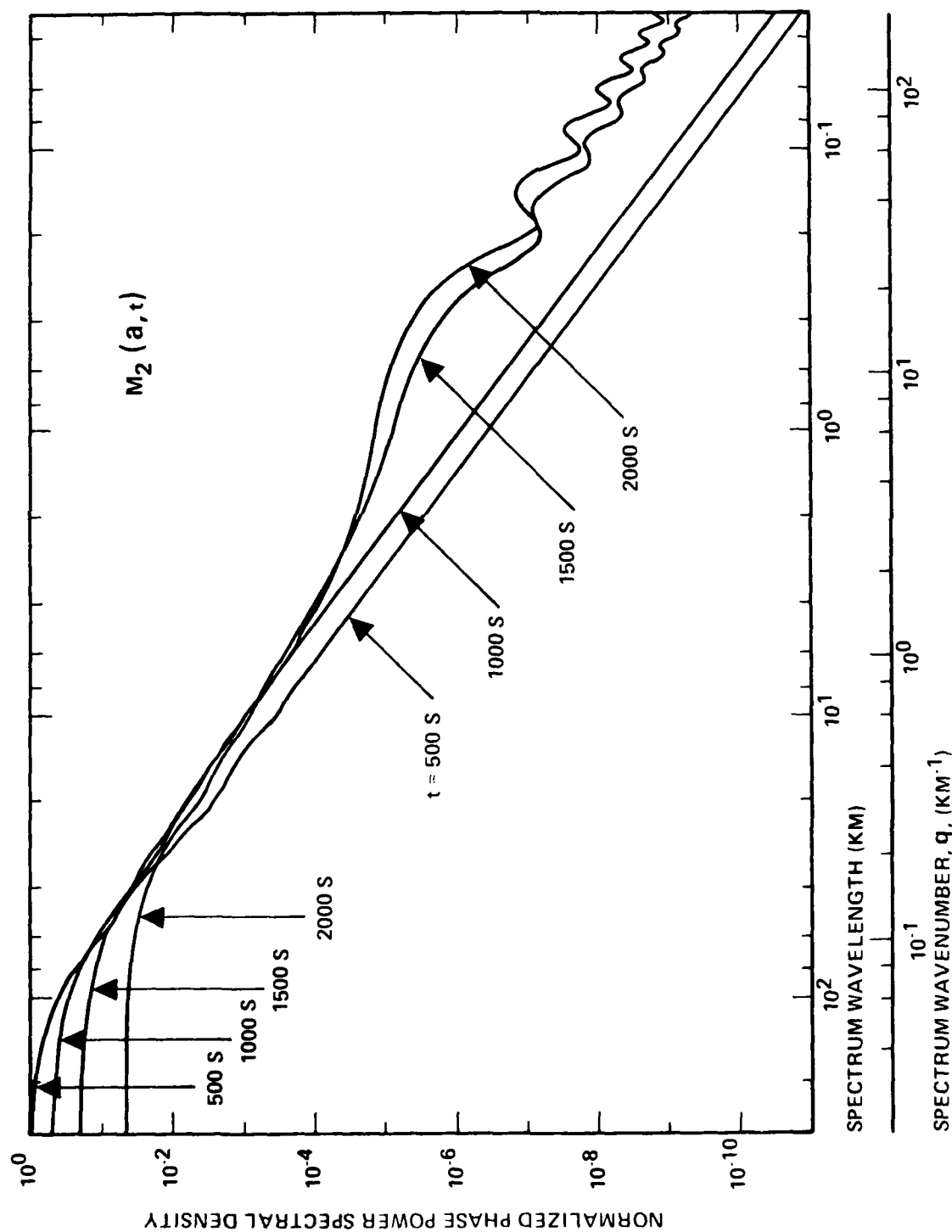
Figure 21. Time development of the Power-Spectral-Density corresponding to an initial $1/a^2$ distribution in scale size. The time is given in seconds after burst. The curve labeled 500 s results from the assumed initial distribution of scale sizes at 500 s following burst.

reflection of the shape of the size distribution. We note that the decrease in power at low wavenumbers with time is slower for $P_2(0, t)$ than for $P_1(0, t)$. This might seem surprising at first since $P_1(0, t)$ is initially proportional to $a_\ell^2(t)$ while the initial value of $P_2(0, t)$ is proportional to $a_M^3(t) - a_m^3(t)$. However, this initial small decrease is easily explained by realizing first that $a_m^3 \ll a_M^3$ and initially $a_M^3(t) \sim (40 - \bar{t})^3$ so that by $t = 2000$ s, $(\bar{t} = 25.9)$ it has decreased by only a factor of less than 25.

At times after 1000 s, $P_2(q, t)$ begins to take on an interesting character-istic. The accumulation of a large number of striations around a 100 meter scale size causes an enhancement in the PSD at the corresponding characteristic value of q. In addition, there are still a large number of electrons contained in striations that are bigger than many kilometers. Thus, it appears that the resultant spectrum is easily explained by the superposition of the contributions from the large number of electrons contained in the larger striations and the large number of striations at the minimum scale size.

Another consequence of the fact that a large number of striations are approaching the same size, approximately 100 m, is that the zeros of the Bessel function are beginning to manifest themselves again. Indeed, in the limit $t \to \infty$, $P_2(q, t)$ approaches $P_1(q, t)$ which is shown as the fifth curve in Figure 20. The most dramatic change that occurs in the phase PSD after 2000 s is the rapid decrease in power in the low wavenumbers.

Figures 22 - 25 compare the two phase PSDs from the two distributions at each of the four different times. Figure 22 is a comparison of the two phase PSDs resulting from the assumed initial distributions. Other than the presence of the zeros resulting from the choice of a single scale size only for M_1, it is apparent that these two PSD curves are comparable to each other to within a factor of 2. At 1000 s shown in Figure 23, the differences in the PSD have increased in some regions of q to approximately a factor of 4 but the differences betweem them are not great yet.

Also shown in Figure 23 is a naive application of the effect of diffusion shown by a dashed curve. If one introduces the effect of diffusion by adding a diffusion term to the continuity equation in the form given by Eq. (4.7), a

Figure 22. Comparison of the initial Power-Spectral-Densities at 500 s after burst resulting from the two assumed initial distributions in scale size.
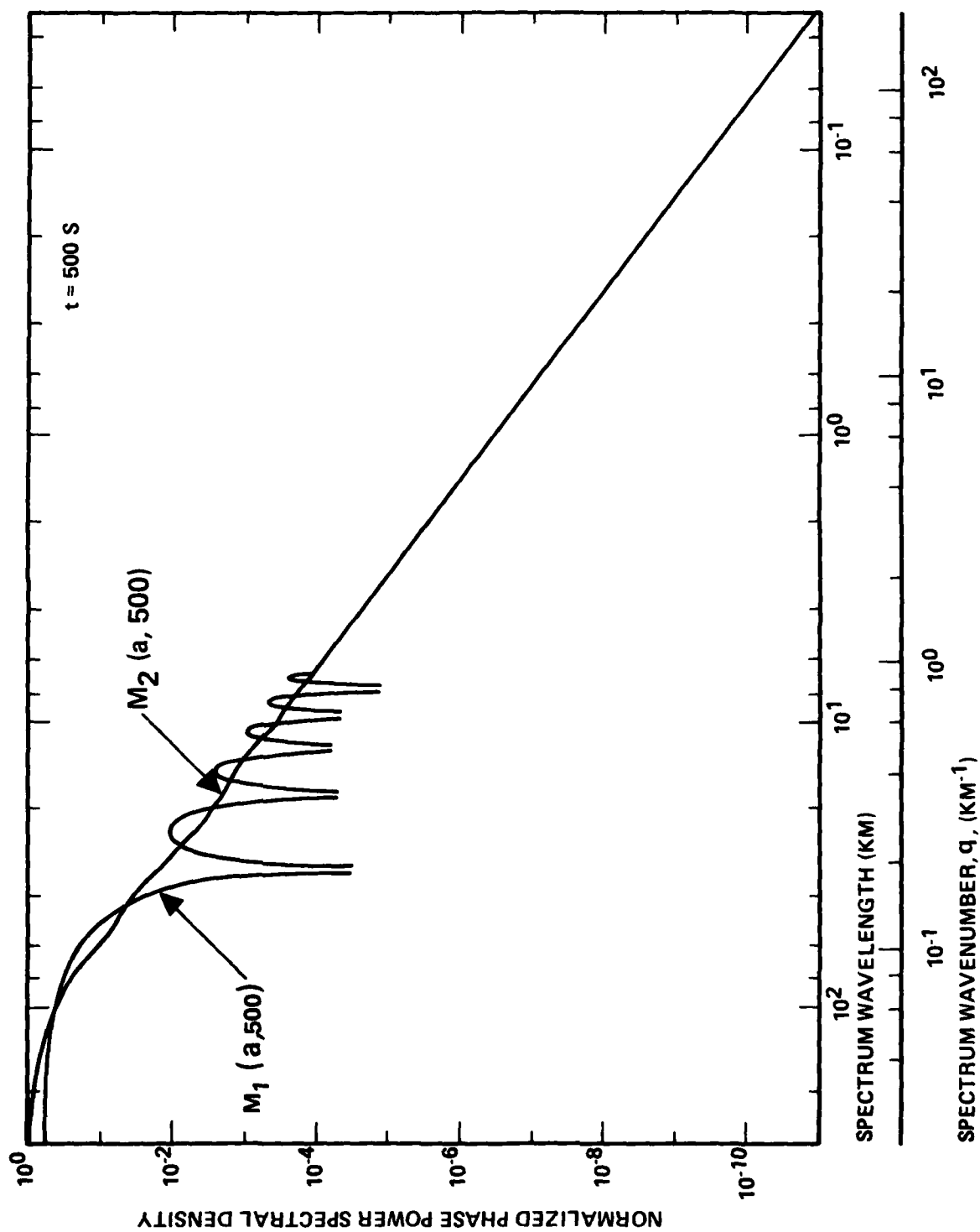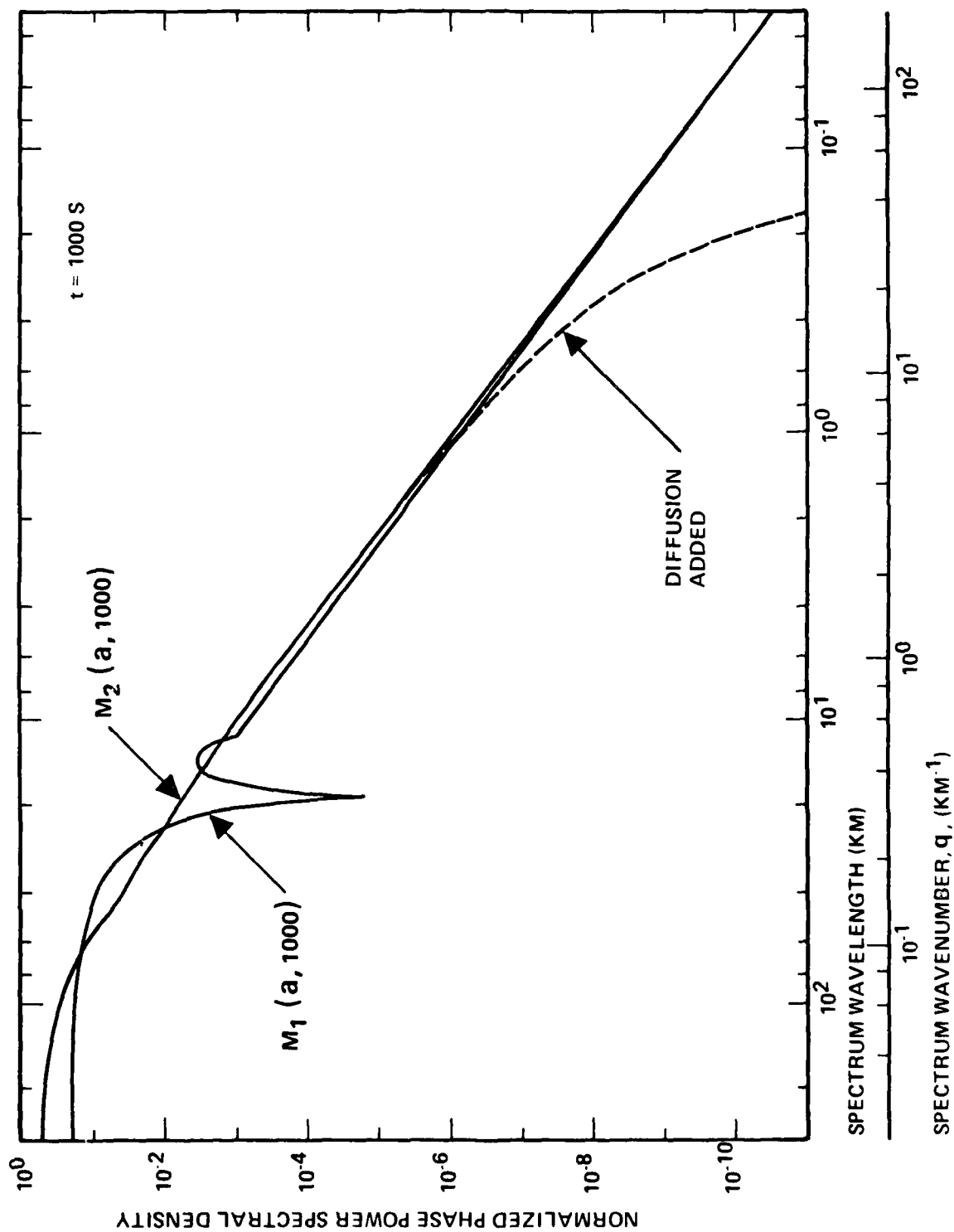
Figure 23. Comparison of the Power-Spectral-Densitites at 1000 s after burst resulting from the two assumed initial distributions in scale size. The effect of diffusion as shown is an over-estimate as discussed in the text and corresponds to a diffusion coefficient of 4 m^2/s.

linearized and nonlinear argument predict similar effects on the PSD. We take as a representative constant value $D = 4 \text{ m}^2/\text{s}$. If one linearizes the continuity equation with diffusion included, one finds that the amplitude of the fluctuation in density which initially may have a growth rate γ_0 now has an effective growth rate given by

$$\gamma = \gamma_0 - q^2 D \tag{5.20}$$

On the other hand, the time-dependent solution of the diffusion equation applied to an initial Gaussian rod of the form $n(r) = n_0 \exp(-r^2/a_0^2)$ results in

$$n(r, t) \sim \frac{n_0}{1 + 4 Dt/a_0^2} \exp\left(-\frac{r^2}{a_0^2 + 4 Dt}\right). \tag{5.21}$$

The Fourier transform of this function is

$$\hat{n}(q) = \frac{n_0}{1 + 4 Dt/a_0^2} \exp\left(-\frac{q^2 a_0^2}{4}\right) \exp(-q^2 Dt) \tag{5.22}$$

Hence, both the linearized and nonlinear analysis applied to the diffusion equation with a constant diffusion coefficient results in the fact that the amplitude of the Fourier component is time dependent and decreases in time as $\exp(-q^2 Dt)$. If this indeed were the effect on the amplitude of the Fourier components of the density distribution, the phase PSD would be modified by a factor $\exp(-2 q^2 Dt)$. The dashed line shown in Figures 23-25 is nothing more than an application of this factor to the undisturbed curves.

We emphasize that the purpose of including these dashed lines is to show solely what a naive application of diffusion to the PSD would produce. We do not feel that this is the correct method of showing the effect of diffusion on phase PSDs. The proper method of including diffusion is complicated because it needs to be applied to a time-evolving situation and the effect on the profile of striations needs to be evaluated. Part of the reason why this task is complicated is because

the value of diffusion at a particular altitude is affected by the electrodynamic coupling to other regions of ionization on the same magnetic field line. The effects shown by the dashed line grossly overestimate the effect that diffusion has on the phase PSD at high wavenumbers. Due to the presence of steepening processes, the effect of diffusion, properly applied, would be restricted to values of wavenumbers higher than the value $q_D \sim 10$ km^{-1} indicated in these figures. For example, the treatment of diffusion in Section 4.1.2 indicated lengths of the order 3 m (see Eq. (4.1.4)) which will affect only values of $q > 500$ km^{-1}.

Figure 24 shows that there are differences in the phase PSD produced by the two different scale-size distribution functions at 1500 s after burst that approach an order of magnitude difference in power for some values of q. The bifurcation process described in the previous subsection is an incompressible process. As such, the $\int r\, n_e^2(r)\, dr$ is conserved as the striations bifurcate and change their number and size. This fact implies that $\int \hat{n}_e^2(k_x, k_y)\, dk_x\, dk_y$ is conserved where $\hat{n}_e^2(k_x, k_y)$ is the PSD of the fluctuations in electron density. For an isotropic, homogeneous distribution of cylindrically-symmetric rods, the case that we have been considering, the phase PSD is given by $\phi^2(q) = \hat{n}_e^2(q, 0)$, $\hat{n}_e^2$ is a function of $k = (k_x^2 + k_y^2)^{\frac{1}{2}}$, and the conserved quantity in k-space is $\int k\hat{n}_e^2(k)\, dk$. Thus, the value of the $\int q P_j(q, t)\, dq$ for the two solid curves in Figure 24 is also conserved. While the value of this integral over all q is the same for both P_1 and P_2, the contribution to the integral from the middle range of q values is greater for P_1 than for P_2; P_2 has relatively larger contributions to its total value from low and high values of q. Note that $\int q P(q, t)\, dt$ is not, in general, conserved for asymmetric striations with $\beta > 1$.

Figure 25 shows that the $P_2(q, t)$ is approaching that of $P_1(q, t)$ as time approaches infinity. The large power at low values of q for P_2 at this time is just a reflection of the fact that almost half of the electrons still reside in striations of greater than 1 kilometer radius.

5.3   SUMMARY

The time-dependent PSD associated with a given set of striations is sufficient for determining propagation effects. The procedures for including the effects

Figure 24. Comparison of the Power-Spectral-Densities at 1500 s after burst resulting from the two assumed initial distributions in scale size. The effect of diffusion as shown is an over-estimate as discussed in the text and corresponds to a diffusion coefficient of 4 m²/s.
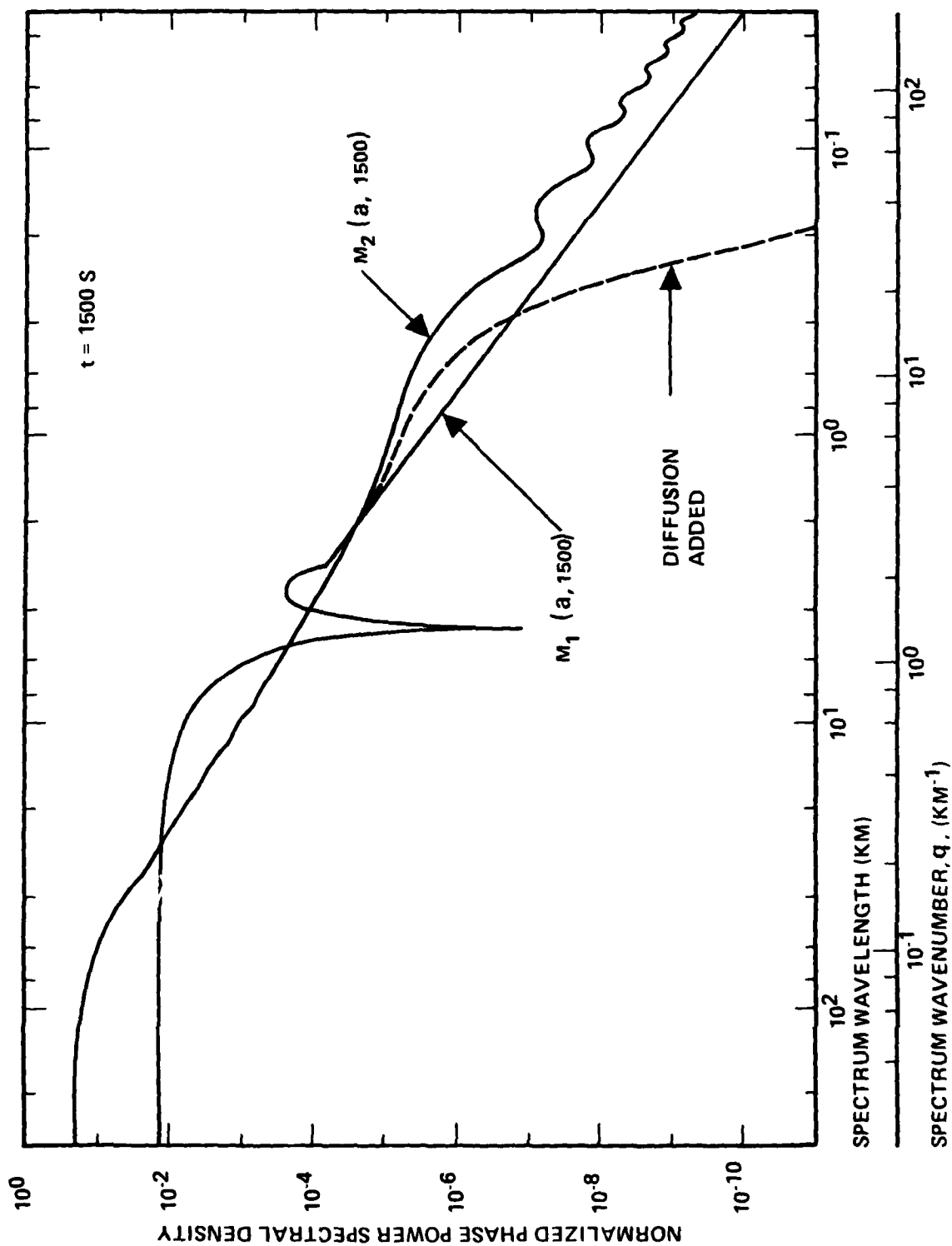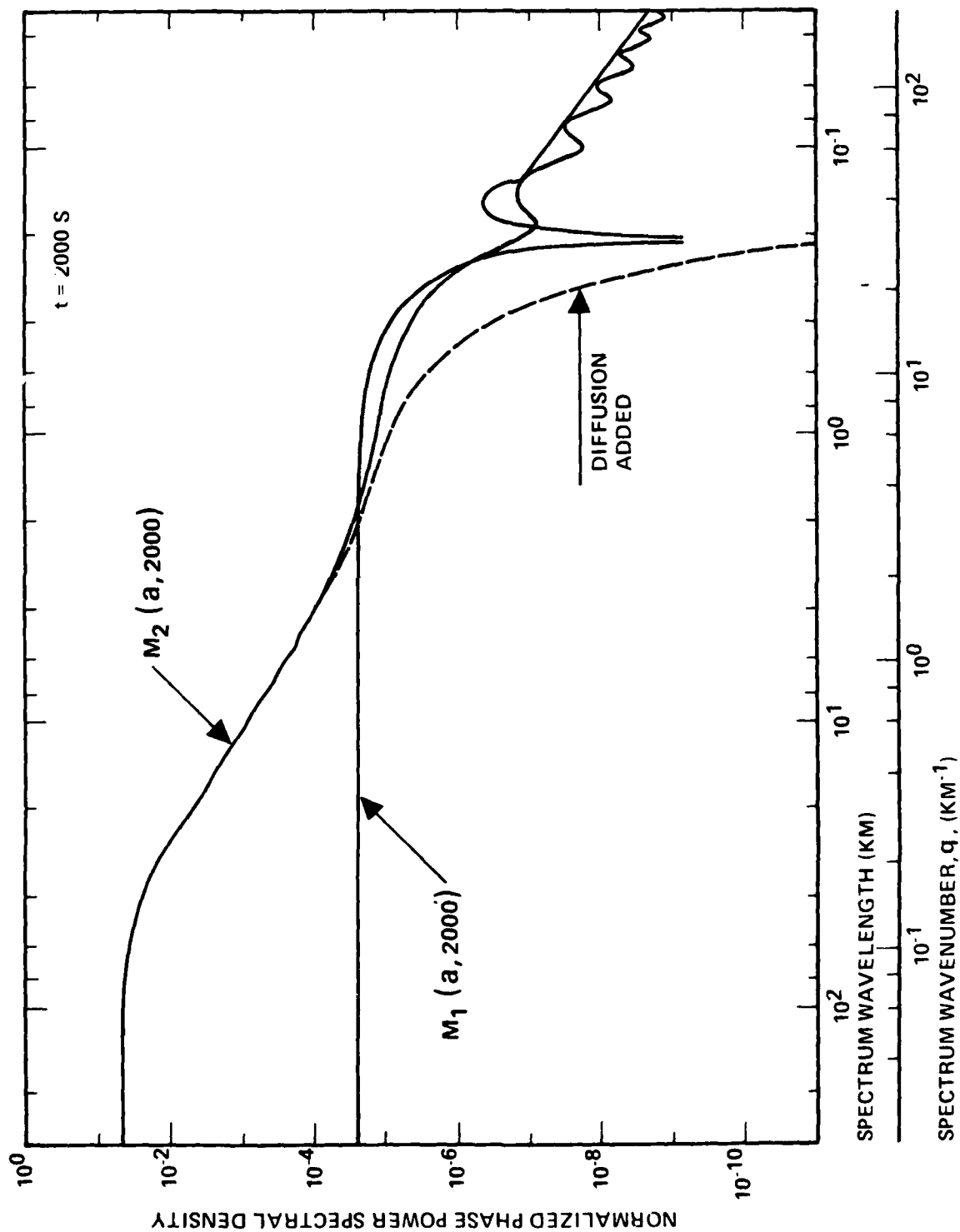
Figure 25.   Comparison of the Power-Spectral-Densities at 2000 s after burst resulting from the two assumed initial distributions in scale size.   The effect of diffusion as shown is an over-estimate as discussed in the text and corresponds to a diffusion coefficient of 4 m²/s.

of the shape of striations and the density profile within striations in determining the phase PSD have been incorporated and the results have been studied in terms of the profile and shape parameters α and β.

The weak link in the procedure for determining the propagation effects that result from HANE is in being able to specify accurately the characteristics of striations. Based on our currently available understanding of the processes which operate to create the structured ionization, we have presented a discussion of the range of expected striation scale sizes that can be expected to exist 500 s after a high altitude nuclear burst. Furthermore, we have discussed our current understanding of the time development of the striations.

A perhaps surprising result is that at late times, after 500 or 1000 s following burst, the region of enhanced ionization has broken up into individual large size striations whose field-line-integrated Pedersen (FLIP) conductivity is of the same order of magnitude as the FLIP conductivity created by the deployment of 48 kg barium releases. This similarity strongly suggests that the continued development of the striations in HANE beyond 500 s after burst will be similar to the development of striations in barium plasma clouds with appropriate adjustments in the time scale due to the different initial size and neutral slip velocity. As the striations break up into smaller scale sizes the time for them to continue to evolve, or bifurcate, continually decreases. On a time scale measured in several 500 s units, we reach the conclusion that most of the ionization will exist in striations of less than a kilometer in size. Observations of barium clouds suggest that there is a minimum size striation that is produced that does not subsequently striate. This size appears to be of order 100 meters but may be somewhat less. We do not presently have adequate understanding for determining this size.

Consistent with the above description, we have introduced a bifurcation model that contains some of the physical features operating to change the scale size of striations. We have accomplished this by introducing a model for the bifurcation time as a function of striation scale size. The specific model that we use is motivated by our physical understanding for large scale sizes but its dependence near the smallest scale size is purely ad hoc. However, it reproduces

95

the features of limiting the further bifurcation of the small size striations and appears to give times that are consistent with the observations of barium clouds for striations of around 300 m radius.

An effect of having an initial distribution in scale sizes is that the PSD does not maintain a simple shape as the striations evolve. The methodology that we have described allows us to introduce appropriate modifications as our understanding increases. Once we are more certain of the initial distribution in scale sizes, the values of the parameters α and β as a function of time, and the mechanism that limits the smaller scale sizes, this knowledge can be incorporated into the procedures that we have discussed.

Based on an initial exploration of the appropriate value ranges of the parameters, we summarize the propagation effects in HANE. The ellipticity of the striations reduce the scintillation effects over most of a striated region and enhance the effects in the central region. Striations with high central electron density compared to background have predominantly parabolic profiles which reduces the scintillation effects to that of abrupt profiles with lower electron densities closer to the background in most cases. High frequencies, $\lambda \leq 3$ cm, may have negligible scintillation many minutes after burst. Lower frequencies may have Rayleigh scintillation for hours after burst.

In conclusion, the areas in which additional work is needed are: an understanding of the physics that determines the initial distribution of scale sizes in a cylindrical geometry; a more accurate understanding of the time-development of the striations in the nonlinear phase; the mechanisms that lead to the cessation of the bifurcation process, and the influence that the steepening and diffusion processes have on determining the density profile of the striations. This latter investigation is important for determining the wavenumbers at which the PSD decreases drastically.

REFERENCES

1. Sachs, D. L., "Propagation Effects of Steep Striations, DNA 4170T, November 1976.

2. Rino, C. L., "Analysis of Scintillation Effects on Communication Systems," Stanford Research Institute (unpublished).

3. Wittwer, L. A., "The Propagation of Satellite Signals through Turbulent Media," AFWL-TR-77-183, Air Force Weapons Laboratory, Kirtland AFB, NM, January 1978.

4. Knepp. D. L., "Multiple Phase-Screen Propagation Analysis for Defense Satellite Communications System," DNA 4424T, September 1977.

5. Linson, L. M., and J. B. Workman, "Formation of Striations in Ionospheric Plasma Clouds," J. Geophy. Res., 75, 3211, 1970.

6. McDonald, B. E., S. L. Ossakow, S. T. Zalesak, and N. J. Zabusky, "Determination of Minimum Scale Size in Plasma Cloud Striations," to be published in Proceedings of the 2nd Symposium on the Effect of the Ionosphere on Space Systems and Communications, Naval Research Laboratory, Jan 24-26, 1978.

7. Scannapieco, A. J., S. L. Ossakow, S. R. Goldman, and J. M. Pierre, "Plasma Cloud Late Time Striation Spectra," J. Geophy. Res., 81, 6037, 1976.

8. Salpeter, E. E., Ap. J., 147, 433, 1967.

9. Mercier, R. P., Proc. Roy. Sol., A58, 382, 1962.

10. Jokipii, J. R., Ap. J., 161, 1147, 1970.

11. Perkins. F. W., N. J. Zabusky, and J. H. Doles III, "Deformation and Striation of Plasma Clouds in the Ionosphere, 1," J. Geophys. Res. 78, 697, 1975.

12. Zabusky, N. J., J. H. Doles III, and F. W. Perkins, "Deformation and Striation of Plasma Clouds, 2, Numerical Simulation of a Nonlinear Two Dimensional Model, J. Geophys. Res., 78, 711, 1973.

13. Linson, L. M., and D. C. Baxter, "Ion Cloud Modeling," DNA 4455F, November 1977.

14. Linson, L. J., "Effect of Conjugate Ionosphere and Shape on the Motion of Barium Ion Clouds," Trans., Am. Geophys. Union, 52, 880, 1971.

15. Linson, L. M., "Nonlinear Dynamics of Barium Ion Clouds," in Analysis of Barium Clouds," RADC-TR-71-253, Vol. I, pp. 39-71, AVCO Everett Research Laboratory, Everett, Mass. 02149, June 1971.

16. Ossakow, S. L., S. T. Zalesak, and N. J. Zabusky, "Recent Results on Cleavage, Bifurcation, and Cascade Mechanisms in Ionospheric Plasma Clouds," NRL Memorandum Report 3579, August 1977.

17. Doles, J. H. III, N. J. Zabusky, and F. W. Perkins, "Deformation and Striation of Plasma Clouds in the Ionosphere, 3, Numerical Simulations of a Multilevel Model with Recombination Chemistry," J. Geophy. Res, 81, 5987, 1976.

DISTRIBUTION LIST

DEPARTMENT OF DEFENSE

Assistant Secretary of Defense
Comm, Cmd, Cont. & Intell.
    ATTN: M. Epstein
    ATTN: J. Babcock

Assistant to the Secretary of Defense
Atomic Energy
    ATTN: Executive Assistant

Command & Control Technical Center
Department of Defense
    ATTN: C-312, R. Mason
    ATTN: C-650, G. Jones
    ATTN: C-650, W. Heidig

Defense Advanced Rsch. Proj. Agency
    ATTN: TIO

Defense Communication Engineer Center
    ATTN: Code 720, J. Worhtington
    ATTN: Code R410, J. McLean

Defense Communications Agency
    ATTN: Code 810, J. Barna
    ATTN: Code 480
    ATTN: Code 101B
    ATTN: Code R1033, M. Raffensperger

Defense Documentation Center
12 cy ATTN: DD

Defense Intelligence Agency
    ATTN: DC-7D, W. Wittig
    ATTN: DB-4C, E. O'Farrell
    ATTN: HQ-TR, J. Stewart
    ATTN: DB, A. Wise
    ATTN: DT-5
    ATTN: DT-1BZ, R. Morton
    ATTN: DT-1B

Defense Nuclear Agency
    ATTN: DDST
    ATTN: STVL
3 cy ATTN: RAAE
4 cy ATTN: TITL

Field Command,
Defense Nuclear Agency
    ATTN: FCPR

Interservice Nuclear Weapons School
    ATTN: TTV

Joint Chiefs of Staff
    ATTN: J-3, WWMCCS Evaluation Office

Joint Strat. Tgt. Planning Staff
    ATTN: JPST, G. Goetz
    ATTN: JLTW-2

DEPARTMENT OF DEFENSE (Continued)

Livermore Division, Field Command, DNA
Lawrence Livermore Laboratory
    ATTN: FCPRL

National Security Agency
Department of Defense
    ATTN: R52, J. Skillman
    ATTN: B3, F. Leonard
    ATTN: W32, O. Bartlett

Under Secretary of Defense for Rsch. & Engrg.
    ATTN: Strategic & Space Systems (OS)

WWMCCS System Engineering Org.
    ATTN: R. Crawford

DEPARTMENT OF THE ARMY

Atmospheric Sciences Laboratory
U.S. Army Research & Development Command
    ATTN: DELAS-AE-M, F. Niles

ERADCOM Technical Support Activity
Department of the Army
    ATTN: DELET-ER, H. Bomke

Harry Diamond Laboratories
Department of the Army
    ATTN: DELHD-N-NP
    ATTN: DELHD-N-RB, R. Williams
    ATTN: DELHD-N-TI, M. Weiner

U.S. Army Ballistic Research Labs.
    ATTN: Tech. Library,

U. S. Army Comm-Elec. Engrg. Instal. Agency
    ATTN: CCC-EMEO,

U.S. Army Foreign Science & Tech. Center
    ATTN: DRXST-SD

U.S. Army Materiel Dev. & Readiness Command
    ATTN: DRCLDC, J. Bender

U.S. Army Nuclear & Chemical Agency
    ATTN: Library

U.S. Army Satellite Comm. Agency
    ATTN: Document Control

U.S. Army TRADOC Systems Analysis Activity
    ATTN: ATAA-PL
    ATTN: ATAA-TCC, F. Payan, Jr.
    ATTN: ATAA-TDC, J. Hesse

DEPARTMENT OF THE NAVY

Naval Electronic Systems Command
    ATTN: NAVELEX 3101, T. Hughes
    ATTN: PME 117
    ATTN: Code 5011
    ATTN: PME 117-T

DEPARTMENT OF THE NAVY (Continued)

Naval Intelligence Support Center
    ATTN: NISC-50

Naval Ocean Systems Center
    ATTN: Code 8151, C. Baggett
3 cy ATTN: Code 5324, W. Moler

Naval Research Laboratory
    ATTN: Code 7580
    ATTN: Code 7555
    ATTN: Code 6700, T. Coffey
    ATTN: Code 6707, J. Davis
    ATTN: Code 7500, Hg. Comm. Dir., B. Wald
    ATTN: Code 6701, J. Brown

Naval Space Surveillance System
    ATTN: J. Burton

Naval Surface Weapons Center
    ATTN: Code F14, R. Butler

Office of Naval Research
    ATTN: Code 420
    ATTN: Code 421

Office of the Chief of Naval Operations
    ATTN: Op-604
    ATTN: Op-941

Strategic Systems Project Office
Department of the Navy
    ATTN: NSSP-2722, F. Wimberly
    ATTN: NSP-2141

Naval Surface Weapons Center
White Oak Laboratory
    ATTN: Code F31

DEPARTMENT OF THE AIR FORCE

Aerospace Defense Command/DC
Department of the Air Force
    ATTN: DC, Mr. Long

Aerospace Defense Command/XPD
Department of the Air Force
    ATTN: XPDQ
    ATTN: XP

Air Force Avionics Laboratory
    ATTN: AAD, W. Hunt
    ATTN: AAD, A. Johnson

Air Force Geophysics Laboratory
    ATTN: LKB, K. Champion
    ATTN: OPR1, J. Ulwick
    ATTN: PHP, J. Aarons
    ATTN: PHI, J. Buchau
    ATTN: PHD, J. Mullen
    ATTN: OPR, A. Stair

Air Force Weapons Laboratory
    ATTN: DYC, J. Barry
    ATTN: SUL
    ATTN: DYC, J. Kamm

Deputy Chief of Staff
Research, Development, & Acq.
Department of the Air Force
    ATTN: AFRDQ

DEPARTMENT OF THE AIR FORCE (Continued)

Electronic Systems Division, AFSC
    ATTN: DCKC, J. Clark
    ATTN: XRW, J. Deas
    ATTN: YSEA

Foreign Technology Division, AFSC
    ATTN: TQTD, B. Ballard
    ATTN: NIIS, Library

Rome Air Development Center, AFSC
    ATTN: V. Coyne, OCSE
    ATTN: Documents Library/TSLD

Rome Air Development Center, AFSC
    ATTN: EEP

Space & Missile Systems Organization/MN
Air Force Systems Command
    ATTN: MNNL, S. Kennedy

Space & Missile Systems Organization/SK
Air Force Systems Command
    ATTN: SKA, M. Clavin

Strategic Air Command/XPFS
Department of the Air Force
    ATTN: NRT
    ATTN: DCX, Chief Scientist

DEPARTMENT OF ENERGY

Department of Energy
Albuquerque Operations Office
    ATTN: Doc. Con. for D. Sherwood

Department of Energy
Library Room G-042
    ATTN: Doc. Con. for A. Labowitz

Office of Military Application
Department of Energy
    ATTN: Doc. Con. for D. Gale

OTHER GOVERNMENT AGENCIES

Central Intelligence Agency
    ATTN: RD/SI, Rm. 5G48, Hq. Bldg.
            for OSI/PSTD

Department of Commerce
National Bureau of Standards
    ATTN: Sec. Officer for R. Moore

Department of Transportation
Office of the Secretary
    ATTN: R. Lewis
    ATTN: R. Doherty

Institute for Telecommunications Sciences
National Telecommunications & Info. Admin.
    ATTN: L. Berry
    ATTN: A. Jean
    ATTN: W. Utlaut
    ATTN: D. Crombie

National Oceanic & Atmospheric Admin.
Environmental Research Laboratories
Department of Commerce
    ATTN: Aeronomy Lab., G. Reid
    ATTN: R. Grubb

DEPARTMENT OF DEFENSE CONTRACTORS

Aerospace Corp.
    ATTN: F. Morse
    ATTN: N. Stockwell
    ATTN: I. Garfunkel
    ATTN: D. Olsen
    ATTN: S. Bower
    ATTN: J. Carter
    ATTN: T. Salmi
    ATTN: R. Slaughter
    ATTN: V. Josephson

Analytical Systems Engineering Corp.
    ATTN: Radio Sciences

Berkeley Research Associates, Inc.
    ATTN: J. Workman

Boeing Co.
    ATTN: J. Kenney
    ATTN: G. Keister
    ATTN: D. Murray
    ATTN: G. Hall
    ATTN: S. Tashird

Brown Engineering Company, Inc.
    ATTN: R. Deliberis

University of California at San Diego
    ATTN: H. Booker

Charles Stark Draper Lab., Inc.
    ATTN: D. Cox
    ATTN: J. Gilmore

Computer Sciences Corp.
    ATTN: H. Blank

Comsat Labs.
    ATTN: G. Hyde
    ATTN: R. Taur

Cornell University
Department of Electrical Engineering
    ATTN: D. Farley, Jr.

Electrospace Systems, Inc.
    ATTN: H. Logston

ESL, Inc.
    ATTN: C. Prettie
    ATTN: J. Roberts
    ATTN: J. Marshall

Ford Aerospace & Communications Corp.
    ATTN: J. Mattingley

General Electric Co.
Space Division
    ATTN: M. Bortner

General Electric Co.
    ATTN: F. Reibert

DEPARTMENT OF DEFENSE CONTRACTORS (Continued)

General Electric Company-TEMPO
Center for Advanced Studies
    ATTN: W. Knapp
    ATTN: M. Stanton
    ATTN: B. Gambill
    ATTN: T. Stevens
    ATTN: D. Chandler
    ATTN: DASIAC

General Electric Tech. Services Co., Inc.
HMES
    ATTN: G. Millman

General Research Corp.
Santa Barbara Division
    ATTN: J. Ise, Jr.
    ATTN: J. Garbarino

Geophysical Institute
University of Alaska
    ATTN: N. Brown
    ATTN: T. Davis
    ATTN: Technical Library

GTE Sylvania, Inc.
Electronics Systems Grp.-Eastern Div.
    ATTN: M. Cross

HSS, Inc.
    ATTN: D. Hansen

University of Illinois
    ATTN: K. Yeh

Institute for Defense Analyses
    ATTN: E. Bauer
    ATTN: J. Aein
    ATTN: J. Bengston
    ATTN: H. Wolfhard

International Tel. & Telegraph Corp.
    ATTN: Technical Library

JAYCOR
    ATTN: S. Goldman

Johns Hopkins University
Applied Physics Lab.
    ATTN: T. Potemra
    ATTN: Document Librarian

Kaman Sciences Corp.
    ATTN: T. Meagher

Lawrence Livermore Laboratory
University of California
    ATTN: Doc. Con. for Technical Information
        Dept. Library

Linkabit Corp.
    ATTN: I. Jacobs

Lockheed Missiles & Space Co., Inc.
    ATTN: Dept. 60-12
    ATTN: D. Churchill

Lockheed Missiles and Space Co., Inc.
    ATTN: R. Johnson
    ATTN: M. Walt
    ATTN: W. Imhof

Los Alamos Scientific Laboratory
    ATTN: Doc. Con. for D. Westervelt
    ATTN: Doc. Con. for R. Taschek
    ATTN: P. Keaton

M.I.T. Lincoln Lab.
    ATTN: D. Towle
    ATTN: L. Loughlin
    ATTN: D. Clark
    ATTN: P. Waldron

McDonnell Douglas Corp.
    ATTN: N. Harris
    ATTN: G. Mroz
    ATTN: J. Moule
    ATTN: W. Olson

Mission Research Corp.
    ATTN: R. Hendrick
    ATTN: S. Gutsche
    ATTN: F. Fajen
    ATTN: D. Sowle
    ATTN: R. Bogusch
    ATTN: P. Fischer
    ATTN: M. Scheibe

Mitre Corp.
    ATTN: C. Callahan
    ATTN: G. Harding

Mitre Corp.
    ATTN: W. Foster
    ATTN: M. Horrocks
    ATTN: W. Hall

Pacific-Sierra Research Corp.
    ATTN: E. Field, Jr.

Pennsylvania State University
Ionosphere Research Lab.
    ATTN: Ionospheric Research Lab.

Photometrics, Inc.
    ATTN: I. Kofsky

Physical Dynamics, Inc.
    ATTN: A. Thompson

Physical Dynamics, Inc.
    ATTN: E. Fremouw

R & D Associates
    ATTN: R. Lelevier
    ATTN: C. Gabbard
    ATTN: R. Turco
    ATTN: F. Gilmore
    ATTN: H. Ory
    ATTN: W. Karzas
    ATTN: W. Wright, Jr.
    ATTN: C. MacDonald

Rand Corp.
    ATTN: E. Bedrozian
    ATTN: C. Crain

Riverside Research Institute
    ATTN: V. Trapani

Sandia Laboratories
Livermore Laboratory
    ATTN: Doc. Con. for T. Cook
    ATTN: Doc. Con. for B. Murphey

Sandia Laboratories
    ATTN: Doc. Con. for 3141
    ATTN: Doc. Con. for Space Project Div.
    ATTN: Doc. Con. for D. Thornbrough
    ATTN: Doc. Con. for W. Brown
    ATTN: Doc. Con. for D. Dahlgren

Science Applications, Inc.
    ATTN: L. Linson
    ATTN: D. Hamlin
    ATTN: D. Sachs
    ATTN: E. Straker
    ATTN: J. McDougall
    ATTN: C. Smith
    ATTN: D. Baxter

Science Applications, Inc.
Huntsville Division
    ATTN: D. Divis

Science Applications, Inc.
    ATTN: SZ

SRI International
    ATTN: G. Carpenter
    ATTN: D. Johnson
    ATTN: C. Rino
    ATTN: G. Smith
    ATTN: G. Price
    ATTN: R. Leadabrand
    ATTN: J. Peterson
    ATTN: W. Jaye
    ATTN: W. Chesnut
    ATTN: M. Baron
    ATTN: A. Burns
    ATTN: D. Neilson

Tri-Com, Inc.
    ATTN: D. Murray

TRW Defense & Space Sys. Group
    ATTN: S. Altschuler
    ATTN: R. Plebuch
    ATTN: D. Dee

Visidyne, Inc.
    ATTN: J. Carpenter
    ATTN: C. Humphrey